

TECHNISCHE UNIVERSITÄT MÜNCHEN

Fakultät für Informatik  
Computer Aided Medical Procedures & Augmented Reality / I16

# Polar Active Contours for Medical Applications

Maximilian Tobias Baust

Vollständiger Abdruck der von der Fakultät für Informatik der Technischen  
Universität München zur Erlangung des akademischen Grades eines  
Doktors der Naturwissenschaften (Dr. rer. nat.)  
genehmigten Dissertation.

Vorsitzender:

Univ.-Prof. Dr. H. M. Gerndt

Prüfer der Dissertation:

1. Univ.-Prof. Dr. N. Navab
2. Prof. A. J. Yezzi, Georgia Institute of Technology, Atlanta, USA

Die Dissertation wurde am 11.08.2011 bei der Technischen Universität  
München eingereicht und durch die Fakultät für Informatik am 17.04.2012  
angenommen.



## Abstract

The accurate and robust detection and tracking of objects in different kinds of imaging data is a fundamental task in computer vision. A possible way of achieving these goals is to use active contours, i.e. contours which aim at finding or tracking the boundary of an object by minimizing an energy defined on the given image data. Since their introduction in the late 1980s, a lot of improvements have been made in order to make this technique applicable also to non-photometric imaging data and more robust with respect to noise, varying lighting conditions, intensity inhomogeneities, background clutter, etc. It turns out that several of these improvements are closely related to the question of how variational problems can be regularized. A quite recent regularization strategy consists in solving the corresponding energy minimization problem in Sobolev spaces. The main contribution of this thesis consists in the application of this regularization technique to polar active contours, i.e. a sub-class of active contours which can only describe star-shaped objects. Inspired by recent work on regularization strategies based on Sobolev spaces, we define a Sobolev space for polar active contours and endow it with a metric that allows the user to weight translations, scale-changes, and smooth deformations of the curve differently. The resulting polar active contours enjoy several properties, e.g. an increased robustness to noise, which are particularly desirable for medical applications such as the segmentation of abdominal aortic aneurysms from computed tomography angiography data or the tracking of the left ventricular cavity acquired by magnetic resonance imaging. Another advantage of this regularization strategy is that the computational overhead is only of linear complexity. When generalizing these ideas to active surfaces, however, one has to solve a partial differential equation (PDE) in every iteration step. The second contribution of this thesis is therefore the development of efficient numerical techniques for solving this PDE, where we do not restrict ourselves to star-shaped objects anymore. Further, we compare the resulting numerical schemes to the ones arising from other regularization strategies.



## Zusammenfassung

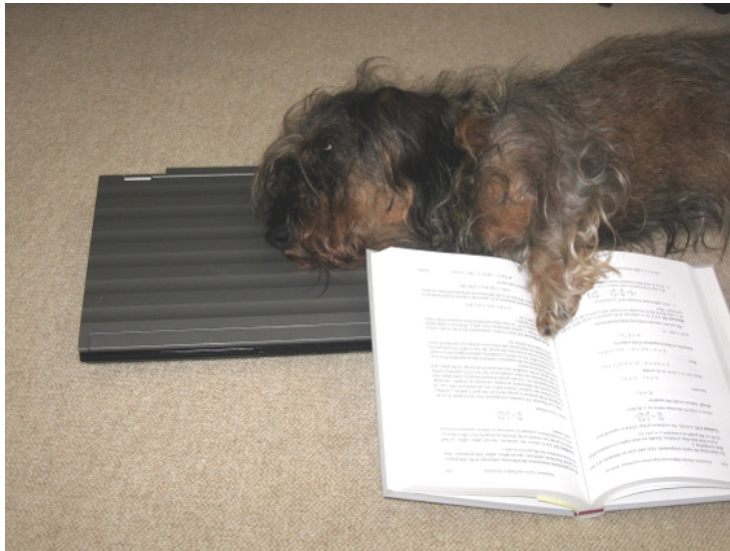
Die genaue und zuverlässige Objekterkennung und -Verfolgung in verschiedenen Bildgebungsmodalitäten ist eine wichtige Aufgabe im Bereich des maschinellen Sehens. Eine Möglichkeit um diese Ziele zu erreichen stellen so genannte aktive Konturen dar, welche den Rand eines Objektes finden und verfolgen indem sie eine Energie minimieren welche von den gegebenen Bilddaten abhängt. Seit ihrer Einführung in den späten 1980er Jahren wurden eine Reihe von Verbesserungen vorgeschlagen, welche die Anwendbarkeit auf nicht photometrische Bilddaten sowie die Robustheit in Bezug auf Bildrauschen, variierende Beleuchtungsbedingungen, Inhomogenitäten bzgl. der Bildintensitäten, inhomogene Hintergründe, usw. zum Ziel haben. Es stellt sich heraus, dass viele dieser Verbesserungen mit der Frage zu tun haben wie variationelle Probleme regularisiert werden können. Eine kürzlich vorgestellte Regularisierungsmethode besteht darin die entsprechenden Energieminimierungsprobleme in Sobolevräumen zu lösen. Der hauptsächliche Beitrag dieser Dissertation besteht in der Anwendung dieser Regularisierungsstrategie auf polare aktive Konturen, also aktive Konturen welche nur sternförmige Objekte beschreiben können. Inspiriert von kürzlich vorgestellten Arbeiten zur Regularisierung mit Sobolev Räumen definieren wir einen Sobolevraum für polare aktive Kurven und statten ihn mit einer Metrik aus, welche es dem Benutzer ermöglicht Translationen, Skalierungen sowie glatte Deformationen der Kurve unterschiedlich zu gewichten. Die resultierenden polaren aktiven Konturen weisen viele Eigenschaften, wie zum Beispiel eine größere Robustheit gegenüber Bildrauschen, auf, welche besonders für medizinische Anwendungen, wie zum Beispiel die Segmentierung von abdominalen Aortenaneurysmen in computertomographischen Angiographiedaten oder die Verfolgung der Wand der linken Herzkammer in Magneresonanztomographiedaten, von Vorteil ist. Ein weiterer Vorteil der vorgeschlagenen Regularisierungsmethode ist, dass der rechnerische Mehraufwand nur von linearer Komplexität ist. Will man diese Ideen jedoch auf aktive Oberflächen anwenden, muss eine partielle Differentialgleichung in jedem Iterationsschritt gelöst werden. Der zweite Beitrag dieser Arbeit ist deshalb die Entwicklung von effizienten numerischen Verfahren um diese Differentialgleichung zu lösen, wobei wir uns nicht mehr auf sternförmige Objekte beschränken. Des weiteren vergleichen wir die vorgeschlagenen Verfahren mit denen die aus der Anwendung anderer Regularisierungsverfahren resultieren.



## Acknowledgments

At this point I wish to express my gratitude for being blessed with the opportunity of carrying out research and writing this dissertation. For this reason, I would like to thank Professor Nassir Navab, because without his continuous support, his incredible serenity, and his great vision the research presented in this thesis would definitely not have been possible. Further, I would like to thank Professor Anthony Yezzi and Professor Gozde Unal for inviting me to Atlanta and Bologna and being a continuous source of inspiration. Moreover, I gratefully acknowledge the support of the international graduate school of science and engineering (IGSSE) at the Technische Universität München which provided me with a research scholarship, an excellent equipment, and a generous budget for education and travel. Last but not least, I would like to thank my family and especially my parents for consulting, encouraging, and supporting me in an absolutely unbelievable way.

During the last 40 months, my way was also accompanied by the following people who made this way a more pleasant and joyful one: Martina Hilla, Darko Zikic, Tobias Lasser, Martin Groher, Richard Brosig, José Gardiazabal, Andreas Keil, Ahmad Ahmadi, Stefan Hinterstoisser, Petra Kleiner, Olivier Pauly, Jakob Vogel, Selen Atasoy, Stefanie Demirci, Hauke Heibel, Nicola Brieu, and Loren Schwarz. In particular, I would like to mention Viktoria Kindzierski for believing in me and brightening up my life.



My Favorite Research Fellow.



# Contents

<b>Abstract</b>	<b>iii</b>
<b>Zusammenfassung</b>	<b>v</b>
<b>Acknowledgments</b>	<b>vii</b>
<b>Contents</b>	<b>ix</b>
<b>1 Introduction</b>	<b>1</b>
1.1 Objective . . . . .	1
1.2 The Importance of Being Smooth . . . . .	4
1.3 Peculiarities of Medical Image Segmentation . . . . .	15
1.4 Contributions and Outline . . . . .	21
<b>2 Active Contours</b>	<b>23</b>
2.1 Chronological Overview . . . . .	23
2.2 Taxonomies for Active Contours . . . . .	28
<b>3 Variational Level Set Methods</b>	<b>35</b>
3.1 The Non-geometric Case . . . . .	38
3.1.1 Generalizing Variational Level Set Methods . . . . .	38
3.1.2 Implicit Regularization Strategies . . . . .	40
3.1.3 Explicit Regularization . . . . .	46
3.1.4 Numerical Schemes for Tikhonov-type Regularizations . . . . .	47
3.2 The Almost Geometric Case . . . . .	55
3.2.1 The Classical $L^2$ Framework . . . . .	56
3.2.2 Sobolev Spaces on Implicit Surfaces . . . . .	57
3.2.3 Computing Sobolev Gradients . . . . .	58
3.2.4 Numerical Treatment . . . . .	59

---

<b>4</b>	<b>Polar Active Contours</b>	<b>63</b>
4.1	Introduction . . . . .	63
4.2	Polar Spaces . . . . .	65
4.2.1	Variational Active Contours . . . . .	65
4.2.2	The Polar Space $\mathcal{L}$ . . . . .	66
4.2.3	The Polar Space $\mathcal{H}$ . . . . .	67
4.3	Implementation . . . . .	70
4.3.1	Computation of $\nabla_{\mathbb{R}^2} E$ . . . . .	70
4.3.2	Choosing $\lambda$ and $\gamma$ . . . . .	70
4.3.3	Choosing the Origin . . . . .	71
4.3.4	Solving the ODE . . . . .	72
4.3.5	Deriving a First Order Correction for $\phi$ . . . . .	73
4.4	Experiments . . . . .	75
4.4.1	Comparing Different Flows . . . . .	75
4.4.2	Coarse-to-Fine Behavior . . . . .	77
4.4.3	Comparison to Classical Sobolev Active Contours . . . . .	77
4.4.4	Visual Tracking Applications . . . . .	78
4.4.5	Quantitative Evaluation . . . . .	81
<b>5</b>	<b>Conclusion</b>	<b>85</b>
	<b>Appendix</b>	<b>86</b>
<b>A</b>	<b>Sobolev Spaces</b>	<b>87</b>
<b>B</b>	<b>Other Contributions</b>	<b>91</b>
B.1	Stent Graft Removal for Improving 2D-3D Registration . . . . .	91
B.2	Monocular Deformable Model-to-Image Registration of Vascular Structures . . . . .	92
B.3	Generalization of Deformable Registration in Riemannian Sobolev Spaces . . . . .	93
B.4	A General Preconditioning Scheme for Difference Measures in Deformable Registration . . . . .	94
B.5	Midbrain Segmentation in Transcranial 3D Ultrasound for Parkinson Diagnosis . . . . .	95
B.6	3D Stent Recovery from One X-ray Projection . . . . .	96

# 1

## Introduction

### 1.1 Objective

The detection and tracking of objects in various kinds of image data are fundamental tasks in computer vision. It is quite common to formulate these tasks as optimization or variational problems and a particular class of such approaches are *active contours*, which have been introduced by Kass, Witkin, and Terzopoulos in [54]. The concept of active contours involves the following three ideas:

1. An object is described by a contour delineating its boundary.
2. The desired configuration of the contour is modeled as a local minimum of an energy defined on the image data.
3. Starting from an (user-defined) initial configuration the contour minimizes the energy and thus evolves towards the boundary of the object of interest, cf. Fig. 1.1.

It is important to notice that active contours are designed to provide solutions to *low-level* vision tasks, i.e. the detection of lines, edges, and subjective contours. Thus, they need to be combined with high-level mechanisms which "can interact with the contour model by pushing it toward an appropriate local minimum" [54]. In the absence of such a high-level mechanism the user himself has to interact with the contour by defining its initial configuration and possibly some additional constraints. Unfortunately, active contours are often too local, in the sense that they are too much depending on the initialization or require too many constraints. A typical example for this behavior can be seen in Fig. 1.1a, where the knife is almost able to prevent the contour from segmenting the lime. As a consequence, a lot of research has been carried out in order to make active contours *more global*. Possible approaches are:

1. Integrating more descriptive cues such as gray value information, color, texture, or motion, e.g. [20, 28, 33, 82, 119].

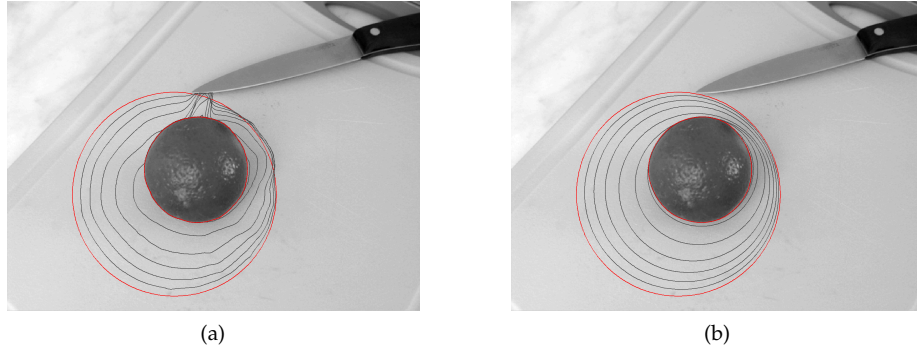


Figure 1.1: **Regularizing Active Contours:** Starting from an initial configuration, drawn in red, two active contours evolve towards the boundary of a lime. Several intermediate configurations are drawn in gray while the final configuration is drawn in red again. Note that the classical (polar) active contour gets almost distracted by the knife (a), which is not the case for the proposed method (b).

2. Integrating prior shape and appearance information, e.g. [27, 26, 25, 61, 118].
3. Making the variational formulation convex in order to find a global solution, e.g. [76, 13, 29].
4. Developing high level mechanisms which provide a good initialization, e.g. [43].
5. Regularize the curve *evolution* by splitting off rigid components and making it smoother, e.g. [110, 108, 109, 107, 21].

The contributions of this dissertation are related to the latter approach. Inspired by [110, 21] and especially [107] we develop a regularization strategy for *polar active contours*, i.e. active contours which are based on a polar object representation. Polar active contours are particularly useful for several medical applications such as the segmentation of the left ventricular cavity from sequential ultrasound (US) data or magnetic resonance imaging (MRI) [104, 39, 37, 38, 31, 65], the slice-wise segmentation of aortic aneurysms from US or computed tomography angiography (CTA) data [92, 12, 4], the segmentation of kidneys in sequential US data [36], and the segmentation and tracking of individual cells [93, 50]. As demonstrated in Fig. 1.1b, the proposed approach is far less sensitive to undesired local minima and it allows the user to adjust how much translations and scale changes of the curve are favored over smooth deformations.

We shall see in Sec. 1.2 that the choice of a particular regularization strategy has also an impact on the choice of the numerical methods. Thus, a second contribution of this thesis is the comparison and development of numerical techniques for the regularization strategies proposed by [21] and [110], but we do not restrict ourselves to polar descriptions anymore.

Achieving smoothness is, however, not only a main component of the proposed regularization strategy. In fact, it is a much more general regularization concept and for this reason we devote Sec. 1.2 to the explanation why achieving smoothness is so important. As the applications for the methods proposed in this dissertation are mainly medical, we will also discuss some peculiarities of medical image segmentation in Sec. 1.3. In Sec. 1.4 we finally explain the contributions of this thesis in detail, before we proceed with the discussion of the related work in chapter 2.

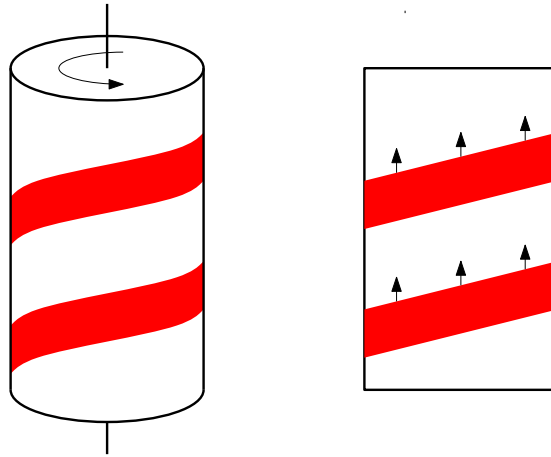


Figure 1.2: **The Barber Pole Illusion:** The diagonal stripes of a horizontally rotating pole appear to move upwards when looking at the pole from the front. Thus, the perceived motion differs from the actual motion of the stripes.

## 1.2 The Importance of Being Smooth

The continuous improvement of computer vision systems is not only of practical value, e.g. for the development of image understanding systems, but it also helps us to understand how the human visual system might work. A good example is the so-called *barber pole illusion*, cf. Fig. 1.2, which occurs when a diagonally striped pole is rotating around its vertical axis. For most people the stripes appear to be moving vertically rather than horizontally. Interestingly, standard algorithms for the computation of optical flow are trapped in a similar way, cf. [89]. The reason for this illusion is that there are multiple motions explaining the same visual perception making the determination of the optical flow an *ill-posed* problem. While humans can use their experience in order to decide for a particular solution, algorithms require *a priori information*. Perhaps the most common a priori assumption is *piecewise continuity* or *smoothness* and we shall now see why.

Avoiding a discussion on how or if the development of computer vision systems and the research on human vision should influence each other, we hope that most people will agree that building a computer vision system could be subdivided in the following way. At first, one usually makes simplifying assumptions about the world leading to *stable descriptions* [11], where stable means that these descriptions should be invariant to lighting conditions, optical distortions, etc. Often, these stable descriptions are modeled as the solution to a *minimization problem* which is finally discretized in order to compute a *numerical solution* as depicted in Fig. 1.3. We shall see now that continuity and smoothness play a crucial role in all these steps<sup>1</sup>.

---

<sup>1</sup>At this point we do not want to make a precise mathematical distinction between continuity and smoothness.

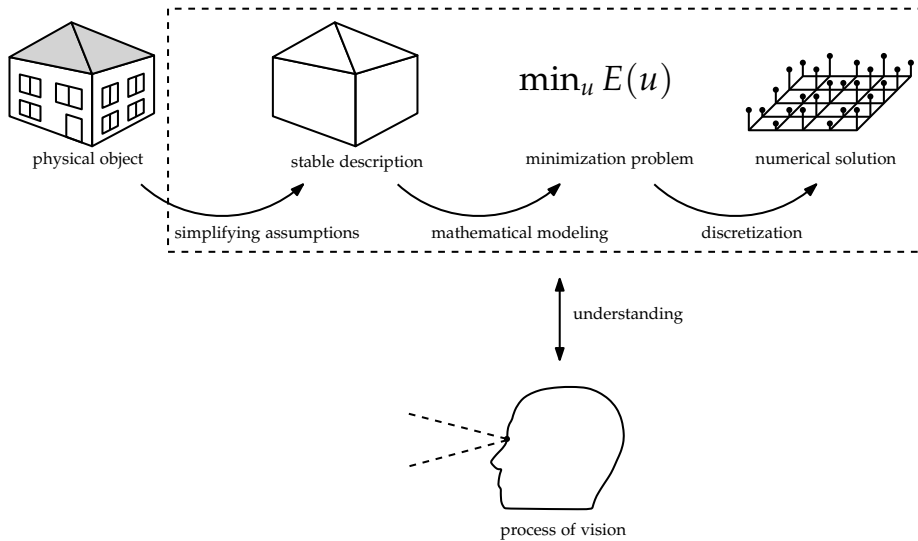


Figure 1.3: **Modeling Vision:** Building a computer vision system involves the creation of stable descriptions, the mathematical modeling of them, and finally their numerical computation. The whole process can help to understand the human visual system as well as the understanding of human vision can influence the development of computer vision systems.

### Simplifying Assumptions and Stable Descriptions

An important part of computer vision consists in implementing so-called *early vision processes*, i.e. processes which recover physical properties of the surrounding visible surfaces from two-dimensional intensity data [89]. Typical early vision processes are edge detection, spatio-temporal interpolation and approximation, optical flow computation, etc. The output of such processes, as well as the raw intensity data itself, can be considered as *visual data* and can be used for what Blake and Zisserman [11] call *visual reconstruction*, i.e. the process of reducing visual data to *stable* and *unambiguous* descriptions, where stable means that these descriptions should be invariant to lighting conditions, optical blurring and distortion, sampling grain, sensor noise, etc. These two demands are a consequence of the fact that early vision can be regarded as *inverse optics* [89]. In contrast to classical optics or computer graphics, which are concerned with the generation of images from three dimensional objects [89], early vision suffers from a loss of information during the imaging process. This loss of information is due to the technical limitations of the image formation process described above, but also due to the loss of three dimensional information as a consequence of the projection. In order to compensate for this loss of information one often incorporates prior assumptions on the surrounding world and the perhaps most popular prior is the *continuity* of surfaces or along curves [11]. The reason why continuity constraints actually make sense is that they yield *physically plausible* solutions due to the coherence of matter, which gives rise to smoothly varying intrinsic scene characteristics [113]; such

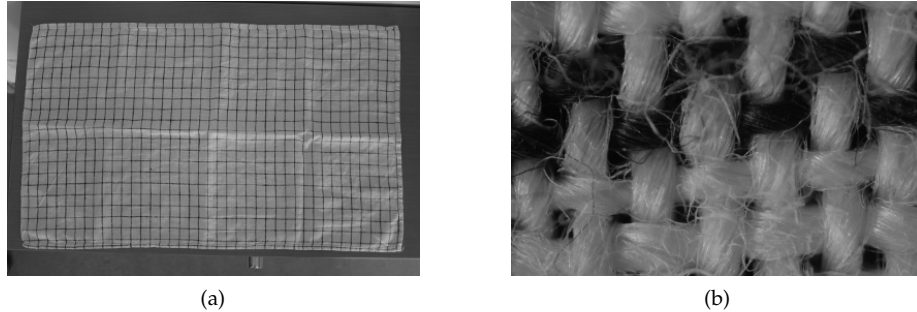


Figure 1.4: **Scale Dependency of Continuity Assumptions:** The cloth appears to be continuous at a coarse scale, but at a finer scale its fabrics become visible and appear as continuous objects themselves (image courtesy of José Gardiazabal).

assumptions are, of course, depending on the scale, cf. Fig. 1.4.

As noted in [113, 11], global continuity constraints are, however, not always appropriate, because they fail to model sudden changes in a scene, e.g. in the case of occlusions. For this reason Terzopolous proposed to use so-called *controlled-continuity constraints* [113] which allow for *piecewise continuous* solutions. It should be noted, however, that in contrast to the pure mathematical definition of piecewise continuity the enforcement of this property is usually accompanied by the expectation that “the fewer pieces the better” [11].

### Mathematical Modeling and Variational Problems

As explained in the last paragraph, early vision processes can be regarded as inverse optics or, put more mathematically, as *inverse problems*, which are typically *ill-posed*. Ill-posedness according to Hadamard [45] means that for a given mathematical problem at least one of the following conditions is violated:

1. A solution exists.
2. The solution is unique.
3. The solution depends continuously on the data.

Obviously, the requirement for unambiguous solutions directly translates to the second condition, but also the third condition might be violated in early vision as in the case of edge detection [89]. In order to render ill-posed early vision problems well-posed one can incorporate a priori knowledge. This a priori information enters the arena either in a deterministic or in a probabilistic way [89], which in most cases leads to either variational or graphical models, e.g. Markov Random Fields. A connection between these two approaches is given by a simplified version of Boltzmann’s law [11]. If we formulate an early vision problem, e.g. the computation of optical flow, in a variational manner, we typically want to minimize an energy  $E$ . If we further denote the solution

to this problem, i.e. the flow field, by  $u$  and the probability for the occurrence of  $u$  by  $\Pi(u)$ , we have that

$$\Pi(u) \propto e^{-E(u)}. \quad (1.1)$$

Besides this relationship one needs, of course, a way to translate the continuous energy into discrete clique potentials for instance. This is usually done by considering finite element discretizations of the variational formulation [112, 100]. In this dissertation, however, we will focus on variational models and refer the interested reader to recent literature on graphical models such as [10, 77].

An early vision task rendered in a variational manner usually results in a minimization problem of the form

$$\min_{u \in F} E(u, I), \quad (1.2)$$

where  $E$  is an energy (cost function, potential, data term, etc.), which measures how well the solution  $u$  explains a certain aspect of the acquired image data  $I$ , and  $F$  is some function space. In order to simplify the notation, we will omit the dependency on  $I$  in the following. Now, there are mainly two possibilities of regularizing this problem:

1. **Explicit Regularization.** The idea of explicit regularization is to consider an additional energy  $R$ , called *regularizer*, which becomes minimal, if the computed solution perfectly resembles the a priori assumption modeled by  $R$ . Such a regularizer can now be incorporated in two different ways [89]. The first possibility is to treat the original energy as a constraint and solve the following minimization problem:

$$\min_{u \in F} R(u), \quad \text{subject to } E(u) \leq \epsilon, \quad (1.3)$$

where  $\epsilon > 0$  is a user-defined tolerance often depending on the estimated or expected amount of noise. For this type of regularization one requires  $E$  to be non-negative, which is, however, not a tremendous restriction. The second possibility, which is often used in the area of image segmentation and optical flow estimation, is to minimize a linear combination of the original energy and the regularizer:

$$\min_{u \in F} E(u) + \lambda R(u), \quad (1.4)$$

where the *regularization parameter*  $\lambda > 0$  allows the user to control the compromise between regularization and closeness to the data [89].

2. **Implicit Regularization.** In contrast to explicit regularization, the incorporation of a priori information is achieved by seeking the solution to the original problem in a subset or subspace  $S \subset F$  yielding the minimization problem

$$\min_{u \in S \subset F} E(u). \quad (1.5)$$

The delusive beauty of implicit regularization lies in the fact that there is no parameter, such as  $\epsilon$  or  $\lambda$  as in the case of explicit regularization, but the choice of a suitable subset or subspace can be very difficult, too.

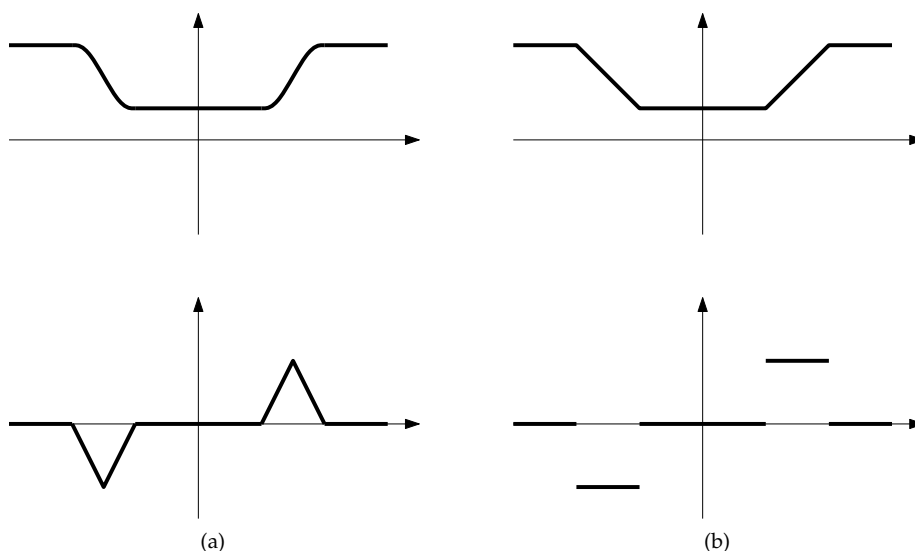


Figure 1.5: **Continuous Functions:** Two continuous functions (upper row) with (a) and without (b) continuous derivative (lower row).

Of course, one can combine an explicit with an implicit regularization in order to weave in different kinds of a priori information, e.g.  $S$  could be chosen as a space spanned by some statistically trained basis functions and  $R$  could enforce the sparsity of the solution with respect to this basis. However, a discussion of all kinds of prior information and how they are connected to the choice of  $S$  and  $R$  is far beyond the scope of this introduction. As also the methods presented in this dissertation are closely related to the generic assumption of smoothness, we will focus on smoothness priors in the following.

In order to design regularizers and function spaces which allow to control the smoothness of the solution we need a precise mathematical definition of smoothness and a way to measure it. The key observation to be made is that the smoothness of a function can be assessed by considering its derivatives as well as the continuity of them. If we consider the two functions in Fig. 1.5, we can observe that the function with a continuous derivative has no kinks in contrast to the function without<sup>2</sup>. This consideration can be iterated and leads to the well known concept of  $C^k$  functions, where  $k \in \mathbb{N}$  indicates that the function is  $k$ -times differentiable and all derivatives are continuous. Obviously, the higher the  $k$  the smoother the function, but how do we compare two functions of the *same* class? The fact that such a comparison is necessary becomes visible in Fig. 1.6. Following our intuition we would consider the function in Fig. 1.6a as smoother than the function in Fig. 1.6b, although both functions are members of the same  $C^k$  class, i.e. spline curves of the same degree. A good idea for

<sup>2</sup>The function depicted in Fig. 1.5b is only differentiable in the distributional sense, but this is not of importance here.

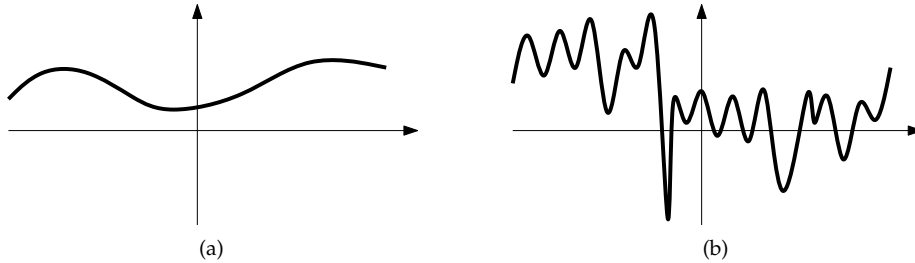


Figure 1.6: **Smooth Functions:** Although both functions are members of the same  $C^k$  class everyone would intuitively consider the function in (a) to be smoother.

distinguishing these two functions is to consider the expression

$$\int_{\Omega} |u'(x)| \, dx, \quad (1.6)$$

where  $\Omega$  is the domain on which  $u$  is defined. Functionals of this type can now be used as (explicit) regularizers and popular choices are for instance the

- *total variation*

$$R(u) = \int_{\Omega} |\nabla u(x)| \, dx \quad (1.7)$$

which has been introduced in computer vision for denoising purposes [97], or the

- *first order Tikhonov regularizer* [115]

$$R(u) = \frac{1}{2} \int_{\Omega} |\nabla u(x)|^2 \, dx. \quad (1.8)$$

At first sight, these definitions only make sense for differentiable functions, but they can be well generalized to weaker types of differentiability. For the mathematical details of these generalizations we refer the interested reader to [35, 101] and focus on providing the geometrical and mechanical, respectively, interpretation of these regularizers.

Let  $A$  be a closed subset of  $\mathbb{R}^2$  and  $u : \mathbb{R}^2 \rightarrow \{0, 1\}$  be the *characteristic function* of  $A$ :

$$u(x) = \begin{cases} 1, & x \in A, \\ 0, & x \notin A. \end{cases} \quad (1.9)$$

Then the total variation of  $u$  is exactly the length of the boundary  $\partial A$  of  $A$  [13]. If  $u$  is for instance the output of a binary segmentation problem, the usage of the total variation as an explicit regularizer would serve as a penalty on the length of the boundary of the segmentation result.

In contrast to this geometric interpretation of the total variation, the first order Tikhonov regularizer has a mechanical one. If we consider a thin soap film attached to a wire frame and neglect the gravity acting on it, the position



Figure 1.7: **Soap Film:** The position of the soap film is well approximated by the solution of the Poisson equation, the Dirichlet-type boundary condition corresponds to the position of the wire frame.

of the film at each point above the ground can then be well approximated by the solution to the variational problem

$$\begin{cases} \min_u \frac{1}{2} \int_{\Omega} |\nabla u(x)|^2 dx, & x \in \Omega, \\ u(x) = g(x), & x \in \partial\Omega, \end{cases} \quad (1.10)$$

where  $g : \partial\Omega \rightarrow \mathbb{R}$  models the position of the wire frame and  $\Omega \subset \mathbb{R}^2$  is the open subset below the wire frame, cf. Fig. 1.7. In other words, the equilibrium configuration of the sheet approximately minimizes the elastic energy given by the Tikhonov regularizer [11].

The minimization problem in (1.10) obviously lacks the specification of the function space in which the solution is supposed to be sought. In the case of the above discussed minimization problem a minimum requirement on the function space should be that the energy to be minimized is well-defined, i.e.

$$\int_{\Omega} |\nabla u(x)|^2 dx < \infty \quad (1.11)$$

should hold for all members of this function space. Thus, a proper function space might be given by the so-called *Sobolev space*

$$H^1(\Omega) = \left\{ u \in L^2(\Omega) : \int_{\Omega} |\nabla u(x)|^2 dx < \infty \right\}. \quad (1.12)$$

For a more mathematical introduction to Sobolev spaces we refer the interested reader to appendix A or to the excellent book of Evans [35]. The reason why this Sobolev space is based on  $L^2$  is simply due to the fact that  $L^2$  is a Hilbert space and  $H^1$  becomes a sub-Hilbert space of  $L^2$  by endowing it with the inner product

$$\langle u, v \rangle_{H^1} = \int_{\Omega} u(x)v(x) dx + \int_{\Omega} \nabla u(x) \cdot \nabla v(x) dx \quad (1.13)$$

$$= \langle u, v \rangle_{L^2} + \langle \nabla u, \nabla v \rangle_{L^2}, \quad (1.14)$$

which is based on the  $L^2$  inner product. A Hilbert space framework is very desirable, because it provides us with several important tools such as the Riesz representation theorem [35], which we shall use later in order to compute the gradient of an energy with respect to the employed inner product.

An interesting observation is that the usage of a particular explicit regularization often even *enforces* that the solution is an element of a certain function space. If we assume that

$$\|u\|_{L^2}^2 \leq CE(u) \quad (1.15)$$

holds for some constant  $C > 0$  and any  $u \in L^2(\Omega)$ , we may conclude that for any solution  $u^*$  of the Tikhonov regularized problem the following inequality holds:

$$\|u^*\|_{L^2}^2 + \int_{\Omega} |\nabla u^*(x)|^2 dx \leq \max \left\{ C, \frac{2}{\lambda} \right\} \left( E(u^*) + \frac{\lambda}{2} \int_{\Omega} |\nabla u^*(x)|^2 dx \right). \quad (1.16)$$

As a solution has, of course, a finite (regularized) energy, we may conclude that  $u^* \in H^1(\Omega)$ . A similar consideration yields that any solution, with finite regularized energy again, to a problem regularized by the total variation is an element of the space of functions of bounded variation, i.e.  $BV(\Omega)$ .

Now, one may wonder, if there are any differences between an explicit regularization using the Tikhonov regularizer and an implicit one with  $S = H^1(\Omega) \subset L^2(\Omega) = F$ . In fact, there are and in order to get a first impression we consider the numerical methods for computing a solution, because each regularization strategy has its own peculiarities on the computational level.

### Discretization and Numerical Solutions

At first, we consider the explicit Tikhonov regularized problem

$$\min_{u \in L^2(\Omega)} E(u) + \lambda R(u), \quad (1.17)$$

where  $R$  is the Tikhonov regularizer defined in (1.8). In order to compute a necessary condition for a minimizer of (1.17) we compute the *first variation*  $F(E + \lambda R, v)$  of the regularized energy. We choose  $v \in L^2(\Omega)$  arbitrarily and evaluate the regularized energy on the line  $u + sv$ , cf. Fig. 1.8. If we assume that  $u$  is already a local minimizer, the following condition must hold:

$$F(E + \lambda R, v) = \frac{d}{ds} \left[ E(u + sv) + \frac{\lambda}{2} \int_{\Omega} |\nabla(u + sv)|^2 dx \right] \Big|_{s=0} = 0. \quad (1.18)$$

Thus, the first variation can be considered as a generalized *directional derivative*. After some manipulations we usually end up with an expression of the form

$$F(E + \lambda R, v) = \int_{\Omega} (\nabla E(u) - \lambda \Delta u) v dx = \langle \nabla E(u) - \lambda \Delta u, v \rangle_{L^2} = 0, \quad (1.19)$$

where  $\nabla E(u)$  is the gradient of the energy  $E$  and  $-\lambda \Delta u$  is the gradient of the Tikhonov regularizer. As  $v$  was chosen arbitrarily the fundamental lemma of variational calculus [35] tells us that

$$\nabla E(u) - \lambda \Delta u = 0, \quad (1.20)$$

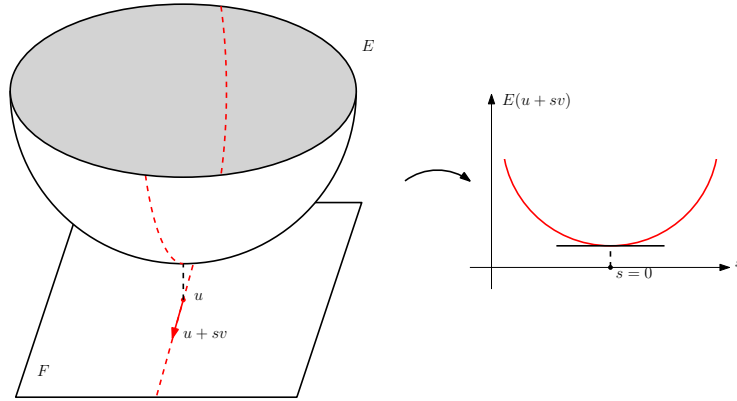


Figure 1.8: **Computing the First Variation:** Evaluating the regularized energy on the line  $u + sv$  leads to a one dimensional function, which has a local minimum, and thus a vanishing derivative, at  $s = 0$ .

which is called the *Euler-Lagrange equation* of the regularized problem.

By setting  $v = -\nabla E(u) + \lambda \Delta u$  in (1.19) we verify that the negative gradient is the direction in which the (regularized) energy decreases the most:

$$F(E + \lambda R, -\nabla E(u) + \lambda \Delta u) = -\|\nabla E(u) - \lambda \Delta u\|_2^2 < 0. \quad (1.21)$$

Thus, we can use the continuous gradient descent

$$\partial_t u = -\nabla E(u) + \lambda \Delta u \quad (1.22)$$

in order to minimize (1.17). Starting with an initial guess  $u^0$  one possibility for solving this evolution equation is to iteratively update the current solution  $u^t$  according to

$$u^{t+\tau} = u^t - \tau (\nabla E(u^t) - \lambda \Delta u^t), \quad (1.23)$$

which corresponds to a forward Euler time discretization. Unfortunately, the usage of the Tikhonov regularizer introduces a severe restriction on the choice of the step size  $\tau$  in order to guarantee numerical stability. This restriction is known as *Courant-Friedrichs-Lewy (CFL) condition* and reads for the above described scenario

$$\tau \leq \frac{1}{2^d \lambda}, \quad (1.24)$$

where  $d$  is the dimension of the domain  $\Omega$  on which  $u$  is defined [123]. As a consequence, the more regularity we enforce by increasing  $\lambda$ , the smaller we have to choose the step size in order to compute the solution. In order to overcome this issue one can use a semi-implicit time discretization:

$$u^{t+\tau} = u^t - \tau (\nabla E(u^t) - \lambda \Delta u^{t+\tau}) \quad (1.25)$$

leading to the update equation

$$u^{t+\tau} = (I - \tau \lambda \Delta)^{-1} (u^t - \tau \nabla E(u^t)), \quad (1.26)$$

which allows for larger time steps.

Next, we consider the implicit  $H^1$  regularized problem

$$\min_{u \in H^1(\Omega)} E(u). \quad (1.27)$$

Similar to the Tikhonov regularized problem we can compute the first variation in order to obtain the gradient of the energy. As indicated in (1.19), the computation of the first variation, and thus the computation of the gradient of the energy, depends on the employed Hilbert space or, more precisely, on the employed inner product. For this reason the first variation reads

$$F(E, v) = \langle \nabla_{H^1} E(u), v \rangle_{H^1} = 0 \quad (1.28)$$

leading to the continuous gradient descent

$$\partial_t u = -\nabla_{H^1} E(u). \quad (1.29)$$

As a consequence, it is incorrect to refer to  $\nabla E(u)$  in (1.19) as *the gradient*. Thus, we call  $\nabla E(u)$  the  $L^2$  gradient of  $E$  and write  $\nabla_{L^2} E(u)$  in the following.

The obvious question is now how to obtain the Sobolev gradient  $\nabla_{H^1} E(u)$ ? Fortunately, we are in a Hilbert space framework which allows us to use the Riesz representation theorem, cf. appendix A or [35], which tells us that

$$F(E, v) = \langle \nabla_{H^1} E(u), v \rangle_{H^1} = \langle \nabla_{L^2} E(u), v \rangle_{L^2}, \quad (1.30)$$

because any linear functional such as the first variation has a unique representation with respect to the used inner product. Using the definition of the  $H^1$  inner product and applying integration by parts we obtain

$$\langle (I - \Delta) \nabla_{H^1} E(u) - \nabla_{L^2} E(u), v \rangle_{L^2} = 0 \quad (1.31)$$

and since  $v$  was chosen arbitrarily we end up with

$$(I - \Delta) \nabla_{H^1} E(u) - \nabla_{L^2} E(u) = 0 \quad \Rightarrow \quad \nabla_{H^1} E(u) = (I - \Delta)^{-1} \nabla_{L^2} E(u), \quad (1.32)$$

where  $(I - \Delta)^{-1}$  can be interpreted as a smoothing operator or projector mapping  $\nabla_{L^2} E(u)$  into the Sobolev space  $H^1$ . Applying a forward Euler time discretization in (1.29) we end up with the update equation

$$u^{t+\tau} = u^t - \tau (I - \Delta)^{-1} \nabla_{L^2} E(u^t). \quad (1.33)$$

Setting  $\tau = \lambda = 1$  in (1.26) we can now compare the explicit Tikhonov regularization with the implicit  $H^1$  regularization as follows:

- Applying  $(I - \Delta)^{-1}$  to the update  $\nabla_{L^2} E(u^t)$  corresponds to the  $H^1$  regularization.
- Applying  $(I - \Delta)^{-1}$  to the whole right hand side  $u^t - \nabla_{L^2} E(u^t)$  corresponds to the Tikhonov regularization.

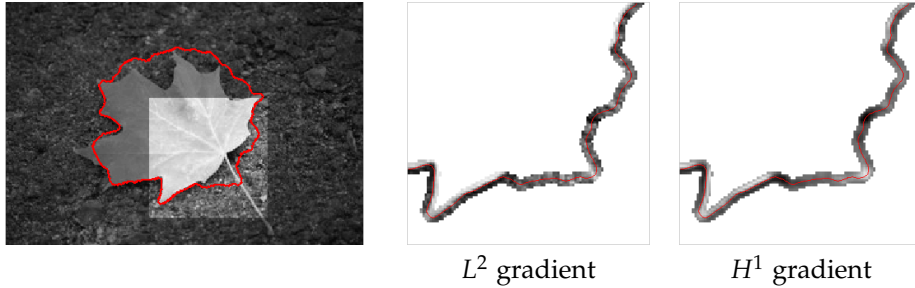


Figure 1.9: **Different Gradients:** We compare the  $L^2$  gradient and the  $H^1$  gradient, which are visualized in the narrow band of a function which represents the evolving curve (red) by its zero level set. Note that the Sobolev gradient is much more regular than the  $L^2$  gradient. (The image data taken from [2].)

In other words, the  $H^1$  regularization ensures that only the computed *update* is smooth while the Tikhonov regularization ensures that the *solution* is smooth. This assertion can be generalized to many other explicit and, if  $S$  is a vector space, also to many other implicit regularization strategies, cf. Sec. 3.1.4.

Before we proceed with the peculiarities of medical image segmentation in Sec. 1.3 we wish to point at another important property of  $H^1$  regularization. Consider (1.33) in the frequency domain:

$$\hat{u}^{t+\tau}(l) = \hat{u}^t(l) - \frac{\tau}{1 + (2\pi l)^2} \widehat{\nabla_{L^2} E(u^t)}(l), \quad l \in \mathbb{Z}, \quad (1.34)$$

where  $\hat{\cdot}(l)$  denotes the  $l$ -th Fourier coefficient of the corresponding quantity, cf. [108]. Obviously, the higher the frequency is the larger is the penalty on it. A consequence of this weighting is the so-called *coarse-to-fine* behavior being typical for Sobolev-type implicit regularization strategies. If  $u$  is for instance a function whose zero level set encodes the boundary of an object, low frequency components of  $u$  correspond to the coarse shape of the object while high frequency components are needed to approximate finer structures. As the step size for coarser shapes is greater than for finer ones, cf. (1.34), we observe that the iteratively computed segmentation first converges towards something one would consider as a *rough guess* of the shape before adapting to the finer details of it. This way, the very local behavior of the image is far less inherited by the gradient of the energy leading to an increased robustness to undesired local minima, cf. Fig. 1.9. In addition to this coarse-to-fine behavior an implicit  $H^1$  regularization has even more beneficial numerical properties such as a stable gradient ascent for the backward heat equation [110] or a preconditioning effect [94].

Summing up, we have seen that there are mainly two possibilities of translating the abstract a priori assumption of smoothness into mathematical models, i.e. explicit and implicit regularization, and we got a first impression on how the choice of such a regularization strategy influences the numerical techniques to be used for computing a solution.

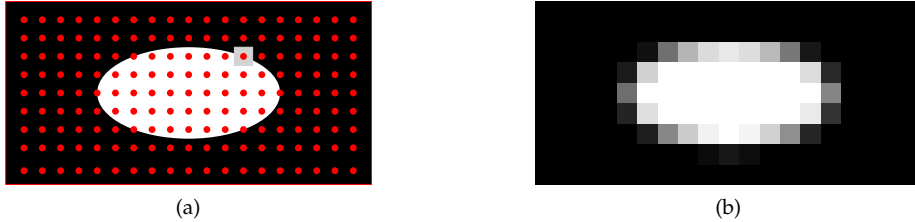


Figure 1.10: **Partial Volume Effect:** Due to the coarse sampling (indicated by the red dots in (a)) the resulting image shows several partial volume effects at the boundary of the white object. The reason is that both tissue types (black and white) contribute to the intensity value of the generated image (b) due to the relatively large influence area of each pixel (gray square in (a)).

### 1.3 Peculiarities of Medical Image Segmentation

A crucial step in the design of any computer vision algorithm consists in understanding the image formation process as well as the limitations of the employed imaging modalities, because these considerations give often a very good hint which energies and which type(s) of regularization should be chosen. We will discuss several modality specific limitations which are common in medical imaging in the following, where we focus on anatomical rather than functional imaging modalities. Moreover, we will explain how the regularization strategies presented in Sec. 1.2 can help to deal with these limitations, if appropriate. In addition to the modality specific limitations that have to be taken into account we will also comment on other aspects which should be considered when designing a segmentation system for medical purposes, such as *interaction*, *reproducibility*, *runtime*, and *evaluation*.

**Noise** The term *noise* can be traced back to Walter Schottky who made current fluctuations in electrical circuits audible in 1918 [103]. More generally, any random and unwanted signal variation is considered as noise, but it is, of course, far beyond the scope of this introduction to discuss all possible physical sources of noise. At this point, we shall only note that, first of all, noise is *unavoidable*, since any electronic system is at least affected by John-Nyquist noise due to the thermal agitation of electric charge in conductors [53, 78]. Secondly, the noise model to be used depends significantly on the imaging modality: While additive Gaussian or Poisson noise models can be used for photometric imaging, a multiplicative Rayleigh noise model is for instance used for US imaging, cf. [58].

From a numerical point of view, noise may cause an active contour evolution to get stuck in an undesired local minimum. The reason is that an active contour gradient without regularization usually inherits the very local behavior of the image to be segmented. It can be seen in Fig. 1.9 that an implicit  $H^1$  regularization causes the gradient to be more regular and less dependent on the local behavior of the image. Also explicit regularizations help to avoid

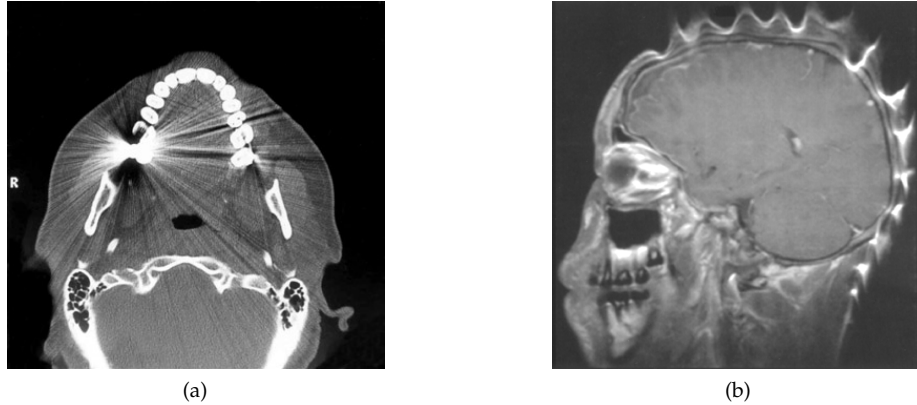


Figure 1.11: **Image Artifacts:** CT image taken from [1] showing streak artifacts caused by metal implants (a) and T1-weighted MRI image taken from [69] showing susceptibility artifacts caused by iron oxide particles suspended in the beeswax dressing in the hair of the patient (b).

getting stuck in an undesired local minimum. Instead of curing symptoms, i.e. regularizing the gradient, it is, of course, also possible to fight the root of all evil and regularize or smooth the image itself. It is thus no surprise that the Tikhonov regularizer and the total variation are also used for variational image restoration and denoising, e.g. [74, 97].

**Partial Volume Effects** occur when several tissue types contribute to the intensity value(s) of a single voxel which results in blurred tissue boundaries [88], which is illustrated in Fig. 1.10. Partial volume effects become less severe by increasing the spatial resolution, but even today the inter-slice resolution of many CT and MRI systems is still significantly worse than the achieved in-slice resolution.

**Intensity Inhomogeneities** typically occur in MR imaging, where they are caused by inhomogeneities and distortions of the magnetic field [88, 124]. As a consequence, voxels of one tissue class may have significantly different intensity values across the entire image or volume. This hampers the usage of segmentation methods which assume a constant intensity value per region such as the well known piecewise constant Mumford-Shah model [74]. A good strategy of dealing with these artifacts turns out to be the computation of a so-called *bias field* along with the segmentation in order to correct the intensity values and eventually enable the usage of piece wise constant models again [62]. Interestingly, such methods perform also well on other imaging modalities such as radiography or US, cf. [62].

**Anisotropic Resolution** When dealing with two dimensional photometric image data one often neglects the true image resolution and assumes a unit

### 1.3 PECULIARITIES OF MEDICAL IMAGE SEGMENTATION

$B_0(T)$	WM	cGM	Caudate	Thalamus	Putamen	Globus pallidus
0.20	361( $\pm 17$ )	635( $\pm 54$ )	555( $\pm 19$ )	522( $\pm 44$ )	524( $\pm 19$ )	411( $\pm 20$ )
1.0	555( $\pm 20$ )	1036( $\pm 19$ )	898( $\pm 45$ )	807( $\pm 47$ )	815( $\pm 16$ )	625( $\pm 14$ )
1.5	656( $\pm 16$ )	1188( $\pm 69$ )	1083( $\pm 52$ )	972( $\pm 32$ )	981( $\pm 13$ )	746( $\pm 20$ )
4.0	1010( $\pm 19$ )	1723( $\pm 93$ )	1509( $\pm 53$ )	1452( $\pm 87$ )	1446( $\pm 32$ )	1143( $\pm 27$ )
7.0	1220( $\pm 36$ )	2132( $\pm 103$ )	1745( $\pm 64$ )	1656( $\pm 84$ )	1700( $\pm 66$ )	1347( $\pm 52$ )

Table 1.1: **T<sub>1</sub> Relaxation Times:** T<sub>1</sub> relaxation times of different brain tissues for varying magnetic field strengths ( $B_0(T)$ ), cf. [95].

pixel spacing. In contrast to this, more care has to be taken when medical image data has to be processed, because CT and MRI scans often exhibit a much coarser resolution in one direction. A good example is for instance a (dynamic) MRI acquisition of short axis slices of the left ventricle which may have an intra-slice resolution of 1.3mm and an inter-slice resolution of 8mm [91]. Such differences in the spatial resolution have, of course, to be considered when PDEs need to be discretized by finite differences which is quite common in many segmentation and registration algorithms. It should be noted that the problem of anisotropic resolution is far less pronounced in image data acquired with modern scanners, such as state-of-the-art multi slice CT devices. However, there are still application areas where more attention has to be paid, e.g. in the case of compounded US sweeps [14].

**Imaging Artifacts** can have many reasons and depend, of course, on the used imaging modality. As in the case of noise it would be far beyond the scope of this introduction to discuss all possible types of imaging artifacts, but the images in Fig. 1.11 may serve as good examples in order to show how severe such artifacts can be. It might be possible to deal with such artifacts - at least to a certain extent - by incorporating prior shape information, but the success of this strategy depends significantly on the type of the artifacts.

**The Leakage Problem** occurs when the organ to be segmented is surrounded by tissue which has the same physical properties. A first example is provided in Tab. 1.1, where experimentally determined T<sub>1</sub> relaxation times of different brain tissues are given. Obviously, different tissue types can have similar physical properties, i.e. relaxation times, and thus similar intensity values. As a consequence, an organ may hardly be distinguishable from the surrounding tissue, cf. 1.12, and a segmentation algorithm which is guided by intensity information alone might thus *leak* into adjacent tissue. Sometimes, the leakage problem can be overcome by incorporating prior shape information, but the morphological variability can often limit the applicability of such approaches.

**Morphological Variability** The difficulties described above often prohibit the usage of generic segmentation techniques, or more precisely of generic regularization techniques, which only ensure the smoothness of the solution for instance. A typical example is the leakage problem described in Fig.

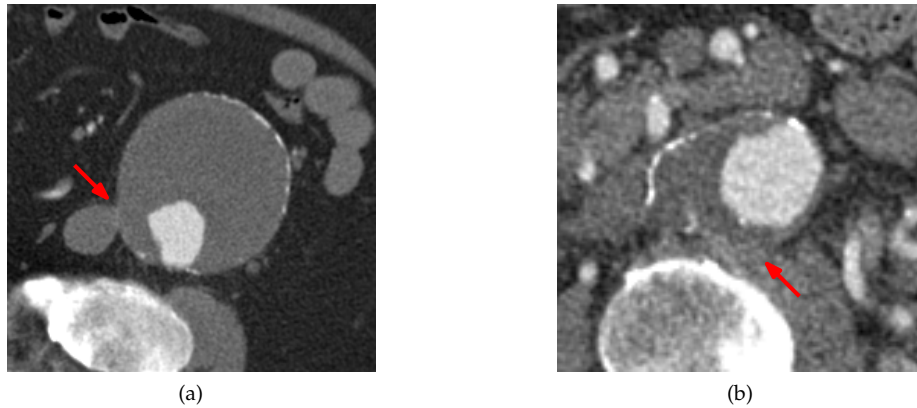


Figure 1.12: **The Leakage Problem:** The thrombus in the wall of abdominal aortic aneurysms is often is hard to distinguish from the surrounding tissue.

1.12, because also a smooth curve may leak into adjacent tissue. In order to overcome such problems one often tries to learn a *shape model* from a set of manually segmented instances as suggested by Cootes [27] for instance. Such a training results in a set of basis functions describing the mean shape and higher moments of variation for instance, and the function space formed by these basis functions can then be used for an implicit regularization. A drawback of this approach is that, if the morphological variability is very high, many training samples are necessary. In order to demonstrate how huge this variability can be, we show a collection of abdominal aortic aneurysms in Fig. 1.13.

**Interaction** There are at least two reasons why fully automatic segmentation systems would be very desirable for clinical applications. Firstly, generating manual segmentations from high resolution 3D or even 3D+t data is very time consuming and often even for diagnostic purposes impracticable, although the time constraints are less tight than in an interventional scenario. Secondly, the possibilities for any interaction in an interventional scenario are very limited due to the fact that the hands of the physicians as well as their assistants are occupied most of the time. Additionally, any interaction in the operating room requires a sterile (or at least sterilizable) interaction device or some kind of gesture or speech recognition system, but even the latter approach might disturb the work flow too much. On the other hand, it is questionable, if fully automatic segmentation systems are the ultimate goal for any kind of application and this question is also closely related to the reproducibility of the system. A typical scenario would be the segmentation and counting of cells in histological data sets, which may consist of several gigabyte of data. If the reproducibility of the result or at least provable bounds for its specificity and sensitivity can be guaranteed, a diagnostic decision based on a fully automatic processing might be acceptable.

A different example would be treatment planning for radiation therapy, where a precise delineation of the tumor(s) is essential in order to protect the

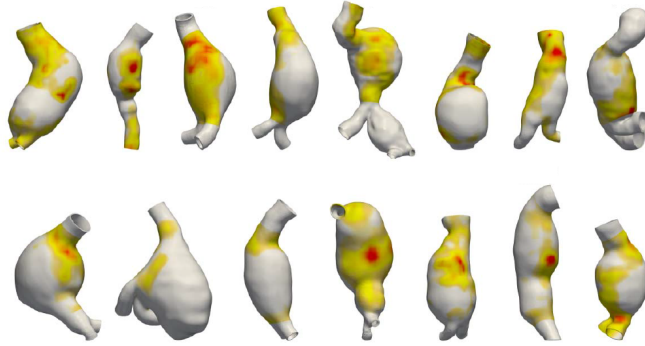


Figure 1.13: **Morphological Variability:** A collection of abdominal aortic aneurysms acquired with PET-CT and colored by FDG-18 uptake values (image courtesy of Andreas Maier).

surrounding tissue as best as possible. Thus, radiation therapy without the possibility of interaction is hard to justify - not only from a legal, but also from an ethical perspective. Moreover, it should be noted that many physicians feel more comfortable when having possibilities for interaction. Concisely put, the ultimate goal is maybe to reduce the amount of user interaction as much as possible while providing intelligent and comfortable user interfaces at the same time. As variational methods, which typically involve several parameters, are of particular interest in this dissertation, we wish to conclude our considerations regarding the interaction by a simple paradigm: Numerical parameters, such as the step size for a gradient descent, should always be chosen by an expert and hidden from the user, whereas model parameters, such as regularization parameters, should have an intuitive meaning making them easy to understand and adjust.

**Reproducibility** is, of course, closely related to the question of interaction, but we wish to briefly elaborate on the mathematical aspect of reproducibility here. The result of a segmentation system is, of course, fully reproducible, if it does not depend on the initialization. Focusing on the scenario described in the last section, full reproducibility can be guaranteed, if the energy to be minimized is (strictly) convex. Indeed, a lot of research on *convexification* has been carried out during the last six years, but there are cases where such approaches are not useful as we shall see in Sec. 4.1. Moreover, it is important to notice that the pose estimation problem cannot be made convex - at least not with the mathematical tools available so far [29]. A simple example for this fact is given in Fig. 1.14. Let us assume that the two circles in 1.14a are two organs and we are interested in just one of them. Even if we are given the perfect shape model in advance, i.e. a circle, an energy encoding this segmentation problem is likely to have two distinct local minima and thus cannot be convex.

**Runtime** The total runtime is, of course, related to the amount of required user interaction and it depends highly on the number of parameters to be

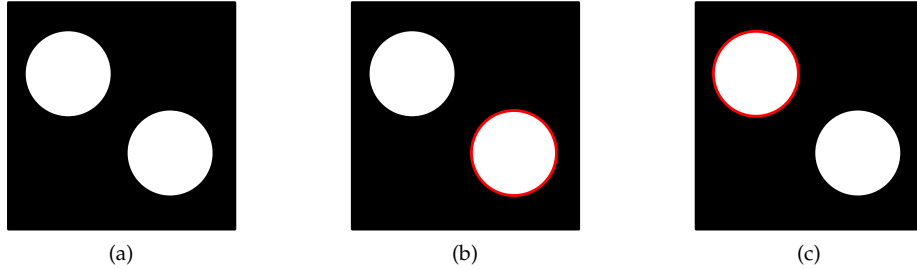


Figure 1.14: **Non-convexity of the Pose Estimation Problem:** An energy for segmenting just one of the circles in (a) is likely to have two distinct local minima - (b) and (c) - and thus cannot be convex.

tuned and on how well the operator can interact with the system via the user interface. As mentioned above, the time constraints may be less restrictive in a diagnostic scenario than in an interventional one, where the result of an algorithm should be available in or close to real time. However, this does not mean that long computation times are acceptable for diagnostic segmentation systems. It might be acceptable, if only an initialization is required and the execution of a segmentation algorithm takes several minutes or even hours, but, if continuous user interaction is needed, long processing times are hardly tolerable. For this reason, the development of efficient numerical schemes is very important, which is also part of this dissertation, cf. Sec. 1.4.

**Validation** The validation of segmentation algorithms can be performed using manually segmented ground truth data or either physical or computational phantoms [88]. Physical phantoms have the advantage that the image acquisition process can be reproduced realistically, but they might have been built based on simplifying anatomical assumptions. In contrast to this, computational phantoms may have a realistic anatomy, but may include simplifying assumptions regarding the image formation process. Manually segmented ground truth data does not have these disadvantages, but the results are hardly reproducible due to inter- and intra observer variabilities [18]. As discussed before, the large anatomical variability of some organs is, of course, another problem requiring a lot of ground truth data sets to be generated which is very cumbersome and time-consuming process. A good strategy in order to deal with all these problems seems to be the automatic combination of multiple expert and algorithm segmentations in order to obtain better ground truth segmentations, e.g. [122]. In the future, large data bases, e.g. the cardiac atlas project ([www.cardiacatlas.org](http://www.cardiacatlas.org)), and segmentation challenges, e.g. the *MICCAI grand challenges* ([www.grand-challenge.org](http://www.grand-challenge.org)), might become more and more important. The benefits of such data bases and challenges are that researches can evaluate their algorithms in a controlled and more objective environment and the submitted results can be used to improve the ground truth data.

## 1.4 Contributions and Outline

The contributions of this dissertation are related to active contour and variational level set methods as well as their efficient implementation and their applications to medical image segmentation.

### Chapter 2 - Active Contours: Advertising the Regularization Strategy as a Taxonomy

Most active contour methods solve a minimization problem of the form

$$\min_{u \in S \subset F} E(u) + \lambda R(u), \quad (1.35)$$

where  $F$  is a function space providing important mathematical structures, e.g. a metric,  $S$  is a subset or even a subspace of more regular or smooth functions, and  $R$  is a regularizer. We will refer to the choice of  $S$  as *implicit regularization strategy* and to the choice of  $R$  as *explicit regularization strategy*, cf. Sec. 1.2. However, active contour methods are often classified with respect to their contour representation (Lagrangian or Eulerian) or with respect to the features guiding them towards the desired boundaries (edge-based or region-based), cf. [62]. As a minor contribution of this dissertation we wish to advertise the usage of the regularization strategy as an additional taxonomy, because

- the curve representation reflects only the way of solving (1.35) numerically and
- a feature-based taxonomy does not reveal any information about the a priori information represented by implicit and explicit regularization.

Besides discussing possible taxonomies we are also going to present a brief history of active contour methods in chapter 2. Finally, we conclude with an overview over most articles cited in this thesis, where we classify each approach based in the taxonomies introduced before.

### Chapter 3 - Variational Level Set Methods: Efficient Methods for $H^1$ - and Tikhonov-type Regularized Variational Level Set Methods

The usage of a regularization strategy, be explicit or implicit, always causes additional computational complexity. As each type of regularization has its own peculiarities, the development of efficient numerical techniques is very important. The contributions proposed in chapter 3 are related to variational level set methods in general and to the development and comparison of the efficient numerical techniques for  $H^1$ - and first order Tikhonov-type regularization strategies. Most of the ideas presented in chapter 3 have been published in the following articles:

- **M. Baust**, D. Zikic, N. Navab. *Diffusion-based Regularisation Strategies for Variational Level Set Segmentation*. Proceedings of the 21st British Machine Vision Conference (BMVC), Aberystwyth, United Kingdom, 2010.

- **M. Baust**, N. Navab. *A Fully Implicit Framework for Sobolev Active Contours and Surfaces*. Proceedings of the 33rd Annual Symposium of the German Association for Pattern Recognition, Frankfurt am Main, Germany, 2011.

#### **Chapter 4 - Polar Active Contours: Translation, Scale, and Deformation Weighted Polar Active Contours**

Chapter 4 contains the main contribution of this dissertation. We translate the concept of Sobolev active contours [110] to polar active contours and endow the resulting Sobolev space with a metric which allows the user to weight translations, scale changes, and smooth deformations of the curve differently. The proposed method has several medical applications such as the segmentation and tracking of abdominal aortic aneurysms or the left ventricular cavity. The ideas presented in chapter 4 can be found in the following articles:

- **M. Baust**, N. Navab. *A Spherical Harmonics Shape Model for Level Set Segmentation*. Proceedings of the 11th European Conference on Computer Vision (ECCV), Crete, Greece, 2010.
- **M. Baust**, A. Yezzi, G. Unal, N. Navab. *A Sobolev-type Metric for Polar Active Contours*. Proceedings of the IEEE Conference on Computer Vision and Pattern Recognition (CVPR), Colorado Springs, USA, 2011.
- **M. Baust**, A. Yezzi, G. Unal, N. Navab. *Translation, Scale, and Deformation Weighted Polar Active Contours*. Journal of Mathematical Imaging and Vision (submitted).

Additionally, we hope that the ideas and results presented in chapter 4 convince the gentle reader that the careful design of implicit regularization strategies is a powerful alternative to the *convexification* of active contour approaches in order to make active contours more global, cf. Sec. 1.1.

#### **Chapter 5 - Conclusion**

In chapter 5 we sum up our findings and discuss several possible directions for further research.

#### **Appendix**

As the ideas presented in this thesis rely heavily on the concept of Sobolev spaces, we present a brief but more mathematical introduction to Sobolev spaces along with some important theorems in appendix A. Finally, all contributions which are not covered by this thesis are listed in appendix B.

# 2

## Active Contours

In this chapter we wish to give an overview over the vast body of literature on active contours. However, it is needless to say that this overview cannot be exhaustive as there are over 10 000 citations<sup>1</sup> of the original work of Kass *et al.* [54]. As a consequence, we aim at providing a *rough impression* of the historical as well as the methodological developments in the field of active contours during the last decades. We start by discussing some important influences from other research areas such as front propagation methods, shape modeling, or variational image restoration in Sec. 2.1. Next, we present possible taxonomies for active contour methods in Sec. 2.2 and employ them for classifying a selection of related works. Thereby, We hope to convince the reader that *regularization* is a very useful taxonomy.

### 2.1 Chronological Overview

Many advances in the area of active contours are due to influences from other research areas such as front propagation methods, shape modeling, edge detection, variational image restoration, and graphical models. For this reason, the history of active contour methods cannot be fitted into a single time line. For a first impression on how diversified the connections to other research areas are, we refer to Fig. 2.1. Of course, Fig. 2.1 highlights only *a few* connections to other areas, but these will be enough to explain *why* they actually exist.

---

<sup>1</sup>According to Google Scholar, August 2011.

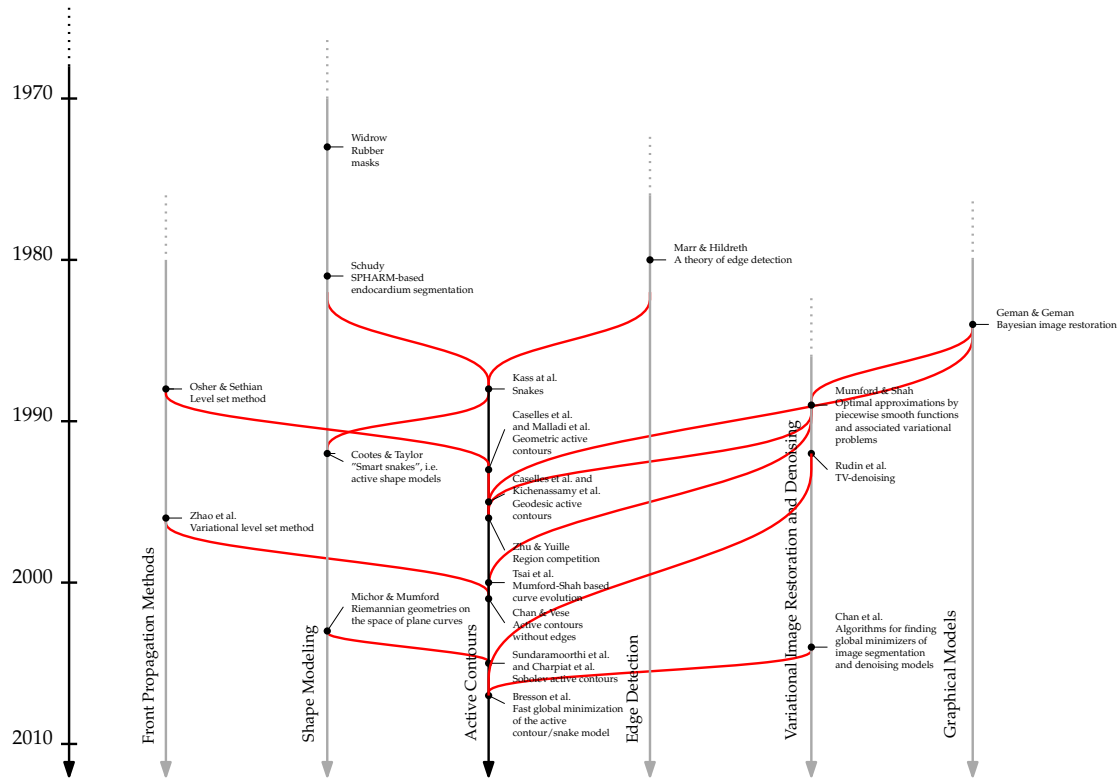


Figure 2.1: **Some Important Influences from Other Research Areas:** Some assignments such as the one of active shape models to the area of shape modeling might, of course, be subject for debate, but we want to emphasize that the main goal of this illustration is to give an *impression* rather than providing a sharp differentiation.

### Shape Modeling and Edge Detection

As indicated in Fig. 2.1, some roots of active contours can be found in the areas of shape modeling and edge detection. The general principle of active contours, i.e. the optimization of an error-measure or cost, which can be regarded as an energy, over a set of basis functions, can already be identified in the *rubber mask* technique of Widrow [125, 126] from 1973. Rubber masks are deformable templates which have been proposed for automatic chromosome analysis and classification. While this technique is somewhere in between model-based registration and segmentation, there is a closer ancestor of active contours proposed by Schudy who developed a method for locating the moving endocardial surface from US data in 1981 [104]. Schudy [104] uses already an implicit regularization, i.e. a spherical harmonics parametrization, and minimizes a cost function. In contrast to this, active contours only use a different cost function, e.g. based on ideas of Marr and Hildreth [68], a different implicit regularization, i.e. splines, and an additional explicit Tikhonov-type regularization.

Active contours again influenced the area of shape modeling by the well known active shape models proposed by Cootes [27] which employ an implicit regularization by a set of basis functions computed from a collection of training shapes. Often, this set of basis functions is obtained by principal component analysis of the coefficients of the employed parametrization. Typical parametrizations are splines [26], (spherical) harmonics [106, 111, 55], wavelets [75], signed distance functions [61, 118], or logarithm of odds based representations [90]. These efforts led, however, to more fundamental questions such as how to compute an average shape in a correct manner [129], because computing statistics in *flat* parameter spaces might not always lead to meaningful shapes as noted in [86] and illustrated in Fig. 2.2. As a consequence, one always has to perform such computations with respect to the underlying manifold *and* the metric defined on it. The role of the metric should not be underestimated which has for instance been demonstrated by Michor and Mumford [71] who found that it makes no sense to measure distances between two curves using the classical  $L^2$  metric. Such considerations again led to a much deeper understanding of active contours and eventually to *Sobolev active contours*, cf. Sundaramoorthi et al. [107, 108, 109, 110] and Charpiat et al. [21], which are also the basis for many ideas presented in this dissertation.

### Level Set Methods

The level set method introduced by Osher and Sethian in [81] was originally developed for tracking fronts whose speed depends on the local curvature, which is the case for crystal growth and flame propagation for instance, but soon after their introduction it has been used as an alternative implementation for active contours. Representing the evolving contour as the zero level set of an embedding function and evolving this function instead has two main advantages. Firstly, topological changes can be handled naturally. Secondly, no thought about the parametrization of the curve has to be wasted, because the parametrization of the curve, i.e. the zero level set, is automatically intrinsic.

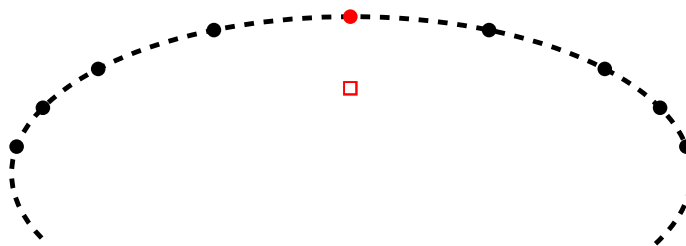


Figure 2.2: **Computing Statistics on Manifolds:** Computing the mean value of the black points with respect to their two dimensional coordinates yields a different result (red square) than computing it with respect to the dashed manifold (red point).

As the necessity for removing the dependency on the parametrization of active contours and the convenient handling of topological changes became obvious in [15, 66] the level set method entered the arena of active contours. Soon after its introduction it also smoothed the way for the well-known geodesic active contours [16, 56].

Several years later, a variant of the level set method the so-called variational level set method [130] became famous by the work of Chan and Vese [20] who used this method for modeling and minimizing a two phase piecewise constant variant of the Mumford-Shah model [74]. The advantage of the variational level set method is that the evolution equation for the embedding function is derived from an energy which is defined for the embedding function itself. In contrast to this, most approaches which are based on the original level set method derived a so-called speed function from an energy defined on the contour and used this speed function for advecting the embedding function, which requires the extension of this speed function to (at least) a narrow band around the zero level set. Besides this obsolete extension step, the main advantage of the variational level set method is that the design of energies using smeared-out approximations of the Heaviside and Dirac distribution is very convenient. On the other hand, it should be noted that such Eulerian techniques are always a bit less geometric in the sense that the evolution of the zero level set might be different from the evolution of the curve it represents.

### Graphical Models and Variational Image Restoration

Graphical models are graph-based probabilistic models, where the nodes represent (groups of) random variables and the edges the probabilistic relationship between them [10]. The way of decomposing the joint distribution over all of these random variables into a product of factors which depend only on subsets of these variables is then captured by the connectivity relationships modeled by the graph. Depending on whether this graph is directed or not, we call the graphical model either *Bayesian network* or *Markov random field* (MRF) [10]. Such a MRF formulation for image restoration has been proposed by Geman and Geman in 1984 [40] which is also closely related to the spatially continuous and variational formulation of Mumford and Shah [74]. As visualized in Fig. 2.1,

these two models had a significant influence on active contour methods. The reason for this development lies in the nature of active contours itself. Active contours are designed for interactive image interpretation and the solution of low-level vision problems such as the detection of edges, lines, and subjective contours by means of energy minimization. The focus is thereby on “energy functions whose local minima comprise the set of alternative solutions available to higher-level processes” [54]. In other words, active contours are local on purpose and designed to depend on the initialization. For some applications, however, their very local behavior as well as their strong dependency on the initialization might not be desired. A first hint on how active contours can be globalized is provided by the observation that there are in two possible ways of describing an object, cf. [57]. One possible way is to describe it by the properties of the boundary, e.g. a high magnitude of the image gradient. Another possibility consists in finding one or more features, e.g. object color or texture, by which the object region itself can be distinguished from the background. In the simplest case, the object can be described by a different gray value leading immediately to the piecewise constant Mumford-Shah model [74]. Vice versa, the class of piecewise constant images is very easy to segment by active contours making it even more comprehensible why incorporating ideas from variational image restoration have been used for globalizing active contours. One of the first approaches on the way to region based active contours can be seen in the region competition approach of Zhu and Yuille [131], but a more direct application of the ideas presented in [74] was however presented by Tsai *et al.* [119] as well as Chan and Vese [20]. The combination of [20] with ideas from total variation based denoising [97] and convex optimization [76] finally led to the first convex active contour models, e.g. [13].

## 2.2 Taxonomies for Active Contours

Besides regularization, there are several other possibilities of classifying active contour methods such as the way they are implemented, the question of convexity, and the features they employ. In Tab. 2.1 we tried to classify most of the cited articles in this thesis based on these taxonomies. The selection of the presented articles is, of course, biased due to the fact that this dissertation mainly focuses on Sobolev-type implicit regularizations and medical applications. For this reason, we put less emphasis on convex approaches, e.g. [13], various ways of integrating color, texture, and motion information, e.g. [82, 83], or shape and appearance models [26, 25], but we still hope that the reader gets a good impression on the diversity of the vast literature on (generalized) active contour methods. Further, we hope that the presented overview convinces the reader that regularization is a very distinctive taxonomy. Before that, however, we want to briefly recall the above mentioned criteria.

### Implementation

There are several ways of implementing a curve or surface evolution:

- The **Lagrangian** approach aims at tracking each (infinitesimal or discretized) surface element as it evolves through space and time. A typical example would be the discretization of a curve by splines [54].
- The level set method (**LSM**), cf. [81], corresponds to the *Eulerian way* of evolving a curve or surface by discretizing the surrounding space, representing the surface by the zero level set of a so-called *embedding function*, and evolving this embedding function instead of discretizing and evolving the curve or surface itself.
- The variational level set method (**VLSM**), cf. [130], is also often used for curve and surface evolution as it allows for flexible modeling as well as the direct derivation of the evolution equation for the embedding function, cf. Sec. 2.1 and chapter 3.
- In order to include convexified active contour methods, e.g. [13], we also consider *labeling functions*, i.e. functions taking values in the range from 0 to 1. As these methods evolved from the variational level set method we term them convex variational level set methods (**cVLSMs**).

The categories given above lead, however, to the wrong conclusion that a clear distinction between a Lagrangian and an Eulerian approaches is always possible. In fact, it may happen that an (Eulerian) approach based on the level set method, requires a (Lagrangian) polygon representation for re-initializing the embedding function to a signed distance function, e.g. [15]. Vice versa, even with a polygon representation at hand it might be better to compute quantities such as the curvature using a level set representation, cf. [110].

### Convexity

Another important classification criterion is whether the minimized energy is convex or not. Although the answer to this question is a binary one, the following aspects should be considered:

- Minimizing a convex energy one usually expects to find a global minimum, but it should be noted that the convexified version of the well-known Chan-ese model [20] for instance, which is discussed in [13], is only convex but not strictly convex, cf. Sec. 3.1. Moreover, convexity is often achieved by so-called relaxation techniques, which means that one actually computes a *soft segmentation*, i.e. a function taking values in  $[0, 1]$ . As a consequence, there are several global minimizers which can be obtained by thresholding this soft segmentation [76, 13]. In practice, however, it turns out that the computed soft segmentation is often almost binary making the selection of the threshold a negligible issue.
- Active contours are meant to be local, because the original intention of active contours is to find local solutions to the edge detection problem. In [54] it is mentioned that some high level mechanism could interact with the contour model by "pushing it toward an appropriate local minimum". The most obvious high level mechanism is, of course, the user itself and for this reason, the original approach contained also an energy modeling user constraints. The current efforts for convexifying variational approaches in computer vision are for sure important and interesting, but convex approaches might not always provide us with meaningful results as it is demonstrated in Sec. 4.1. Another important aspect is that there is - at least so far - no way to convexify the pose estimation problem, even if prior shape information is available, cf. [29]. Besides making the above mentioned high level mechanism obsolete by means of convexification, the intelligent design of such high level mechanisms might be another promising research direction. An excellent example is given by the work of Grbić *et al.* [43], where the initial position of a complex shape model of the heart is found in a very elegant and robust way based on state of the art machine learning algorithms.

However, it should be noted again that we consider convexified approaches only in order to complete the picture rather than providing an exhaustive overview on them.

### Driving Features

A relatively common taxonomy are the features by which the evolution of the contour or surface is driven. One typically distinguishes between **edge-based** and **region-based** approaches. Edge-based features are the gradient magnitude for instance, or any other response of an edge detector. Possible region-based features could be gray value, color, or texture; for a good overview we refer to [28]. If both kinds of information are used, we call the approach **hybrid**. In addition to these categories we introduce the category **generic**

in order to indicate that an approach focuses on a certain optimization or regularization strategy rather than on the usage of certain features or on a particular application.

As in the case of implementation, a clear distinction is sometimes not possible as it is shown by the following example. Denoting the evolving contour or surface by  $\mathcal{S}$ , one could argue to the incorporation of region information often involves the minimization of the weighted area integral

$$\int_{\text{int}\mathcal{S}} f \, dx, \quad (2.1)$$

where  $f : \Omega \rightarrow [0, \infty)$  is a function encoding this information and  $\text{int}\mathcal{S}$  denotes the region enclosed by  $\mathcal{S}$ . The simplest choice  $f \equiv 1$ , however, leads to the balloon force proposed by Cohen and Cohen [23], but this model is used in several approaches such as the geodesic active contours [16, 56] which are often considered as edge-based. Such considerations might be pedantic, because the region information is only generic, but we want to avoid the impression that the classifications in Tab. 2.1 are considered as unalterable.

### Regularization

Most of the approaches in Tab. 2.1 are related to a minimization problem of the form

$$\min_{u \in S \subset F} E(u) + \lambda R(u), \quad (2.2)$$

where  $u$  is either an Eulerian or Lagrangian representation of the curve or surface,  $S$  is a subset of a function space  $F$ , and  $R$  is an explicit regularizer. The distinction between  $S$  and  $F$  is needed, because as in the case of level set methods, the restriction to the set of signed distance functions comprises an implicit regularization, but this set is not a function space. Thus, structural properties, such as a vector space structure or a metric, have to be provided by a function space containing this subset, e.g.  $L^2$ . Often,  $S$  is chosen as a subspace of  $F$  spanned by a finite number of basis functions, such as (spherical harmonics), wavelets, or eigenmodes with respect to some parametrization, but also infinite dimensional choices, such as  $H^1$  or  $C^\infty$ , are possible<sup>2</sup>. As far as explicit regularizers are concerned we can distinguish between regularizers based on derivatives of  $u$ , such as Tikhonov-type regularizers [113], total variation based regularizers, signed distance regularizers (cf. [63, 64]), curvature based regularizers, or the curve length<sup>3</sup>, and regularizers based on the coefficients of some parametrization of  $u$ . A typical example for the latter case are regularizers which encode assumptions on the distribution of the trained basis functions, e.g. [29].

---

<sup>2</sup>Of course, when implementing an algorithm one always ends up with a finite dimensional representation, but we want to indicate the conceptual difference at this point.

<sup>3</sup>The derivative is often hidden in the definition of the arc-length.

approach	year	implementation	convex	driving features	explicit regularization	implicit regularization
<b>Widrow</b> [125, 126]	1973	deformable pattern matching	-	region-based	thresholds on parameters	parametrized stereotypes
<b>Schudy</b> [104]	1981	Lagrangian	-	region-based	-	(spherical) harmonics
<b>Terzopoulos</b> [113]	1986	Lagrangian	-	generic	Tikhonov-type	splines
<b>Kass <i>et al.</i></b> [54]	1988	Lagrangian	-	edge-based	Tikhonov-type & user constraints	splines
<b>Friedland <i>et al.</i></b> [39]	1989	Lagrangian	-	edge-based	finite difference based smoothness regularizer	MRF-parametrized polar description
<b>Terzopoulos &amp; Metaxas</b> [114]	1991	Lagrangian	-	generic	Tikhonov-type	super-quadratics
<b>Cootes <i>et al.</i></b> [27]	1992	Lagrangian	-	edge-based	coefficient regularizer	set of trained basis functions
<b>Figueiredo</b> [37]	1992	Lagrangian	-	region-based	finite difference based smoothness regularizer	MRF-parametrized polar description
<b>Caselles <i>et al.</i></b> [15]	1993	LSM	-	edge-based	curve length	signed distance functions
<b>Chohen &amp; Cohen</b> [23]	1993	Lagrangian	-	edge-based	Tikhonov-type	finite elements
<b>Pentland</b> [87]	1993	Lagrangian	-	n/a	n/a	eigenmodes
<b>Vemuri <i>et al.</i></b> [121]	1993	Lagrangian	-	edge-based	Tikhonov-type	wavelets
<b>Malladi <i>et al.</i></b> [66]	1994	LSM	-	edge-based	curve length	signed distance functions
<b>Caselles <i>et al.</i></b> [16]	1995	LSM	-	edge-base	weighted curve length	signed distance functions
<b>Kichenassamy</b> [56]	1995	LSM	-	edge-based	weighted curve length	signed distance functions
<b>Malladi <i>et al.</i></b> [67]	1995	LSM	-	edge-based	curve-length	signed distance functions
<b>Dias <i>et al.</i></b> [31]	1996	Lagrangian	-	region-based	finite difference based smoothness regularizer & additional constraints	MRF-parametrized polar description

<b>Floreby <i>et al.</i></b> [38]	1996	Lagrangian	-	edge-based	Tikhonov-type	polar description
<b>Staib &amp; Duncan</b> [106]	1996	Lagrangian	-	edge-based	coefficient regularizer	harmonics
<b>Szekely <i>et al.</i></b> [111]	1996	Lagrangian	-	edge-based	curvature-based	eigenmodes based on spherical harmonics
<b>Zhao <i>et al.</i></b> [130]	1996	VLSM	-	generic	n/a	parametrization signed distance functions
<b>Caselles <i>et al.</i></b> [17]	1997	LSM	-	edge-base	weighted curve length	signed distance functions
<b>Xu &amp; Prince</b> [127]	1997	Lagrangian	-	edge-based	Tikhonov-type	splines
<b>Yezzi <i>et al.</i></b> [128]	1997	LSM	-	edge-based	weighted curve length	signed distance functions
<b>Schnörr</b> [102]	1998	cVLSM	✓	region-based	total variation	<i>BV</i>
<b>Denzler &amp; Niemann</b> [30]	1999	Lagrangian	-	edge-based	Tikhonov-type	polar description
<b>Gomes &amp; Faugerás</b> [41]	1999	LSM	n/a	generic	n/a	signed distance functions with additional PDE constraints
<b>Kelemen <i>et al.</i></b> [55]	1999	Lagrangian	-	edge-based	coefficient regularizer	eigenmodes based on spherical harmonics parametrization
<b>Leventon <i>et al.</i></b> [61]	2000	LSM	-	hybrid	coefficient regularizer	eigenmodes based on signed distance functions
<b>Tsai <i>et al.</i></b> [119]	2000	Lagrangian	-	hybrid	curve length	signed distance functions
<b>Chan &amp; Vese</b> [20]	2001	VLSM	-	region-based	weighted curve length	signed distance functions
<b>Paragios &amp; Deriche</b> [83]	2002	LSM	-	hybrid	weighted curve length	signed distance functions
<b>Tsagaan <i>et al.</i></b> [117]	2002	Lagrangian	-	edge-based	shape-regularizer	Non-Uniform Rational B-Spline
<b>Tsai <i>et al.</i></b> [118]	2004	VLSM	-	generic	-	eigenmodes based on signed distance functions
<b>Chambolle</b> [19]	2004	cVLSM	n/a	generic	total variation	n/a
<b>Fernandez</b> [36]	2004	Lagrangian	-	region-based	finite difference based smoothness regularizer	MRF-parametrized polar description

<b>Hintermüller &amp; Ring</b> [47]	2004	VLSM	-	hybrid	Tikhonov-type	preconditioner could be considered as projector into a certain subspace
<b>Hu et al.</b> [50]	2004	Lagrangian	-	edge-based	Tikhonov-type	polar description
<b>Ray et al.</b> [93]	2004	Lagrangian	-	region-based	curve length	polar description
<b>Ho et al.</b> [48]	2005	LSM	n/a	generic	-	unstructured point cloud
<b>Li et al.</b> [63]	2005	VLSM	n/a	generic	signed distance regularizer	$L^2$
<b>Morse et al.</b> [72]	2005	LSM	-	edge-based	curve length	radial basis functions
<b>Yezzi &amp; Mennuci</b> [129]	2005	LSM	n/a	generic	-	$L^2$ , but endowed with conformal metric
<b>Nikolova et al.</b> [76]	2006	cVLSM	✓	generic	total variation	labeling functions normalized to $[0, 1]$
<b>Charpiat et al.</b> [21]	2007	LSM	n/a	generic	n/a	$H^1$ & $C^\infty$
<b>Bresson et al.</b> [13]	2007	cVLSM	✓	hybrid	total variation	labeling functions normalized to $[0, 1]$
<b>Eckstein et al.</b> [34]	2007	Lagrangian	n/a	generic	n/a	$H^1$
<b>Nain et al.</b> [75]	2007	Lagrangian	-	region-based	-	eigenmodes based on spherical wavelets parametrization
<b>Slabaugh et al.</b> [105]	2007	VLSM	-	region-based	curve length	anisotropic radial basis functions
<b>Sundaramoorthi et al.</b> [110]	2007	LSM	n/a	generic	n/a	Sobolev spaces in general, $H^1$ in particular
<b>Cremers et al.</b> [29]	2008	cVLSM	✓ (only shape)	generic	coefficient regularizer	trained labeling functions normalized to $[0, 1]$
<b>Gooya et al.</b> [42]	2008	VLSM	-	hybrid	-	signed distance functions
<b>Huang et al.</b> [52]	2008	VLSM	-	hybrid	-	signed distance functions & free form deformations
<b>Lankton et al.</b> [59]	2008	VLSM	-	hybrid	-	signed distance functions
<b>Li et al.</b> [62]	2008	VLSM	-	region-based	signed distance regularizer & curve length	$L^2$

<b>Liang et al.</b> [65]	2008	Lagrangian	-	edge-based	Tikhonov-type & shape regularizer	polar representation
<b>Paragios et al.</b> [84]	2008	VLSM	-	generic	shape regularizer	signed distance functions
<b>Sundaramoorthi et al.</b> [108]	2008	LSM	-	generic	-	$H^1$
<b>Sundaramoorthi et al.</b> [109]	2008	LSM	-	generic	-	$H^1$
<b>Bar et al.</b> [3]	2009	VLSM	-	generic	-	$H^1$ & $C^\infty$
<b>Benoit et al.</b> [73]	2009	VLSM	-	generic	-	non-Euclidean image-adaptive radial basis functions
<b>Bernard et al.</b> [8]	2009	VLSM	-	generic	-	B-splines
<b>Collewet et al.</b> [24]	2009	Lagrangian	-	area-based	Tikhonov-type	spherical harmonics
<b>Li</b> [64]	2010	VLSM	-	generic	signed distance regularizer	$L^2$
<b>Baust &amp; Navab</b> [4]	2010	VLSM	-	generic	coefficient regularizer	spherical harmonics
<b>Baust et al.</b> [7]	2010	VLSM	-	generic	Tikhonov-type	$L^2$
<b>Chen et al.</b> [22]	2010	LSM	-	generic	-	signed distance functions including an elegant velocity projection
<b>Sundaramoorthi et al.</b> [107]	2010	LSM	-	generic	-	$H^1$
<b>Baust et al.</b> [6]	2011	Lagrangian	-	generic	-	$H^1$ & polar description
<b>Baust et al.</b> [5]	2011	VLSM	-	generic	-	signed distance functions & $H^1$ for zero level set

Table 2.1: **Related Work on Active Contours:** Approaches in red are closely related to this dissertation.

# 3

## Variational Level Set Methods

The core idea of active contours [54] is to evolve a curve  $c$  towards the desired object boundaries via the evolution equation

$$\partial_t c = F \mathbf{n}, \quad (3.1)$$

where  $F$  is a speed function depending on the image and  $\mathbf{n}$  denotes the unit outward normal of  $c$ . A possible way of implementing this evolution is the *level set method* [81, 79, 80] which relies on an implicit representation of the evolving curve  $c$  or surface  $\mathcal{S}$ . In order to simplify the notation we will denote any curve or surface by  $\mathcal{S} \subset \Omega \subset \mathbb{R}^d$  ( $d = 2, 3$ ) throughout the rest of this chapter. Now, we can represent  $\mathcal{S}$  as the zero level set of a *signed distance function*  $\phi : \Omega \subset \mathbb{R}^d \rightarrow \mathbb{R}$  defined as

$$\phi(x) = \begin{cases} -d(x, \mathcal{S}), & \text{if } x \text{ is inside } \mathcal{S}, \\ 0, & \text{if } x \text{ is on } \mathcal{S}, \\ +d(x, \mathcal{S}), & \text{if } x \text{ is outside } \mathcal{S}, \end{cases} \quad (3.2)$$

where  $d(x, \mathcal{S})$  denotes the (Euclidean) distance to the surface at  $x$ , cf. Fig. 3.1. The two main advantages of the level set approach are that topological changes during the evolution are handled automatically and that no care about the parametrization of the surface has to be taken.

Instead of directly evolving the curve or surface we then evolve the embedding function  $\phi$  by solving the advection equation

$$\partial_t \phi = F \mathbf{n} \cdot \nabla \phi = F \frac{\nabla \phi}{|\nabla \phi|} \cdot \nabla \phi = F |\nabla \phi|, \quad (3.3)$$

where we have used the fact that the unit outward normal of  $\mathcal{S}$  is given by  $\mathbf{n} = \nabla \phi / |\nabla \phi|$ . At first sight, this Eulerian approach to curve evolution seems to be very convenient, but the gained advantages are not for free and the following aspects should be considered:

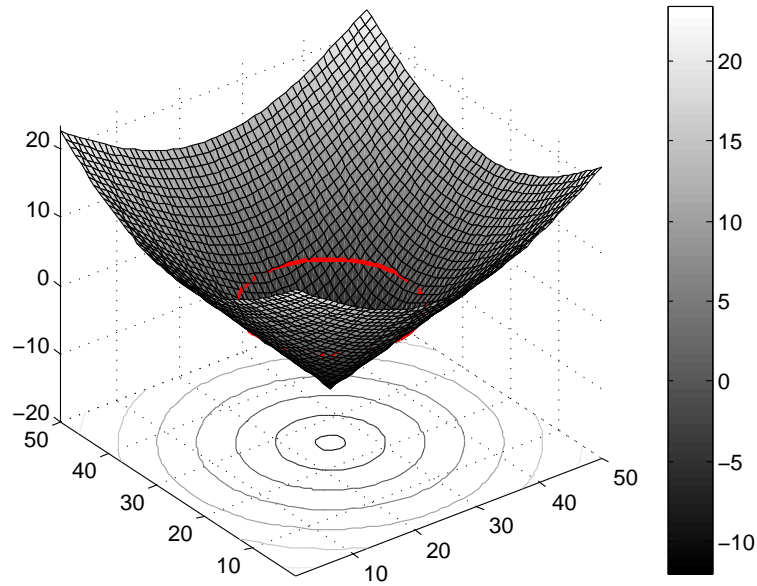


Figure 3.1: **Signed Distance Representation:** A circle (red) is implicitly represented by a signed distance function.

1. Using an  $n + 1$  dimensional embedding function in order to store an  $n$  dimensional surface is not very efficient from a computational point of view. In order to achieve a memory footprint which is comparable to the one of Lagrangian approaches one has to restrict the embedding function to a *narrow band* storing only the function values which are in a small vicinity of the zero level set. It is, however, not trivial to find an efficient data structure for storing the narrow band and a lot of research has been carried out in this area. For a more recent article on this topic we recommend the paper of Houston *et al.* [49].
2. The speed function  $F$  is usually derived for the evolving curve or surface and thus only defined on the zero level set. As a consequence,  $F$  has to be extended to the narrow band mentioned above [79, 80].
3. The numerical solution of (3.3) requires the usage of *upwind schemes*, i.e. special finite difference schemes which adapt to the direction of information propagation, in order to guarantee numerical stability, cf. [79]. In addition to this, the embedding function usually deviates from being a signed distance function during the evolution making periodic re-initialization or the usage of additional regularizers necessary [85, 63].

A popular variant of the level set method has later been proposed by Zhao *et al.* which is called the *variational level set method* [130] and a well-known application of the variational level set method to image segmentation is the work of Chan and Vese [20]. The main difference to the classical level set method is that the evolution equation is derived for the embedding function

---

*itself*. In contrast to this, the evolution equation for the classical level set method is just a plain advection equation where the speed function has been extended to the narrow band, cf (3.3).

It is important to note though that the variational level set method is not *geometric*, cf. [22]. The reason is that computing the first variation with respect to the embedding function is different from computing the first variation with respect to the curve or surface itself, because the set of curves for instance is a *manifold*, cf. [70], while the space of corresponding embedding functions is usually treated as a *flat* function space<sup>1</sup>. As a consequence, also the evolution of the zero level set of  $\phi$  may be different from the evolution of  $\mathcal{S}$ .

Nevertheless, the variational level set method has been used extensively for image segmentation purposes during the last decade and this success has mainly two reasons. Firstly, for plain segmentation purposes only the final configuration of the zero level set may be of interest and not the way of getting there. The situation is, however, very different for tracking applications, cf. [108], where the object in the subsequent frame may only be found by a geometrically meaningful evolution. Secondly, the variational level set method can be summarized by a flexible and simple recipe:

1. Use approximations of the Heaviside function and its distributional derivative, such as the  $C^2$  continuous and compactly supported functions

$$H_{2,\epsilon}(\phi) = \begin{cases} 0, & \phi < \epsilon, \\ \frac{1}{2} + \frac{\phi}{2\epsilon} + \frac{1}{2\pi} \sin\left(\frac{\pi\phi}{\epsilon}\right), & |\phi| \leq \epsilon, \\ 1, & \epsilon < \phi, \end{cases} \quad (3.4)$$

$$\delta_{2,\epsilon}(\phi) = \begin{cases} \frac{1}{2\epsilon} + \frac{1}{2\epsilon} \cos\left(\frac{\pi\phi}{\epsilon}\right), & |\phi| \leq \epsilon, \\ 0, & |\phi| > \epsilon, \end{cases} \quad (3.5)$$

as described in [79], in order to design an energy  $E$  such that the desired configuration of  $\phi$  is at least a local minimum of

$$\min_{\phi \in \mathcal{S}_{\text{SDF}} \subset L^2} E(\phi), \quad (3.6)$$

where  $\mathcal{S}_{\text{SDF}}$  denotes the set of signed distance functions.

2. Apply the calculus of variations in order to obtain  $\nabla_{L^2} E(\phi)$ :

$$\left. \frac{d}{ds} E(\phi + s\psi) \right|_{s=0} = \int_{\Omega} \nabla_{L^2} E(\phi) \cdot \psi \, dx = \langle \nabla_{L^2} E(\phi), \psi \rangle_{L^2} = 0. \quad (3.7)$$

3. Solve (3.6) via gradient descent, which leads to the continuous evolution equation

$$\partial_t \phi = -\nabla_{L^2} E(\phi) \quad (3.8)$$

---

<sup>1</sup>One may argue that the set of valid embedding functions, i.e. the set of all embedding functions which correspond to a shape, is also a manifold. However, in most articles on variational level set methods this fact is largely ignored and the first variation is computed with respect to the *flat* function space  $L^2(\Omega) = \{u : \Omega \rightarrow \mathbb{R} : \|u\|_{L^2} < \infty\}$ .

and the discrete update equation obtained by a forward Euler discretization of  $\partial_t \phi$ :

$$\phi^{t+\tau} = \phi^t - \tau \nabla_{L^2} E(\phi^t). \quad (3.9)$$

Thereby, we have to re-initialize  $\phi^t$  from time to time in order to guarantee that  $\phi^t \in S_{\text{SDF}}$ .

As already indicated in (3.7), the recipe described above assumes a standard  $L^2$  framework leading to a  $L^2$  gradient descent. Unfortunately, the  $L^2$  gradient is, to put it simply, too local and therefore prone to lead into an undesired local minimum (cf. [21, 110] or Fig. 1.9). Thus, either explicit or implicit regularization strategies are necessary.

In the remainder of this chapter we shall consider explicit Tikhonov-type as well as implicit  $H^1$ -type regularization strategies for variational level set methods. We will shine a light on the connection between these two strategies in the non-geometric case in Sec. 3.1 and we will try to develop an almost geometric  $H^1$ -regularized variational level set method in Sec. 3.2.

## 3.1 The Non-geometric Case

In this section we discuss possible explicit and implicit regularization strategies for variational level set methods in the non-geometric case with particular emphasis on  $H^1$ -regularization and first-order Tikhonov-type regularizations. By *non-geometric* we mean that not only the first variation is computed with respect to the flat function space  $L^2(\Omega)$ , but also that the assumption of  $\phi$  being a signed distance function may be completely dropped. A consequence of this relaxation is that the support of the smeared-out Heaviside and Dirac distributions is then depending on the slope of the embedding function. This might seem suspicious at first sight, but we will present a general framework for variational level set methods now, which will help us to understand the implications of this relaxation much better.

### 3.1.1 Generalizing Variational Level Set Methods

We are going to present a general framework which will allow us to classify not only variational level set approaches, but also convexified approaches such as the one presented in [13]. As a byproduct, we gain a deeper insight into the problem of convexifying active contour methods and the associated problems.

Considering variational level set methods from a very abstract point of view one can identify the following ingredients:

- A **function space**  $F$  which is at least endowed with a metric, such as a Banach or Hilbert space, e.g.  $F = L^2(\Omega)$ ,
- a **subset**  $S \subset F$  of this function space which actually contains the embedding functions and allows us to weave in an implicit regularization, e.g. the set of signed distance functions,
- an **explicit regularizer**  $R : F \rightarrow \mathbb{R}$ , e.g. a Tikhonov-type regularizer,

- a differentiable **binarization operator**  $\mathbf{B} : \mathbb{R} \rightarrow [0, 1]$ , e.g.  $\mathbf{B} = H_{2,\epsilon}$  in (3.4), which allows us to formulate weighted area integrals

$$\int_{\Omega} \mathbf{B}(\pm\phi) f \, dx, \quad (3.10)$$

and a weighted surface integral

$$\int_{\Omega} \mathbf{B}'(\phi) \nabla\phi \cdot \frac{\nabla\phi}{|\nabla\phi|} g \, dx = \int_{\Omega} \mathbf{B}'(\phi) |\nabla\phi| g \, dx, \quad (3.11)$$

where  $f, g : \Omega \rightarrow \mathbb{R}$  can depend on the embedding function  $\phi$  as well as the image data to be segmented, and finally

- a **reprojection operator**  $\mathbf{P} : F \rightarrow S$  which can be used to project iteratively computed solutions back into the set  $S$ , e.g. the re-initialization of a function to a signed distance function.

Putting everything together we might end up with a minimization problem of the form

$$\min_{\phi \in S \subset F} E(\phi) + \lambda R(\phi), \quad (3.12)$$

where  $E$  is for instance given by

$$E(\phi) = \int_{\Omega} \mathbf{B}(\phi) f \, dx + \gamma \int_{\Omega} \mathbf{B}'(\phi) g |\nabla\phi| \, dx. \quad (3.13)$$

Depending on the function space  $F$  as well as the structure of minimization problem in (3.12) we can choose different algorithms for computing the solution to (3.12), but during the following considerations we will rely on gradient descent. In order to be able to compute gradients, a Hilbert space framework would be desirable and so we assume that  $F = L^2(\Omega)$  in the following. This allows us to formulate a generic optimization strategy for solving (3.12):

1. Compute the first variation of the regularized energy

$$\left. \frac{d}{ds} [E(\phi + s\psi) + \lambda R(\phi + s\psi)] \right|_{s=0} = \langle \nabla_{L^2} E(\phi) + \lambda \nabla_{L^2} R(\phi), \psi \rangle_{L^2} = 0. \quad (3.14)$$

2. Perform a gradient descent

$$\phi^{t+\tau} = \phi^t - \tau [\nabla_{L^2} E(\phi^t) + \lambda \nabla_{L^2} R(\phi^t)]. \quad (3.15)$$

3. Use the reprojection operator  $\mathbf{P}$  in order to guarantee that the updated solution  $\phi^{t+\tau}$  is still an element of  $S$ , if necessary. If the subset  $S$  has a vector space structure, it is only necessary to project  $\nabla_{L^2} E(\phi^t) + \lambda \nabla_{L^2} R(\phi^t)$  onto  $S$  before applying the update step in (3.15). In the case of signed distance functions this is for instance not the case and thus one has to re-initialize the updated solution  $\phi^{t+\tau}$ .

Based on these very general considerations we will now review several implicit and explicit regularization strategies.

### 3.1.2 Implicit Regularization Strategies

As discussed in Sec. 1.2 it is, of course, possible to combine an implicit with an explicit regularization, but in order to simplify the following considerations we will assume w.l.o.g. that no explicit regularization is used.

#### Signed Distance Functions

An implicit regularization corresponds to the choice of  $S$  in (3.12) and the most common example for such an implicit regularization is probably the restriction of  $\phi$  to the set of signed distance functions. Unfortunately, signed distance functions do not form a function space in the mathematical sense as the sum of two signed distance functions is not a signed distance function for instance. As a consequence, we need to periodically re-initialize the computed updates  $\phi^{t+\tau}$ , cf. [67, 20, 130]. This also determines the re-projection operator  $\mathbf{P}$ , but we will avoid a discussion on how to implement this re-initialization and refer the interested reader to [85] and [79] instead. Finally, it should be mentioned that Chen *et al.* recently proposed a technique for converting level set gradients to shape gradients [22]. This technique tries to modify the computed update such that the resulting function is again a signed distance function, but it is unfortunately only applicable in two dimensions - at least so far.

The choice of the set  $S$  is closely related to the choice of the binarization operator. One possibility in the case of signed distance functions is  $\mathbf{B} = H_{2,\epsilon}$ , cf. (3.4), but we will see now why this is perhaps not the best choice. If we assume that  $E$  has the generic form described in (3.13) and that there is no explicit regularization, the gradient descent step in (3.15) can be written as

$$\phi^{t+\tau} = \phi^t - \tau \mathbf{B}'(\phi^t) U(\phi^t), \quad (3.16)$$

where  $U(\phi) = \left[ f - \gamma \operatorname{div} \left( g \frac{\nabla \phi}{|\nabla \phi|} \right) \right]$ . Having a closer look at (3.16) we observe that the velocity of the level sets

$$\phi_c^t = \{x \in \Omega : \phi^t(x) = c \in \mathbb{R}\} \quad (3.17)$$

is not only depending on the step size  $\tau$ , but also on the derivative of the binarization operator  $\mathbf{B}'(\phi^t)$ , which is also visualized in Fig. 3.2a. We observe that for the choice  $\mathbf{B}(\phi) = H_{2,\epsilon}(\phi)$ , cf. (3.4), only the level sets for  $c \in (-\epsilon, +\epsilon)$  are evolving. This restricts the evolution to a narrow band

$$N_\epsilon = \{x \in \Omega : \delta_{2,\epsilon}(\phi) > 0\} \quad (3.18)$$

around the zero level set, cf. Fig. 3.2.

In contrast to this, Chan and Vese [20] proposed to use the  $C^\infty$  continuous and *non-compactly* supported approximation of the Heaviside function

$$H_\epsilon(\phi) = \frac{1}{2} \left( 1 + \frac{2}{\pi} \arctan\left(\frac{\phi}{\epsilon}\right) \right) \quad (3.19)$$

causing *all* level sets to evolve. Although  $E$  in (3.13) is in general not convex, Chan and Vese argue that by using a non-compactly supported approximation

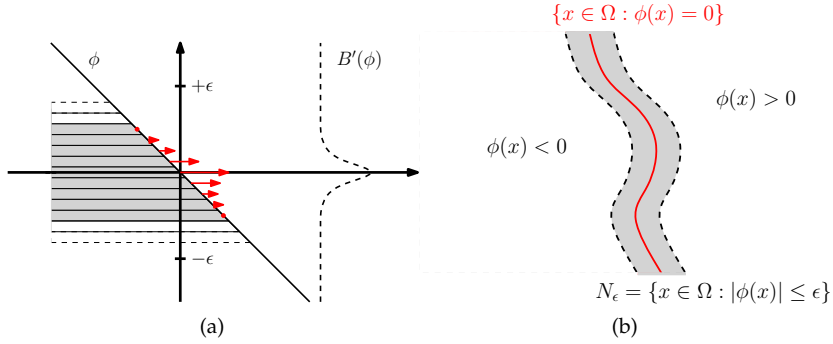


Figure 3.2: **Evolving Level Sets:** The velocity of the level sets of  $\phi$ , drawn as gray and white layers in (a), is depending on  $\mathbf{B}'(\phi^t)$ . We depict the situation for  $\phi$  being a signed distance function and  $\mathbf{B} = H_{2,\epsilon}$ . The level sets drawn in gray evolve with positive speed while the ones drawn in white stagnate as  $\mathbf{B}'(\phi_c^t) = 0$  for all  $c \in \mathbb{R} \setminus (-\epsilon, +\epsilon)$ . This restricts the evolution to a narrow band  $N_\epsilon$  around the zero level set (b).

such as (3.19) the algorithm would have a “tendency to compute a global minimizer” and one could, “in practice, [...] obtain a global minimizer, independently of the position of the initial curve” [20]. A few years later, these considerations led to the development of fully convex approaches based on labeling functions which will be described now.

### Labeling Functions

The usage of labeling functions, i.e. functions which take values in the closed interval  $[0, 1]$ , comprises no real regularization, but it is rather a consequence of turning (3.12) into a convex optimization problem, cf. [13]. The identification of the components making (3.12) either convex or non-convex is thereby a crucial step:

1. We need a **convex subset**  $S$ , because the set of signed distance functions is not convex. A natural choice is the set of all functions which take values in the interval  $[0, 1]$ :

$$S = \{u : \Omega \rightarrow [0, 1]\}, \quad (3.20)$$

where we postpone a discussion on the regularity of these functions for a moment.

2. We need a **convex binarization operator** and Bresson *et al.* propose to use

$$\mathbf{B}(\phi) = \phi \quad (3.21)$$

which causes all level sets to evolve with equal velocity [13].

3. We need a **reprojection operator** and a suitable choice is

$$\mathbf{P}[\phi](x) = \min(\max(\phi(x), 0), 1), \quad x \in \Omega. \quad (3.22)$$

At first sight, these choices might appear unmotivated, but they become clear by inspecting (3.16) again. A key observation is that we will always obtain the same steady state solution, if we only assume that  $\mathbf{B}'$  is strictly positive such that all level sets of  $\phi$  are evolving. As there is no obvious reason why some level sets should evolve faster or slower than others we can use the same velocity for all of them. This leads almost inevitably to the binarization operator  $\mathbf{B}(\phi) = \phi$ , because it is convex and  $\mathbf{B}'(\phi) = 1$ . However, this specific choice of  $B$  causes  $U(\phi)$  to be homogeneous of degree one [13], and thus we have to prevent  $\phi$  from blowing up during the evolution by enforcing that it takes only values in a bounded interval. Together with the demand for a convex set  $S$  as well as the requirement that  $\mathbf{B}(\phi)$  should only take values in  $[0, 1]$  we end up with the above made choice of  $S$  and  $\mathbf{P}$ . However, we want to make the following remarks:

- The surface integral (3.11) in the convexified case becomes the so-called *weighted total variation*

$$\int_{\Omega} \mathbf{B}'(\phi) |\nabla\phi| g \, dx = \int_{\Omega} |\nabla\phi| g \, dx \quad (3.23)$$

acting as an explicit regularizer. This observation gives rise to the question why we did not choose  $F = BV(\Omega)$  in (3.12). However, the space of functions of bounded variation  $BV(\Omega)$  is not a Hilbert space and in order to discuss the choice of the metric for the computation of the gradient we need a Hilbert space framework, but there are, of course, other optimization methods which do not require a Hilbert space framework, e.g. splitting techniques for the weighted total variation [13].

- Finally, the binarization operator  $\mathbf{B}(\phi) = \phi$  deserves some attention. First of all  $B$  is not a binarization operator anymore, because the binarization is implicitly included in the choice of  $S$ . This leads to the question, if it would be possible to use a set of non-bounded functions, e.g.  $S = L^2(\Omega)$ , and a binarization operator taking values in  $[0, 1]$  instead? In fact, this is not possible, because a convex function with positive derivative cannot be bounded, cf. Fig. 3.3. However, there is still the possibility of choosing other (degenerate) binarization operators, which is maybe an interesting direction for further research.

We want to emphasize that it depends highly on the application whether a convex or a non-convex formulation should be used. In fact, we will demonstrate in chapter 4 that non-convex approaches can be very useful, especially for medical purposes.

### Parametrizations and Shape Models

Another implicit regularization strategy can be seen in the usage of parametrizations leading to finite dimensional function spaces spanned by smooth basis functions. A typical example are radial basis functions which have been used by Ho *et al.* [48], Morse *et al.* [72], Slabaugh *et al.* [105], and Benoit *et al.* [73] for instance. Approaches using splines, such as the MetaMorphs framework

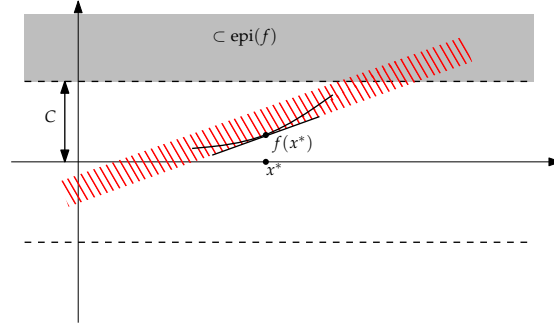


Figure 3.3: **On the Convexity of Bounded Binarization Operators:** Let  $f : \mathbb{R} \rightarrow \mathbb{R}$  be continuously differentiable and convex. If  $f'(x) > 0$  for all  $x \in \mathbb{R}$ ,  $f$  cannot be bounded. Proof: If  $f$  would be bounded, i.e.  $\exists C > 0 : |f(x)| \leq C \forall x \in \mathbb{R}$ , the half space  $\{(x, \lambda) \in \mathbb{R}^2 : \lambda > C\}$  would be a subset of the epigraph of  $f$ . Due to the convexity of  $f$ , however, the epigraph of  $f$  has to lie above all tangents of  $f$ , which is clearly a contradiction.

of Huang *et al.* [51], the variational B-spline framework of Bernard *et al.* [8], or the spherical harmonics shape model proposed by Baust and Navab [4] are also related to this strategy. Further, it is also possible to generate application specific basis functions, i.e. shape models, as proposed by Leventon *et al.* [61] or Tsai *et al.* [118] for instance. Of course, there are many more possibilities for learning such function spaces, but we restrict ourselves to the mentioned examples and refer the interested reader to the excellent overview of Heimann and Meinzer [46].

In most cases, the used binarization operator is either  $H_{2,\epsilon}$  or  $H_{\infty,\epsilon}$ . If  $\phi$  is not a signed distance function, it may happen in the case of  $H_{2,\epsilon}$  that the width of the narrow band  $N_\epsilon$  (cf. Fig. 3.2b) depends not only on  $\epsilon$ , but also on the slope of  $\phi$ , but this is in general not very problematic.

In contrast to the binarization operator, the re-projection operator does usually not appear explicitly in the approaches discussed above. It is rather implicitly contained in the gradient descent which can be explained as follows. Assume that the representation of the embedding function  $\phi$  with respect to  $S$  is given by

$$\phi = \sum_{i=1}^n \alpha_i \psi_i, \quad (3.24)$$

where  $\psi_1, \dots, \psi_n$  form a ( $L^2$ -orthonormal) basis of  $S$  and  $\alpha_1, \dots, \alpha_n \in \mathbb{R}$  denote the corresponding coefficients. A gradient descent for the parameter vector  $\alpha = (\alpha_1, \dots, \alpha_n)^T \in \mathbb{R}^n$  is then given by

$$\alpha_i^{t+\tau} = \alpha_i^t - \tau \langle \nabla_{L^2} E(\phi^t), \psi_i \rangle_{L^2}. \quad (3.25)$$

Now, we can turn (3.25) easily into a gradient descent for  $\phi$ :

$$\phi^{t+\tau} = \sum_{i=1}^n \alpha_i^{t+\tau} \psi_i \quad (3.26)$$

$$= \sum_{i=1}^n (\alpha_i^t - \tau \langle \nabla_{L^2} E(\phi^t), \psi_i \rangle_{L^2}) \psi_i \quad (3.27)$$

$$= \sum_{i=1}^n \alpha_i^t \psi_i - \tau \sum_{i=1}^n \langle \nabla_{L^2} E(\phi^t), \psi_i \rangle_{L^2} \psi_i \quad (3.28)$$

$$= \phi^t - \tau \sum_{i=1}^n \langle \nabla_{L^2} E(\phi^t), \psi_i \rangle_{L^2} \psi_i \quad (3.29)$$

$$= \phi^t - \tau \mathbf{P} [\nabla_{L^2} E(\phi^t)], \quad (3.30)$$

where the re-projection operator is given by

$$P[\phi] = \sum_{i=1}^n \langle \phi, \psi_i \rangle_{L^2} \psi_i. \quad (3.31)$$

This also confirms the above made assertion that only the gradient has to be projected, if  $S$  has a vector space structure.

### Infinite Dimensional and Smooth Function Spaces

Function spaces related to a parametrizations and shape models are usually finite dimensional. In contrast to this, Charpiat *et al.* [21] as well as Sundaramoorthi *et al.* [110] suggested the usage of infinite dimensional function spaces, such as  $C^\infty$  or the Sobolev space  $H^1$ . Two years later,  $C^\infty$  was also used by Bar and Sapiro in [3], but based on a slightly different mathematical justification. As these spaces also have a vector space structure the gradient descent corresponding to these regularizations also reads

$$\phi^{t+\tau} = \phi^t - \tau \mathbf{P} [\nabla_{L^2} E(\phi^t)] \quad (3.32)$$

and we will show an interesting connection between these implicit regularization strategies and first-order Tikhonov-type regularizers in Sec. 3.1.4. It deserves credit, that regularization strategies of this kind have been used much earlier in the registration community (e.g. Trouvé in 1998 [116]) than in the segmentation community. Moreover, it should be noted that [21] and [110] introduced these regularization strategies in a more geometric way and not for the variational level set method, but we will see in Sec. 3.1.4 that they also work in the non-geometric case. Finally, we wish to conclude this section on implicit regularization strategies with the overview presented in Tab. 3.1.

<b>approach</b>	classical variational level set method, e.g. [130, 79, 80]	Chan and Vese [20]	convexified, e.g. [13]	parametrized, e.g. [48, 72, 105, 73, 51, 8, 4, 61, 118]	$H^1$ , cf. Sec. 3.1.4	$C^\infty$ , cf. Sec. 3.1.4
$F$	$L^2(\Omega)$	$L^2(\Omega)$	$L^2(\Omega)^*$	$L^2(\Omega)$	$H^1(\Omega)$	$L^2(\Omega)$
$S$	signed distance functions	signed distance functions	$\{u : \Omega \rightarrow [0, 1]\} \cap BV(\Omega) \cap L^2(\Omega)^*$	$\{\phi = \sum_{i=1}^n \alpha_i \psi_i\}$	$H^1(\Omega)$	$C^\infty$
<b>B</b>	$H_{2,\epsilon}$	$H_{\infty,\epsilon}$	$\phi \mapsto \phi$	$H_{2,\epsilon}$ or $H_{\infty,\epsilon}$	$H_{2,\epsilon}$	$H_{2,\epsilon}$
<b>P</b>	re-initialization	re-initialization	$\min(\max(\phi(x), 0), 1)$	$\sum_{i=1}^n \langle \cdot, \psi_i \rangle_{L^2} \psi_i$	$(I - \Delta)^{-1}$	$G_\sigma * \cdot$

\*The original choice is  $S = F = BV(\Omega)$ , but we chose  $F$  and  $S$  in this particular way, because we need a Hilbert space framework here.

Table 3.1: Variational Level Set Approaches with Implicit Regularization.

### 3.1.3 Explicit Regularization

Although we shall later focus on Tikhonov-type regularizers, cf. Sec. 3.1.4, we briefly discuss several other explicit regularization strategies now.

#### Coefficient Regularizers

An explicit regularizer which does not directly depend on the embedding function, but on a vector of coefficients, e.g. in the case of a finite dimensional implicit regularization by a set of basis functions, is called *coefficient regularizer*. There are two main applications for such regularizers. A natural scenario is the incorporation of *shape distributions* into the segmentation framework. Using a plain shape model, i.e. an implicit regularization based on a set of trained basis functions, one implicitly assumes a uniform distribution. If this assumption is not justified, one might want to model other distributions of shape, e.g. a Gaussian distribution, cf. [28]. Another important application scenario could be to enforce *sparsity* with respect to a certain basis, cf. [101]. Our focus is, however, not on coefficient regularizers and we thus mention them only for the sake of completeness and refer the interested reader to [28] and [101].

#### Signed Distance Regularizers

In [63] Li *et al.* established a novel class of explicit regularizers which enforce locally the shape of a signed distance function. A well-known property of any signed distance function is  $|\nabla\phi(x)| = 1$  and a natural choice for such a regularizer is thus given by

$$R(\phi) = \int_{\Omega} (|\nabla\phi|^2 - 1)^2 dx \quad (3.33)$$

which penalizes the deviation of  $\phi$  from this property. The  $L^2$  gradient of this regularizer is

$$\nabla_{L^2} R(\phi) = -\operatorname{div} \left( \left( 1 - \frac{1}{|\nabla\phi|} \right) \nabla\phi \right). \quad (3.34)$$

Unfortunately, the diffusivity  $1 - 1/|\nabla\phi|$  is non-linear and enforces a backward diffusion, if  $|\nabla\phi| < 1$ , which has to be taken into account for the numerical treatment. For this reason an improved version of this regularizer, which has slightly better numerical properties, has recently been presented in [64].

It is important to mention that Gomes and Faugerás also introduced a kind of signed distance regularization, but unlike Li *et al.* [63] they directly regularize the evolution equation and not the energy.

#### Total Variation

Similar to the first order Tikhonov regularizer the total variation regularizer

$$R(\phi) = \int_{\Omega} |\nabla\phi| dx, \quad (3.35)$$

comprises a penalty on the gradient magnitude, but it also has a geometrical interpretation for characteristic functions as explained in Sec. 1.2. As a

consequence, the (weighted) total variation, cf. (3.23), appears quite naturally when using labeling functions which can be considered as relaxed characteristic functions. However, energies regularized with the total variation should not be optimized via gradient descent, because its  $L^2$  gradient

$$\nabla_{L^2} R(\phi) = -\operatorname{div} \left( \frac{\nabla \phi}{|\nabla \phi|} \right) \quad (3.36)$$

is non-linear in  $\phi$  and the diffusivity  $1/|\nabla \phi|$  is not defined, if  $|\nabla \phi| = 0$ , which has to be considered for the numerical treatment. In fact, there are faster techniques, such as the ones presented in [19, 13], which do not employ the  $L^2$ -gradient.

### Tikhonov-type Regularization

A classical type of regularization are first-order Tikhonov-type regularizers. In Sec. 3.1.4 we will, however, consider the more general form

$$R(\phi) = \int_{\Omega} (\nabla \phi)^T g \nabla \phi \, dx, \quad (3.37)$$

where the weight function  $g$  solely depends on the image function  $I$  (and not on  $\phi$ ) causing the resulting  $L^2$  gradient

$$\nabla_{L^2} R(\phi) = -\operatorname{div} (g \nabla \phi) \quad (3.38)$$

to be linear with respect to  $\phi$ . We will show in Sec. 3.1.4 that such regularizers can lead to update equations of the form

$$\phi^{t+\tau} = \mathbf{P} [\phi^t - \tau \nabla_{L^2} E(\phi^t)], \quad (3.39)$$

where the re-projection operator is same as in the case of an implicit  $H^1$  or  $C^\infty$  regularization.

### 3.1.4 Numerical Schemes for Tikhonov-type Regularizations

The goal of this subsection is to consider the following highly non-geometric and non-convex variational level set scenario:

- $F = L^2(\Omega)$ ,
- $S = F$ ,
- $R(\phi) = \int_{\Omega} (\nabla \phi)^T g \nabla \phi \, dx$ ,
- $B = H_{2,\epsilon}$ , and
- $P = Id$ .

As already mentioned before, we will show that the resulting update equations can be related to the implicit regularization strategies proposed in [21, 110, 3], but before that we have to discuss some theoretical implications first.

### Theoretical Considerations

A necessary theoretical assumption is the ellipticity condition

$$g \geq c, \quad (3.40)$$

for some  $c > 0$ . Provided (3.40) holds, the resulting continuous gradient descent

$$\partial_t \phi = -\nabla_{L^2} E(\phi) + \lambda \operatorname{div}(g \nabla \phi) \quad (3.41)$$

is a parabolic partial differential equation modeling a diffusion process. A parabolic equation has the nice property that information is spread with infinite speed and we can hope that this results in an improved convergence rate. However, it might be a good idea, to limit the amount of information, which is spread across edges. Thus, we will investigate not only the isotropic case  $g \equiv 1$ , but also

$$g(x) = \frac{1}{1 + |\nabla I(x)|^2 / \beta}, \quad \beta > 0, \quad (3.42)$$

which is clearly anisotropic.

Due to the usage of the compactly supported binarization operator  $H_{2,\epsilon}$  we obtain a splitting of  $\Omega$  into two domains with different behavior:

- A *competitive domain*, i.e. the narrow band  $N_\epsilon$  in (3.18), corresponding to  $\delta_\epsilon(\phi) \neq 0$  and indicated by gray color in Fig. 3.4a and 3.4b, where the evolution is governed by the competition between  $\operatorname{div}(g \nabla \phi)$  and  $\nabla_{L^2} E(\phi)$ . As a result, the slope of  $\phi$  in this area can be controlled by adjusting the regularization parameter  $\lambda$ , cf. Fig. 3.4d.
- A *diffusion dominated domain*, i.e.  $\Omega \setminus N_\epsilon$ , corresponding to  $\delta_\epsilon(\phi) = 0$  and indicated by gray stripes in Fig. 3.4a and 3.4b, where the evolution is completely governed by  $\operatorname{div}(g \nabla \phi)$ . Imposing Neumann boundary conditions we will observe that in the diffusion dominated domain

$$|\phi| \rightarrow \epsilon \quad (3.43)$$

as  $t \rightarrow \infty$ .

### Forward Euler Discretization

A forward Euler time discretization of (3.41) results in

$$\phi^{t+\tau} = \phi^t - \tau \nabla_{L^2} E(\phi^t) + \tau \lambda \operatorname{div}(g \nabla \phi^t). \quad (3.44)$$

Provided powerful alternatives are available, which is the case here, one should not use a forward Euler scheme, because, even in the simplest case  $g(I) \equiv 1$ , it suffers from the severe CFL-condition  $\tau \leq 1/(2^d \lambda)$ , where  $d$  denotes the number of spatial dimensions. Thus, we now derive more efficient numerical schemes for solving (3.41).

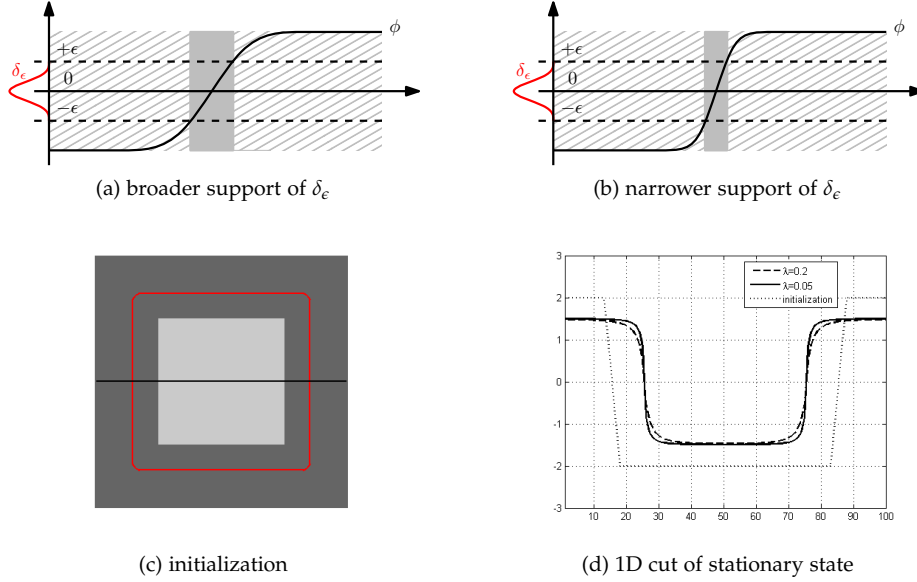


Figure 3.4: **Width of the Narrow Band:** The width of the narrow band  $N_\epsilon$  (gray) clearly depends of the slope of  $\phi$ . The steeper  $\phi$  the smaller the width of  $N_\epsilon$  and vice versa, cf. (a) and (b). The slope of  $\phi$  again depends on the choice of  $\lambda$ , because it controls the trade-off between data fidelity and regularization in the competitive domain (gray area in (a) and (b)). The higher the value of  $\lambda$  the smaller the slope of  $\phi$  and vice versa as demonstrated experimentally in (c) and (d) (we set  $g \equiv 1$ ). The black line in (c) indicates the position of the one dimensional cut shown in (d) and the red curve indicates the initial position of the zero level set. As predicted,  $\phi \rightarrow \pm\epsilon$  in the diffusion dominated domain (gray stripes in (a) and (b)) as verified in (d).

### Semi-Implicit Discretization

In order to avoid severe time step constraints we can use the semi-implicit scheme

$$\phi^{t+\tau} = \phi^t - \tau \nabla_{L^2} E(\phi^t) + \tau \lambda \operatorname{div} (g \nabla \phi^{t+\tau}), \quad (3.45)$$

leading to the update equation

$$\phi^{t+\tau} = (I - \tau \lambda \operatorname{div} (g \nabla))^{-1} (\phi^t - \tau \nabla_{L^2} E(\phi^t)). \quad (3.46)$$

Fortunately, the resulting equation system has to be assembled only once and we can use efficient numerical techniques for the inversion, which can be found in [123] or the book of Saad [98] for instance.

### Duhamel's Principle

If  $g \equiv 1$ , there is another possibility for solving (3.41) based on Duhamel's principle [35, chapter 2]. The main idea is to split an initial value problem of

the form

$$\begin{cases} \partial_t u(x, t) = f(x, t) + \lambda \Delta u(x, t), \\ u(x, 0) = g(x), \end{cases} \quad (3.47)$$

into two problems. One with the correct initial condition, but without source-term

$$(i) \begin{cases} \partial_t u_i(x, t) = \lambda \Delta u_i(x, t), \\ u_i(x, 0) = g(x), \end{cases} \quad (3.48)$$

and one including the source term, but with homogeneous initial condition

$$(s) \begin{cases} \partial_t u_s(x, t) = \lambda \Delta u_s(x, t) + f(x, t), \\ u_s(x, 0) = 0. \end{cases} \quad (3.49)$$

The superposition  $u = u_i + u_s$  eventually solves the whole problem, because

$$\partial_t u(x, t) = [\partial_t u_i + \partial_t u_s](x, t) = [\lambda \Delta u_i + \lambda \Delta u_s + f](x, t) = f(x, t) + \lambda \Delta u(x, t) \quad (3.50)$$

and

$$u(x, 0) = u_i(x, 0) + u_s(x, 0) = g(x) + 0 = g(x). \quad (3.51)$$

Denoting the fundamental solution by

$$\Phi(x, t) = \begin{cases} (4\pi\lambda t)^{-\frac{d}{2}} \exp\left(-\frac{\|x\|_2^2}{4\lambda t}\right), & t > 0, \\ 0, & t \leq 0, \end{cases} \quad (3.52)$$

where  $d$  denotes the spatial dimension, the solution to (i) can be written as

$$u_i(x, t) = (\Phi * g)(x, t), \quad (3.53)$$

if  $t > 0$ . The solution to (s) can be obtained using Duhamel's principle:

$$u_s(x, t) = \int_0^t \int_{\mathbb{R}^n} \Phi(x - y, t - s) f(y, s) dy ds. \quad (3.54)$$

Approximating the integral with respect to  $s$  we obtain

$$u_s(x, t) \approx t \int_{\mathbb{R}^n} \Phi(x - y, t - 0) f(y, 0) dy = t(\Phi * f(\cdot, 0))(x, t), \quad (3.55)$$

if  $t > 0$ . Thus we can construct an iterative scheme for (3.41) as follows. At time  $t$  we set  $\phi^t(x) = g(x)$  as well as  $-\nabla_{L^2} E(\phi^t(x)) = f(x, 0)$  and compute  $\phi^{t+\tau}$  via

$$\phi^{t+\tau} = G_{2\sqrt{\tau\lambda}} * \phi^t - \tau G_{2\sqrt{\tau\lambda}} * \nabla_{L^2} E(\phi^t) \quad (3.56)$$

$$= G_{2\sqrt{\tau\lambda}} * (\phi^t - \tau \nabla_{L^2} E(\phi^t)), \quad (3.57)$$

where

$$G_{2\sqrt{\tau\lambda}}(x) = \Phi(x, 2\sqrt{\tau\lambda}) \quad (3.58)$$

is nothing else than a Gaussian kernel with standard deviation  $2\sqrt{\tau\lambda}$ .

### Regularization Paradigms

We want to compare the schemes obtained by the semi-implicit time discretization and by Duhamel's principle to the numerical schemes which correspond to the implicit regularization strategies proposed in [21, 110, 3]. In order to simplify the following considerations, we define three *projection operators*, which can be considered as low-pass filters or smoothing operators:

1. The *Gaussian projector*

$$\mathbf{P}_G(\sigma)[\psi] = G_\sigma * \psi, \quad (3.59)$$

where  $G_\sigma$  is a Gaussian kernel with standard deviation  $\sigma$ ,

2. the *isotropic Sobolev projector*

$$\mathbf{P}_S(\alpha)[\psi] = (I - \alpha\Delta)^{-1} \psi, \quad (3.60)$$

where  $\alpha > 0$ , and

3. the *anisotropic Sobolev projector*

$$\mathbf{P}_A(\alpha)[\psi] = (I - \alpha \operatorname{div}(g\nabla))^{-1} \psi, \quad (3.61)$$

where again  $\alpha > 0$ .

This allows to rewrite the derived schemes as follows:

$$\phi^{t+\tau} = \begin{cases} \mathbf{P}_G(2\sqrt{\tau\sigma}) [\phi^t - \tau\nabla_{L^2}E(\phi^t)], & \text{Duhamel's principle for } g \equiv 1, \\ \mathbf{P}_S(\tau\lambda) [\phi^t - \tau\nabla_{L^2}E(\phi^t)], & \text{semi-implicit scheme for } g \equiv 1, \\ \mathbf{P}_A(\tau\lambda) [\phi^t - \tau\nabla_{L^2}E(\phi^t)], & \text{semi-implicit scheme for general } g. \end{cases} \quad (3.62)$$

If we forget about the model we want to solve and consider these schemes as plain update equations, we might wonder, whether it would be possible to regularize only the update  $\nabla_{L^2}E(\phi^t)$ . Indeed, it is and this leads us to the implicit regularization strategies suggested by Charpiat *et al.* [21] and Sundaramoorthi *et al.* [110]:

1. Choosing  $S = C^\infty$  in (3.12), cf. [21, 3], leads to a gradient descent of the form

$$\phi^{t+\tau} = \phi^t - \tau\mathbf{P}_G(\sigma) [\nabla_{L^2}E(\phi^t)]. \quad (3.63)$$

2. Choosing  $S = H^1$  in (3.12), cf. [110, 21], leads to a gradient descent of the form

$$\phi^{t+\tau} = \phi^t - \tau\mathbf{P}_S(\alpha) [\nabla_{L^2}E(\phi^t)]. \quad (3.64)$$

3. Finally, the gradient descent

$$\phi^{t+\tau} = \phi^t - \tau\mathbf{P}_A(\alpha) [\nabla_{L^2}E(\phi^t)], \quad (3.65)$$

corresponds to the choice  $S = H^1$  as well, but in this case  $H^1$  is endowed with the inner product

$$\langle \phi, \psi \rangle_{L^2} + \alpha \langle \nabla\phi, g\nabla\psi \rangle_{L^2}. \quad (3.66)$$

Interestingly, this regularization has not been used for variational level set segmentation so far.

applied to	$\nabla_{L^2}E(\phi^t)$	$\phi^t - \tau\nabla_{L^2}E(\phi^t)$
$\mathbf{P}_G(\sigma)$	[21] and [3]	isotropic diffusion ( $\sigma = 2\sqrt{\lambda\tau}$ )
$\mathbf{P}_S(\alpha)$	[21] and [110]	isotropic diffusion ( $\alpha = \lambda\tau$ )
$\mathbf{P}_A(\alpha)$	weighted Sobolev space	anisotropic diffusion ( $\alpha = \lambda\tau$ )

Table 3.2: Regularization Paradigms and Update Equations.

In summary, we can observe two regularization paradigms here. We can apply the projectors  $\mathbf{P}_G$ ,  $\mathbf{P}_S$ , and  $\mathbf{P}_A$  either to the whole right-hand side  $\phi^t - \tau\nabla_{L^2}E(\phi^t)$  (rhs), or only to the update given by  $\nabla_{L^2}E(\phi^t)$ , cf. Tab. 3.2. The computational complexity is exactly the same in both cases and it depends only on the used projector and the way we want to implement it (operator splitting, convolution, etc.).

At this point we wish to draw a connection to the principle of *cooperativity* which is an algorithmic concept discussed in [11]. Let us imagine that the result of applying one of the projectors defined above is computed by a network of individual processing cells which are connected to just a few neighbors. Then the process of computing the solution for all points is a so-called *cooperative process*, i.e. "a computation performed in parallel by a network of independent processing cells" [11], which have to exchange information with each other in order to compute the solution. The neighborhood relationships of all cells are thus modeled by the off-diagonal entries of the matrices discretizing the projectors  $\mathbf{P}_S$  and  $\mathbf{P}_A$  or by the entries of the filter mask discretizing  $\mathbf{P}_G$ <sup>2</sup>. Loosely speaking, we could say that regularization in the sense of enforcing a continuous or even smooth, and thus unambiguous solution, cf. Sec. 1.2, can only be achieved by tying together all involved processing cells.

In order to compare the two regularization paradigms derived above, we segmented three images from [2] (see Fig. 3.5) based on a standard Chan-Vese model [20]. In order to keep the application of the regularization operators corresponding to the implicit strategies of [21, 110, 3] comparable we used  $\sigma = 2\sqrt{\tau\lambda} = 2$  for  $\mathbf{P}_G$  and  $\alpha = \tau\lambda = 1$  for  $\mathbf{P}_S$  and  $\mathbf{P}_A$ . As expected, the application of a regularization operator to the whole right-hand side, which corresponds to an explicit Tikhonov-type regularization, results in an increased convergence rate (c.f. Fig. 3.5c, 3.5f, and 3.5i) and a smoother embedding function in all three cases. Comparing the three projectors with each other, it turns out that the results provided by  $\mathbf{P}_S(\alpha)$  and  $\mathbf{P}_A(\alpha)$  are visually more satisfying.

<sup>2</sup>The discretized Gaussian kernel has, of course, only a compact support which resembles the connections between the processing cells only up to a certain distance.

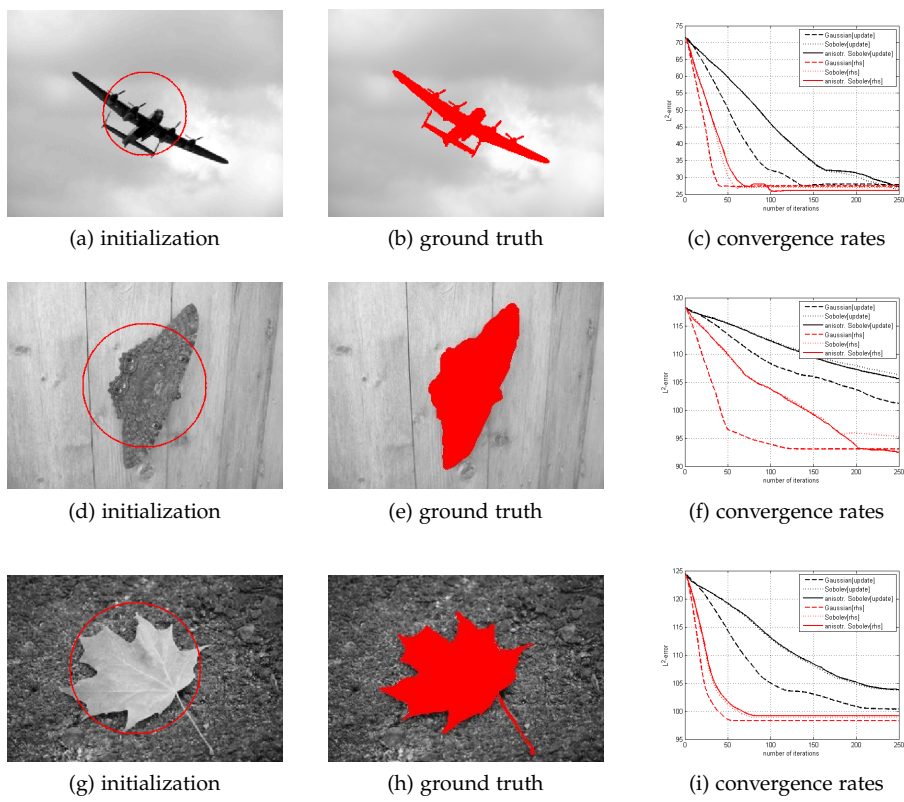


Figure 3.5: **Convergence Rates of Different Regularization Paradigms:** The explicit Tikhonov-type regularization paradigm shows an increased convergence rate.

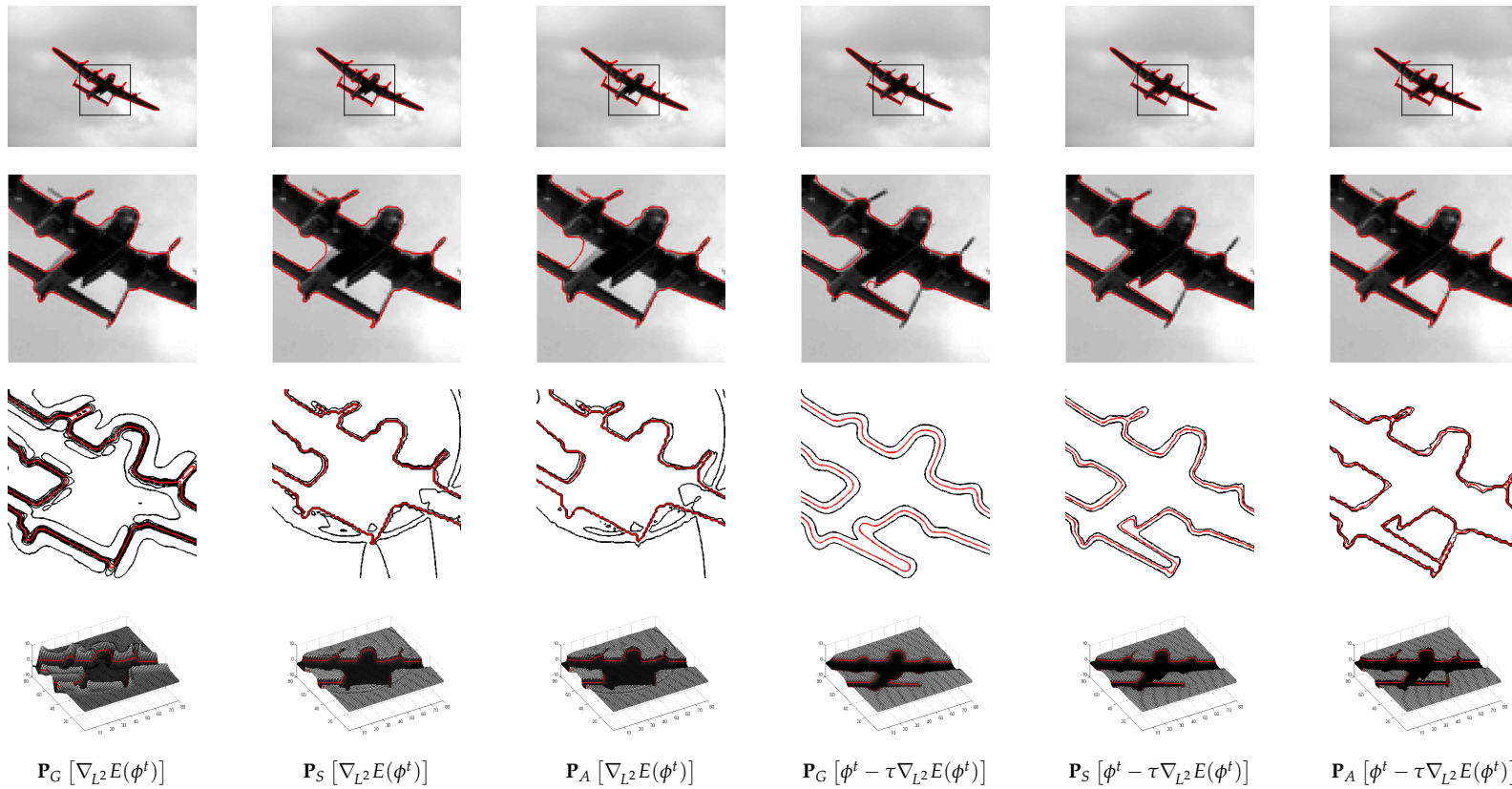


Figure 3.6: **Qualitative Comparison of Different Regularization Paradigms:** Segmentation results (first row), close-ups of the results (second row), the corresponding contour plots (third row), and the corresponding surface plots (bottom row).

## 3.2 The Almost Geometric Case

The  $H^1$ -type implicit regularization considered in the last section was totally non-geometric due to the following three reasons:

1. The embedding function was not a signed distance function making the width of the narrow band depending on the slope of the embedding function.
2. Regularizing the embedding function is different from regularizing the evolving curve.
3. The variational level set method itself is non-geometric in the sense that the evolution equation is derived with respect to the embedding function and not the curve itself.

The goal of this section is now, to derive an *almost geometric* variational level set method with an implicit  $H^1$ -regularization in the sense that we try to solve the first two issues while tolerating the third. The first issue can be solved easily by using signed distance functions again, but the solution of the second problem is a bit more involved. The reason is that we will have to deal with function spaces defined on the evolving surface  $\mathcal{S}$  itself (and not the embedding space). As a consequence, the projection of the computed gradient requires the solution of an elliptic partial differential equation on the implicitly defined surface  $\mathcal{S}$ . Interestingly, the computation of Sobolev gradients for *contours* can be achieved in linear complexity [110], but the computation for *surfaces* cannot due to the elliptic character of the problem. Although it has been demonstrated by [21] and [34] that Sobolev type surface evolutions are computationally feasible, the presented approach is slightly different:

1. In contrast to related approaches for surface evolutions [21, 34], we will employ a geometrically motivated Sobolev-type inner product, which allows the user to weight the translational and the deformational component of the computed gradient. This inner product is closely related to the ones that have been proposed for active contours by [110, 107].
2. All previous approaches for Sobolev-type curve and surface evolutions use either no implicit surface representation at all, or an implicit surface representation only for projecting the gradient [34, 21, 110]. In contrast to this, we use an implicit representation *on purpose* yielding a unified framework for Sobolev-type curve *and* surface evolutions.
3. In order to solve the projection step in a computationally efficient manner, we propose to turn the resulting elliptic PDE into a parabolic one, which corresponds to a continuous gradient descent. Inspired by [96] we further split the elliptic operator in such a way that a standard semi-implicit time discretization can be used. If desired, one can even use operator splitting techniques, e.g. [123], in order to obtain an approximative Sobolev gradient in *linear complexity*.

Before we explain the theory of Sobolev spaces on implicit surfaces in Sec. 3.2.2 and 3.2.3, we briefly review the classical  $L^2$  framework for variational level set methods in Sec. 3.2.1 in order to better explain the differences of the presented approach. In Sec. 3.2.4 we derive the proposed numerical scheme and verify the expected properties experimentally.

### 3.2.1 The Classical $L^2$ Framework

As the following considerations are based on a signed distance representation of the evolving curve or surface  $\mathcal{S} \subset \Omega \subset \mathbb{R}^d$  ( $d = 2, 3$ ) we will use the well-known property  $|\nabla\phi| = 1$  in order to simplify the notation whenever appropriate.

Again we assume that our segmentation problem is modeled as a minimization problem of the form

$$\min_{\phi} E(\phi). \quad (3.67)$$

In order to make the following derivations more illustrative, we further assume that  $E$  is of the form

$$E(\phi) = \frac{1}{|\mathcal{S}|} \int_{\Omega} H_{2,\epsilon}(-\phi) f \, dx + \frac{\gamma}{|\mathcal{S}|} \int_{\Omega} \delta_{2,\epsilon}(\phi) g |\nabla\phi| \, dx. \quad (3.68)$$

Note that this energy is made scale-invariant by normalizing it with the surface area  $|\mathcal{S}|$ . Computing the first variation  $F(E, \psi)$  of  $E$  yields

$$F(E, \psi) = \left. \frac{d}{dt} E(\phi + t\psi) \right|_{t=0} = -\frac{1}{|\mathcal{S}|} \int_{\Omega} \delta_{2,\epsilon}(\phi) [f + \alpha \operatorname{div}(g \nabla\phi)] \psi \, dx = 0, \quad (3.69)$$

where we replaced  $\nabla\phi / |\nabla\phi|$  by  $\nabla\phi$  due to the above mentioned property of signed distance functions. It has been noted in [22] that computing the first variation with respect to the embedding function, as done in (3.69), is different to computing the first variation of  $E$  with respect to the surface itself. The technique presented in [22] for converting level set gradients to shape gradients is, however, only available in two dimensions. If a similar technique becomes available for three dimensions, it would also make the proposed framework more geometric, but until then we rely on computing the first variation with respect to  $\phi$ .

As a compromise, we will define the  $L^2$  gradient of  $E$  as

$$\nabla_{L^2} E = -(f + \alpha \operatorname{div}(g \nabla\phi)). \quad (3.70)$$

and the  $L^2$  inner product as

$$\langle u, v \rangle_{L^2} = \frac{1}{|\mathcal{S}|} \int_{\Omega} \delta_{2,\epsilon}(\phi) uv \, dx, \quad (3.71)$$

which is slightly different to the usual convention of defining  $\langle u, v \rangle_{L^2} = \int_{\Omega} uv \, dx$  and  $\nabla_{L^2} E = -\delta_{2,\epsilon}(\phi) [f + \alpha \operatorname{div}(g \nabla\phi)]$ . This way, the inner product defined in (3.71) can be interpreted as an approximation to the  $L^2$  inner product for functions defined on  $\mathcal{S}$  rather than functions defined on  $\Omega$ . Thus,

$\nabla_{L^2}E$  as it is defined in (3.70) shall be interpreted as a function defined on  $\mathcal{S}$ . This interpretation would, of course, give rise to the question of how  $\nabla_{L^2}E$  has to be extended to the support of  $\delta_{2,\epsilon}$ , but since the definition of  $\nabla_{L^2}E$  makes sense for all points in  $\Omega$  this extension is naturally given. Finally, the continuous gradient descent is now of the form

$$\partial_t \phi = -\delta_{2,\epsilon}(\phi) \nabla_{L^2}E \quad (3.72)$$

and this notation clearly reveals that the evolution is localized to a small vicinity of  $\mathcal{S}$  as it would be in the case of a Lagrangian implementation.

### 3.2.2 Sobolev Spaces on Implicit Surfaces

We will now discuss two possible surface Sobolev spaces.

#### The Classical Sobolev Space $H^1$

In [21, 34] a Sobolev space of the following type has been used for obtaining more regular gradients:

$$H^1(\mathcal{S}) = \left\{ u \in L^2(\mathcal{S}) : \|u\|_{H^1} < \infty \right\}, \quad (3.73)$$

where  $\|u\|_{H^1}^2 = \langle u, u \rangle_{H^1}$  and

$$\langle u, v \rangle_{H^1} = \lambda \langle u, v \rangle_{L^2} + \frac{1}{|\mathcal{S}|} \int_{\Omega} \delta_{\epsilon}(\phi) \nabla_{\mathcal{S}} u \cdot \nabla_{\mathcal{S}} v \, dx, \quad \lambda > 0. \quad (3.74)$$

Noting that the unit outward normal is given by  $\eta = \nabla \phi$  we can write the intrinsic surface gradient as

$$\nabla_{\mathcal{S}} u = (I - \eta \otimes \eta) \nabla u, \quad (3.75)$$

which is a projection of  $\nabla u$  onto  $\mathcal{S}$ , cf. [9]. In contrast to [21, 34] we decided to weight the zero order component of  $\langle \cdot, \cdot \rangle_{H^1}$  by  $\lambda$  (and not the first order component), because we want to avoid an unnecessary coupling of the model parameter  $\lambda$  and the step size parameter  $\tau$  in Sec. 3.2.4.

#### The Geometrically Motivated Sobolev Space $\hat{H}^1$

The reason why we propose to use a different Sobolev space is that the zero order component  $\langle u, v \rangle_{L^2}$  of  $H^1$  has no geometric interpretation. Inspired by [110] we propose the following Sobolev space

$$\hat{H}^1(\mathcal{S}) = \left\{ u \in L^2(\mathcal{S}) : \|u\|_{\hat{H}^1} < \infty \right\}, \quad (3.76)$$

where  $\|u\|_{\hat{H}^1}^2 = \langle u, u \rangle_{\hat{H}^1}$ ,

$$\langle u, v \rangle_{\hat{H}^1} = \lambda \bar{u} \cdot \bar{v} + \frac{1}{|\mathcal{S}|} \int_{\Omega} \delta_{2,\epsilon}(\phi) \nabla_{\mathcal{S}} u \cdot \nabla_{\mathcal{S}} v \, dx, \quad \lambda > 0, \quad (3.77)$$

and

$$\bar{u} = \frac{1}{|\mathcal{S}|} \int_{\Omega} \delta_{2,\epsilon}(\phi) u \eta \, dx. \quad (3.78)$$

The benefit of this Sobolev space is that the zero order component of the inner product has a geometric interpretation, because  $\bar{u}$  is the portion of  $u$  which corresponds to a translation of the zero level set, cf. also [110]. This geometric meaning can also be observed experimentally in Sec. 3.2.4.

### 3.2.3 Computing Sobolev Gradients

Fortunately, Sobolev gradients can be computed easily from the standard  $L^2$  gradient by employing the Riesz representation theorem [35]. We define  $u = \nabla_{H^1} E$ ,  $\hat{u} = \nabla_{\hat{H}^1} E$ , and  $w = \nabla_{L^2} E$  as well as

$$\int_{\Omega} \cdot \, dx = \frac{1}{|\mathcal{S}|} \int_{\Omega} \delta_{2,\epsilon}(\phi) \cdot \, dx \quad (3.79)$$

in order to simplify the notation in the following computations.

#### Computing $\nabla_{H^1} E$

Applying the representation theorem we obtain:

$$\langle w, v \rangle_{L^2} = \int_{\Omega} w v \, dx = \int_{\Omega} [\lambda u v + \nabla_{\mathcal{S}} u \cdot \nabla_{\mathcal{S}} v] \, dx = \langle u, v \rangle_{H^1}, \quad (3.80)$$

where  $v$  is chosen arbitrarily. Noting that  $\mathcal{S}$  is a closed surface and applying integration by parts we obtain

$$\int_{\Omega} w v \, dx = \int_{\Omega} [\lambda u - \Delta_{\mathcal{S}} u] v \, dx, \quad (3.81)$$

where

$$\Delta_{\mathcal{S}} u = \operatorname{div}((I - \eta \otimes \eta) \nabla u) \quad (3.82)$$

is the intrinsic surface Laplacian, i.e. the Laplace-Beltrami operator, cf. [9]. Applying the fundamental lemma of calculus of variations we obtain

$$w = (\lambda I - \Delta_{\mathcal{S}}) u. \quad (3.83)$$

In order to solve this surface PDE we impose homogeneous Dirichlet boundary conditions  $u|_{\Gamma_{\epsilon}} = 0$ , where  $\Gamma_{\epsilon} = \partial N_{\epsilon}$  denotes the boundary of the narrow band  $N_{\epsilon}$ , cf. (3.18).

#### Computing $\nabla_{\hat{H}^1} E$

Again, we apply the representation theorem:

$$\langle w, v \rangle_{L^2} = \int_{\Omega} w v \, dx = \lambda \bar{u} \cdot \bar{v} + \int_{\Omega} \nabla_{\mathcal{S}} u \cdot \nabla_{\mathcal{S}} v \, dx = \langle u, v \rangle_{\hat{H}^1}. \quad (3.84)$$

Inserting the definition of  $\bar{v}$  yields

$$\int_{\Omega} w v \, dx = \int_{\Omega} [\lambda \bar{u} \cdot (v \eta) + \nabla_{\mathcal{S}} u \cdot \nabla_{\mathcal{S}} v] \, dx. \quad (3.85)$$

Integrating by parts and using the fundamental lemma we end up with

$$w = \lambda \bar{u} \cdot \eta - \Delta_S u. \quad (3.86)$$

As  $\bar{w} = \bar{u}$ , we finally have

$$w - \lambda \bar{w} \cdot \eta = -\Delta_S u, \quad (3.87)$$

where we impose homogeneous Dirichlet boundary conditions on  $\Gamma_\epsilon$  again.

### 3.2.4 Numerical Treatment

Once we have computed  $\nabla_{H^1} E$  or  $\nabla_{\hat{H}^1} E$  numerically, we can use it to evolve the embedding function by

$$\partial_t \phi = -\delta_{2,\epsilon}(\phi) \nabla_{H^1} E, \quad \text{or} \quad \partial_t \phi = -\delta_{2,\epsilon}(\phi) \nabla_{\hat{H}^1} E, \quad (3.88)$$

respectively, where we use  $\epsilon = 1.5$ , as suggested in [80]. We approximate the time derivative with a standard forward Euler discretization and interleave this evolution with a few iteration steps for reinitializing the signed distance function, where we use the method of Peng *et al.* [85] in our experiments. A more geometric way of maintaining a signed distance representation would, of course, be given by the method of Chen *et al.* [22], which is unfortunately only available for two dimensional problems.

The only question remaining is how to compute  $\nabla_{H^1} E = u$  or  $\nabla_{\hat{H}^1} = \hat{u}$  numerically, if  $\nabla_{L^2} E = w$  is given. Our strategy will be to turn the stationary PDEs (3.83) and (3.87) into time dependent ones and split the elliptic operators in such a way that a standard semi-implicit time discretization for parabolic problems can be used. A stability analysis of similar splitting techniques can be found in [96].

#### Computing $\nabla_{H^1} E$ Numerically

At first we note that (3.83) may be interpreted as the gradient of the energy

$$\frac{1}{2} \int_{N_\epsilon} |\nabla_S u|^2 + \lambda u^2 - 2uw \, dx. \quad (3.89)$$

A continuous gradient descent for this energy yields the parabolic problem

$$\partial_t u = \Delta_S u - \lambda u + w. \quad (3.90)$$

Next we split  $\Delta_S$  which yields:

$$\partial_t u = \Delta u - \operatorname{div}(\eta \otimes \eta \nabla u) - \lambda u + w. \quad (3.91)$$

Finally, we employ a semi-implicit time discretization leading to

$$(I - \tau \Delta) u^{t+\tau} = u^t - \tau [\operatorname{div}(\eta \otimes \eta \nabla u^t) + \lambda u^t - w]. \quad (3.92)$$

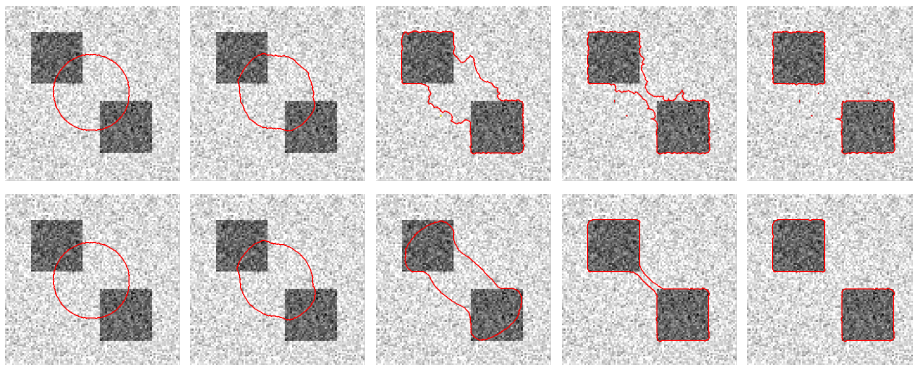


Figure 3.7: **Beneficial Properties of Sobolev Gradients:** In contrast to the curve evolution based on  $L^2$  gradient (upper row), the evolution based on  $\hat{H}^1$  gradients is much smoother, even in the case of topological changes.

### Computing $\nabla_{\hat{H}^1} E$ Numerically

Similar to the previous considerations, we note that (3.87) may be interpreted as the gradient of the energy

$$\frac{1}{2} \int_{N_\epsilon} |\nabla_S u|^2 - 2(w - \lambda \bar{w} \cdot \eta)u \, dx. \quad (3.93)$$

The corresponding continuous gradient descent then reads

$$\partial_t \hat{u} = \Delta_S \hat{u} + (w - \lambda \bar{w} \cdot \eta), \quad (3.94)$$

and after splitting  $\Delta_S$  we obtain

$$\partial_t \hat{u} = \Delta \hat{u} - \operatorname{div}(\eta \otimes \eta \nabla \hat{u}) + (w - \lambda \bar{w} \cdot \eta). \quad (3.95)$$

Finally, we employ again a semi-implicit time discretization:

$$(I - \tau \Delta) \hat{u}^{t+\tau} = \hat{u}^t - \tau [\operatorname{div}(\eta \otimes \eta \nabla \hat{u}^t) - (w - \lambda \bar{w} \cdot \eta)]. \quad (3.96)$$

### Remarks

The presented numerical schemes allow us to use comparatively large step sizes in order to compute the Sobolev gradients. In all our experiments five iteration steps with  $\tau = 2$  were sufficient in order to obtain a good approximation. Finally, we want to mention that weighting the first order component  $\int_{\Omega} \nabla_S u \cdot \nabla_S v \, dx$  by  $\lambda > 0$  would have led to operators of the form  $(I - \lambda \tau \Delta)$  and thus an unnecessary coupling of the discretization parameter  $\tau$  and the model parameter  $\lambda$ .

### Discussion of the Experiments

The main advantage of Sobolev gradients is that the corresponding curve and surface evolutions are much smoother than the ones based on classical  $L^2$

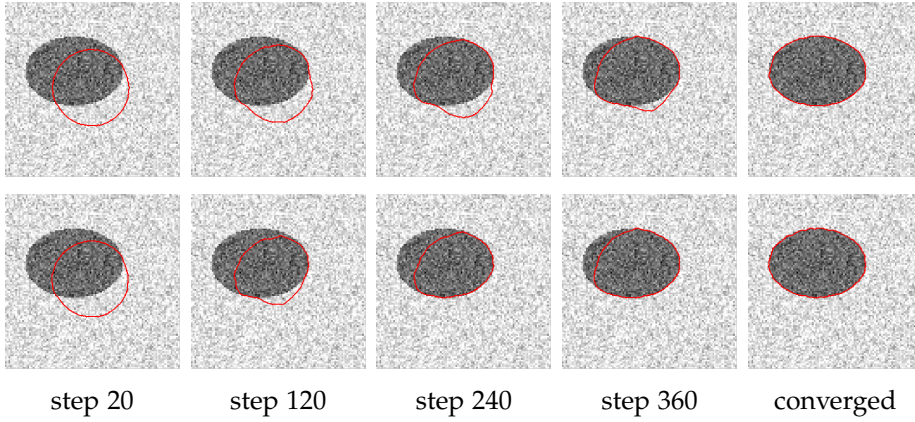


Figure 3.8: **Comparison of  $H^1$  and  $\hat{H}^1$** : The  $H^1$  driven curve (upper row) is less eager to capture the object by translation than the  $\hat{H}^1$  driven curve, which reaches the object much earlier (compare step 240 and 360).

gradients. In order to demonstrate that the Sobolev gradient obtained with the proposed numerical scheme have the same advantageous properties we compare the  $\hat{H}^1$  evolution to a classical  $L^2$  evolution in Fig. 3.7 by minimizing the standard Chan-Vese model without penalizing the curve length [20]. As expected, the  $\hat{H}^1$  evolution is much smoother than the one based on  $L^2$  gradients.

In Fig. 3.8 we illustrate the difference between the  $H^1$  evolution and the  $\hat{H}^1$  evolution by minimizing the same energy. In both cases we chose  $\lambda = 0.5$  and used the same step size for the curve evolution. We can see that the curve evolved by the  $\hat{H}^1$  gradient (lower row) moves much earlier to the object than the curve evolved by the  $H^1$  gradient, which is only able to capture the object by deformation.

Our last experiment in Fig. 3.9 shows the applicability of our framework to real world problems. We track the left ventricular cavity acquired by 3D+t MRI [91] by taking the segmentation result from one volume as the initialization for the following one. Again we use the Chan-Vese model without length penalty and apart from that we employ no regularizer which ensures that the subsequent segmentation result is somehow close to the previous one.

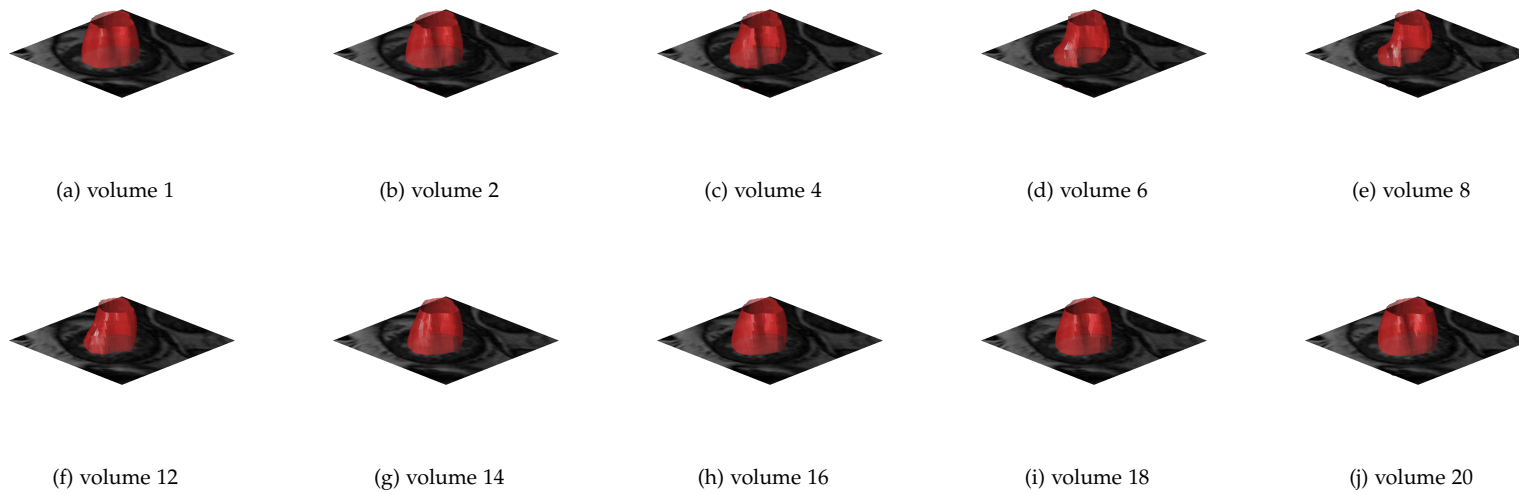


Figure 3.9: **Tracking Example:** Tracking of the left ventricular cavity acquired by 3D+t MRI (data set taken from [91]).

# 4

## Polar Active Contours

### 4.1 Introduction

Polar curve or surface representations have proven to be a useful shape model for numerous medical segmentation tasks. Popular application scenarios are for instance the segmentation of the left ventricular cavity from sequential ultrasound (US) data or magnetic resonance imaging (MRI) [104, 39, 37, 38, 31, 65], the slice-wise segmentation of aortic aneurysms from US or computed tomography angiography (CTA) data [92, 12, 4], the segmentation of kidneys in sequential US data [36], and the segmentation and tracking of individual cells [93, 50]. Additionally, polar descriptions have been proposed for tracking humans or objects [30, 24] and for interactive image segmentation [120].

In almost all of the above cited approaches the polar representation is used in an active contour framework. This means that starting from an initial contour one aims at finding the desired object boundary by iteratively minimizing an energy, which characterizes the optimal position of the contour. However, there are two main issues, which have to be considered.

Firstly, the global optimum may not correspond to the desired segmentation, cf. Fig. 4.1, and a polar representation can be considered as a *geometric implicit regularization*, which may help to obtain the desired local minimum.

Secondly, even a polar representation might not provide enough regularity to prevent the curve evolution from getting stuck in an undesired local minimum. Thus one often augments the energy with an additional explicit regularizer, e.g. the curve length [93], or restricts the solution space to a finite set of smooth basis functions, e.g. spherical harmonics [4], in order to obtain satisfying segmentation results. As a consequence, one is either forced to minimize a *different energy* or restricted to a *finite dimensional representation*, which may not always be desired.

Recently, Sundaramoorthi *et al.* [110] as well as Charpiat *et al.* [21] proposed to employ smooth but infinite dimensional function spaces, i.e. Sobolev spaces. The advantage of this regularization strategy is that one can directly minimize the desired energy while not being restricted to a finite dimensional function

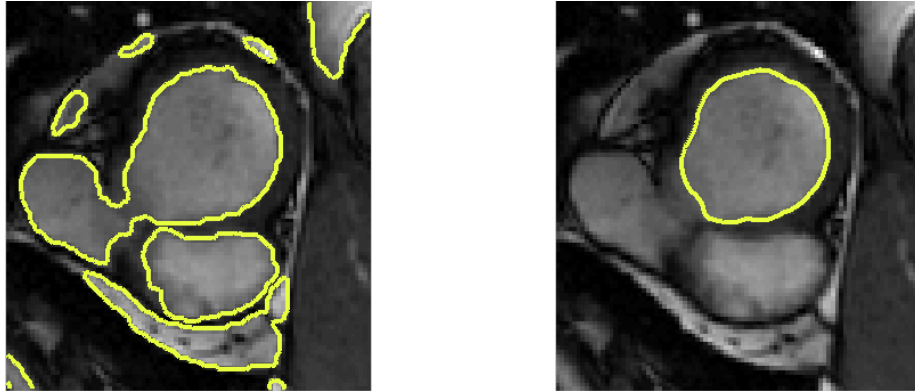


Figure 4.1: **Global versus Local:** Sometimes a global minimum (left) is not useful for medical applications. If a polar object description can be used, as in the case of the left ventricle, it introduces a meaningful geometric regularization (right). Note that a restriction to convex objects cannot be applied here. (The image is taken from [91] and the result in (a) is computed with [13].)

space. Another advantage of curve evolutions in Sobolev spaces is that they are far less sensitive to local minima [108]. Moreover, it is possible to endow these function spaces with metrics that allow the user to weight rigid and non-rigid deformation components [21].

In this chapter we develop a Sobolev-type function space for *polar active contours*, which is endowed with a metric that allows the user to favor translations and scale changes over smooth deformations. We achieve this goal by two steps in Sec. 4.2:

1. We define a suitable structure for such a function space, in the following called *polar space*, by analyzing how the standard recipe for variational active contours changes when we restrict ourselves to a polar curve representation. This will lead to a basic polar space, where only translations can be favored.
2. We extend this basic polar space, in such a way that it contains smoother functions. Additionally, the metric in this space will allow us to weight not only translations, but also scale changes.

After giving some details on the implementation in Sec. 4.3, we compare our method to existing approaches and demonstrate its applicability to a variety of medical examples in Sec. 4.4.

## 4.2 Polar Spaces

We consider curves which can be represented by polar coordinates, i.e. an origin  $c^o \in \mathbb{R}^2$  and a radius function  $c^r : [0, 2\pi] \rightarrow (0, \infty)$ :

$$c = c^o + c^r \mathbf{s}, \quad (4.1)$$

where  $\mathbf{s} = (\cos(\theta), \sin(\theta))^T$  and  $\theta \in [0, 2\pi]$ . This definition already implies a certain parametrization of  $c$  and although this parametrization seems to be natural for polar curves we want to switch to an arc length parametrization. Denoting the derivative of  $c$  with respect to  $\theta$  by  $c'$ , the arc length  $s$  is defined as

$$s(\theta) = \int_0^\theta |c'| \, dp \quad (4.2)$$

and thus the length of  $c$  is  $L = s(2\pi)$ . In order to avoid the curve length  $L$  to be confused with the symbol for the function space  $L^2$ , we will denote the space of square integrable functions by  $\mathbb{L}^2$  and the Sobolev space by  $\mathbb{H}^1$  in the remainder of this chapter.

Our goal is now to derive function spaces, which we will term *polar spaces*, that reflect and also exploit the possibility of decomposing any polar curve into a *finite dimensional component*  $c^o$  and an *infinite dimensional component*  $c^r$ .

### 4.2.1 Variational Active Contours

Before we start to derive the concept of polar spaces, we briefly revisit the standard recipe for variational active contour methods and recall where the choice of the function space comes into play. The standard recipe reads:

1. Define an energy  $E$ , which gets (at least locally) minimized by the desired configuration of the curve. Thereby, we focus on *geometric energies*, which are defined with respect to the arc length of  $c$ .
2. Consider a time-varying *family of geometric curves*  $c(s, t)$  such that the first variation  $F(E, c)$  of  $E$  vanishes:

$$F(E, c) = \left. \frac{d}{dt} E(c(s, t)) \right|_{t=0} = \int_0^L \nabla E \cdot c_t \, ds = 0, \quad (4.3)$$

where  $c_t$  denotes the partial derivative of  $c(s, t)$  with respect to  $t$ .

3. Evolve the curve under the gradient flow (continuous gradient descent)

$$c_t = -\nabla E(c), \quad (4.4)$$

since plugging (4.4) into (4.3) yields

$$F(E, c) = - \int_0^L (\nabla E(c))^2 \, ds < 0. \quad (4.5)$$

It has been pointed out by Michor and Mumford [71] as well as Yezzi and Menucci [129] that (4.3) contains the implicit assumption of using an  $\mathbb{L}^2(0, L)$  framework, since

$$\int_0^L \nabla E \cdot c_t \, ds = \langle \nabla E, c_t \rangle_{\mathbb{L}^2}. \quad (4.6)$$

Thus, the generalized form of (4.3) reads

$$F(E, c) = \left. \frac{d}{dt} E(c(s, t)) \right|_{t=0} = \langle \nabla_{\mathbb{F}} E, c_t \rangle_{\mathbb{F}} = 0, \quad (4.7)$$

where  $\mathbb{F}$  can be any Hilbert space accompanied by the inner product  $\langle \cdot, \cdot \rangle_{\mathbb{F}}$ . As indicated in (4.7), the gradient of  $E$  depends on the choice of the Hilbert space or more precisely on the metric induced by its inner product. By choosing function spaces beyond  $\mathbb{L}^2$  and constructing intelligent metrics in these spaces one can obtain gradient flows

$$c_t = -\nabla_{\mathbb{F}} E(c) \quad (4.8)$$

with favorable properties for segmentation and tracking, cf. [110, 21, 108].

The choice of a suitable function space for polar curves, called *polar space* in the following, is the main goal of this section. As a first step, we will study (4.7), if  $c$  has the form (4.1).

## 4.2.2 The Polar Space $\mathcal{L}$

In order to identify the structure of a polar space, we assume that  $c$  has a polar representation, cf. (4.1), and that  $\mathbb{F} = \mathbb{L}^2$  is equipped with the *scale invariant* inner product

$$\langle h, k \rangle_{\mathbb{L}^2} = \frac{1}{L} \int_0^L h(s) \cdot k(s) \, ds, \quad (4.9)$$

where  $h, k : [0, L] \rightarrow \mathbb{R}^2$ . Then, the first variation (4.7) reads:

$$F(E, c) = \langle \nabla_{\mathbb{L}^2} E, c_t^o \rangle_{\mathbb{L}^2} + \langle \nabla_{\mathbb{L}^2} E, c_t^r \mathbf{s} \rangle_{\mathbb{L}^2} \quad (4.10)$$

$$= \overline{\nabla_{\mathbb{L}^2} E} \cdot c_t^o + \frac{1}{L} \int_0^L (\nabla_{\mathbb{L}^2} E \cdot \mathbf{s}) c_t^r \, ds, \quad (4.11)$$

where  $\overline{\cdot}$  denotes the mean value, which is defined as

$$\bar{h} = \frac{1}{L} \int_0^L h \, ds. \quad (4.12)$$

As a consequence, we obtain the evolution equations

$$c_t^o = -\overline{\nabla_{\mathbb{L}^2} E(c)} \quad \text{and} \quad c_t^r = -\nabla_{\mathbb{L}^2} E(c) \cdot \mathbf{s}. \quad (4.13)$$

From a more formal point of view, we can interpret the tuple

$$\left( \overline{\nabla_{\mathbb{L}^2} E(c)}, \nabla_{\mathbb{L}^2} E(c) \cdot \mathbf{s} \right) \in \mathbb{R}^2 \times \mathbb{L}^2(0, L) \quad (4.14)$$

as the  $\mathbb{L}^2$  projection of  $\nabla_{\mathbb{L}^2} E$  onto the subspace of polar curves, which means that the evolution of any polar curve according to (4.13) always stays in this subspace. This interpretation motivates the following definition.

**Definition 4.1 (Polar Space  $\mathcal{L}$ )** We define the polar space  $\mathcal{L}$  as

$$\mathcal{L} = \mathbb{R}^2 \times \mathbb{L}^2(0, L). \quad (4.15)$$

This space becomes a Hilbert space with the inner product

$$\langle h, k \rangle_{\mathcal{L}} = h^o \cdot k^o + \frac{\lambda}{L} \int_0^L h^r k^r ds, \quad (4.16)$$

where  $h = (h^o, h^r), k = (k^o, k^r) \in \mathcal{L}$ , and  $\lambda > 0$ . Note that  $h^r, k^r : [0, L] \rightarrow \mathbb{R}$ .

The polar space  $\mathcal{L}$  enjoys two desirable features:

1. Origin components and radial components are orthogonal to each other.
2. The additional parameter  $\lambda$  allows us to weight the influence of the infinite dimensional component. Since the gradient of  $E$  with respect to  $\mathcal{L}$  reads

$$\nabla_{\mathcal{L}} E = (\overline{\nabla_{\mathbb{L}^2} E}, (\nabla_{\mathbb{L}^2} E \cdot \mathbf{s}) / \lambda), \quad (4.17)$$

$\nabla_{\mathcal{L}} E$  becomes a pure translation of the origin as  $\lambda \rightarrow \infty$ . This way, we can favor translations of the origin over deformations of the radius function.

Although the possibility of weighting translations over radial deformations is useful for image segmentation purposes,  $\mathcal{L}$  suffers from the fact that it is based on the function space  $\mathbb{L}^2$ , which contains nearly arbitrary functions. As a consequence, the curve evolution is very sensitive to noise because all parts of the curve can move independently from each other. This is demonstrated in Fig. 4.2 as well as in Sec. 4.4. In order to prevent the curve from getting stuck in an undesired local minimum, a penalty on the curve length is often added to the energy. This causes the curve evolution to be smoother, but results in the minimization of a different energy, which may not always be desired. Instead of regularizing the energy, one can choose smooth but infinite-dimensional function spaces, which allows the user to directly minimize the desired energy [110]. Inspired by these approaches, we want to find a polar space which contains smooth radial components. Moreover, we will go one step further and endow this polar space with a metric that allows the user to weight translations, scale changes and (smooth) deformations differently.

### 4.2.3 The Polar Space $\mathcal{H}$

Now, we want to design a polar space which contains smoother radial components than  $\mathcal{L}$  and whose inner product allows us to favor translations and scale changes over smooth deformations. We will see that the following polar space has all these advantageous properties.

**Definition 4.2 (Polar Space  $\mathcal{H}$ )** We define the Sobolev-type polar space

$$\mathcal{H} = \mathbb{R}^2 \times \mathbb{H}^1(0, L), \quad (4.18)$$

where

$$\mathbb{H}^1(0, L) = \{h^r \in \mathbb{L}^2(0, L) : \|h^r\|_{\mathbb{H}^1} < \infty\} \quad (4.19)$$

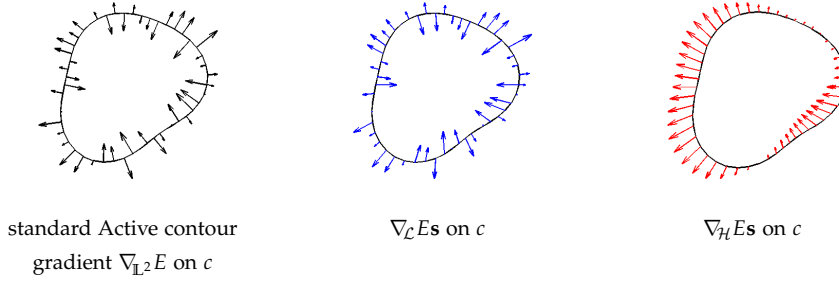


Figure 4.2: **Different Gradients:** A standard active contour gradient in normal direction is shown on the left. The projection of this gradient onto  $\mathbf{s}$  is drawn in the middle, while its smoothed version, i.e. the radial component of the  $\mathcal{H}$  gradient, is shown on the right. Note that this vector field generates a smoother and more global deformation of the curve.

and  $\|\cdot\|_{\mathbb{H}^1}$  is induced by the inner product

$$\langle h^r, k^r \rangle_{\mathbb{H}^1} = \overline{h^r} k^r + \gamma L \int_0^L h_s^r k_s^r ds. \quad (4.20)$$

$\mathcal{H}$  becomes a Hilbert space with the inner product

$$\langle h, k \rangle_{\mathcal{H}} = h^o \cdot k^o + \lambda \left( \overline{h^r} k^r + \gamma L \int_0^L h_s^r k_s^r ds \right), \quad (4.21)$$

where  $h = (h^o, h^r), k = (k^o, k^r) \in \mathcal{H}$ .

Note that the scale is exactly captured by the average value of the radial component  $\overline{h^r}$ . Before we discuss the properties of  $\mathcal{H}$  and  $\langle \cdot, \cdot \rangle_{\mathcal{H}}$  in detail, we will explain how  $\nabla_{\mathcal{H}}E$  can be computed from  $\nabla_{\mathcal{L}}E$ . Therefore, we suppose that  $\nabla_{\mathcal{L}}E = h = (h^o, h^r)^T$  and  $\nabla_{\mathcal{H}}E = k = (k^o, k^r)^T$ . Applying the Riesz representation theorem [60] we obtain  $\langle h, l \rangle_{\mathcal{L}} = \langle k, l \rangle_{\mathcal{H}}$ . Since origin and radial components are orthogonal, we have  $k^o = h^o$  and

$$\frac{\lambda}{L} \int_0^L h^r l^r ds = \lambda \left( \overline{k^r} \overline{l^r} + \gamma L \int_0^L k_s^r l_s^r ds \right). \quad (4.22)$$

Using the definition of  $\overline{l^r}$  and applying integration by parts as well as the fundamental lemma of variational calculus we obtain

$$h^r = \overline{k^r} - \gamma L^2 k_{ss}^r. \quad (4.23)$$

Since  $\overline{h^r} = \overline{k^r}$  we end up with the ordinary differential equation

$$k_{ss}^r = \frac{1}{\gamma L^2} \left( \overline{h^r} - h^r \right). \quad (4.24)$$

The the solution to (4.24) can be written as (cf. Sec. 4.3.4 and [110])

$$k^r = K_{\gamma} * h^r, \quad (4.25)$$

where

$$K_\gamma(s) = \frac{1}{L} \left( 1 + \frac{(s/L)^2 - (s/L) + 1/6}{2\gamma} \right) \quad (4.26)$$

and  $s \in [0, L]$ . In fact,  $K_\gamma$  can be interpreted as a smoothing kernel, which is also illustrated in Fig. 4.2. However,  $k^r$  can still be computed in linear complexity by

$$k^r(s) = k^r(0) + sk_s^r(0) - \frac{1}{\gamma L^2} \int_0^s (s - \hat{s})(k^r(\hat{s}) - \bar{k}^r) d\hat{s}, \quad (4.27)$$

where

$$k_s^r(0) = -\frac{1}{\gamma L^3} \int_0^L s(k^r(s) - \bar{k}^r) ds \quad (4.28)$$

and

$$k^r(0) = \int_0^L K_\gamma(s) h^r(s) ds, \quad (4.29)$$

as shown in [110] and appendix 4.3.4.

The polar space  $\mathcal{H}$  enjoys the following properties:

1. Origin and radial components are orthogonal with respect to  $\langle \cdot, \cdot \rangle_{\mathcal{H}}$ .
2. As  $\lambda \rightarrow \infty$  gradients computed with respect to  $\langle \cdot, \cdot \rangle_{\mathcal{H}}$  converge towards pure translations of the origin.
3. As  $\gamma \rightarrow \infty$  we can deduce from (4.26) that  $K_\gamma \rightarrow 1/L$  and thus the radial component of the  $\mathcal{H}$  gradient becomes a pure rescaling of the curve.

Adjusting  $\lambda$  and  $\gamma$  we can now favor translations of the origin over radial deformations as well as scale changes over smooth deformations. We will see in Sec. 4.4 that these properties are beneficial for a lot of applications. Before that, however, we discuss some implementation details.

### 4.3 Implementation

Since  $\nabla_{\mathbb{L}^2} E$  is necessary to compute the  $\mathcal{L}$  gradient as well as the  $\mathcal{H}$  gradient, we will explain how the computation of  $\nabla_{\mathbb{L}^2} E$  can be implemented, cf. Sec. 4.3.1. In Sec. 4.3.2 we will briefly comment on the choice of the parameters  $\lambda$  and  $\gamma$ . As our method employs no additional strategy for placing the origin we are also going to discuss several strategies used in other approaches in Sec. 4.3.3. Further, we shall explain in Sec. 4.3.4 how the convolution kernel in (4.26) can be derived. Finally, we derive a first order accurate implicit curve representation in Sec. 4.3.5.

#### 4.3.1 Computation of $\nabla_{\mathbb{L}^2} E$

In order to explain how  $\nabla_{\mathbb{L}^2} E$  is computed, we consider the following linear combination of a region-based and a boundary-based energy

$$E(c) = \int_{\text{int } c} f \, dx + \alpha \int_0^L g \, ds, \quad (4.30)$$

where  $\text{int } c$  denotes the region which is bounded by  $c$ . The  $\mathbb{L}^2$  gradient of  $E$ , assuming the scale invariant scalar product (4.9), reads

$$\nabla_{\mathbb{L}^2} E(c) = Lf\mathbf{n} + \alpha L(\nabla g \cdot \mathbf{n} - g\kappa)\mathbf{n}, \quad (4.31)$$

where  $\mathbf{n}$  denotes the normal of  $c$  and  $\kappa$  its curvature. Note that quantities like  $\mathbf{n}$  and  $\kappa$  can be computed from a polygon representation of  $c$ , but a more accurate way is to compute them from an implicit representation as suggested in [110]. Besides using a signed distance function it is also possible to use the embedding function

$$\phi(x) = \begin{cases} |x - c^o| - c^r(\theta(x)), & x \neq 0, \\ \inf_{x \neq 0} \phi(x), & x = 0, \end{cases} \quad (4.32)$$

for representing polar curves implicitly [4]. Of course, this function is not a signed distance function, but we only need a correct position of the zero level set. In practice, this requirement is usually satisfied, if the position of  $c$  is two or three pixels away from the singularity at  $x = 0$ .

If, however, a signed-distance representation is needed, in order to compute geometric quantities in the neighborhood of the zero level set for instance, we suggest to employ the first-order accurate correction

$$\hat{\phi}(x) = [\mathbf{s}(\theta(x)) \cdot \mathbf{n}(\theta(x))] \phi(x), \quad (4.33)$$

which is derived in Sec. 4.3.5.

#### 4.3.2 Choosing $\lambda$ and $\gamma$

Choosing  $\lambda$  and  $\gamma$  is quite easy because both parameters have a geometric interpretation. At first, we note that the range of the image intensities is not important in the following considerations, because it only affects the step size of the gradient descent scheme. Now,  $\lambda$  and  $\gamma$  should be chosen as follows:

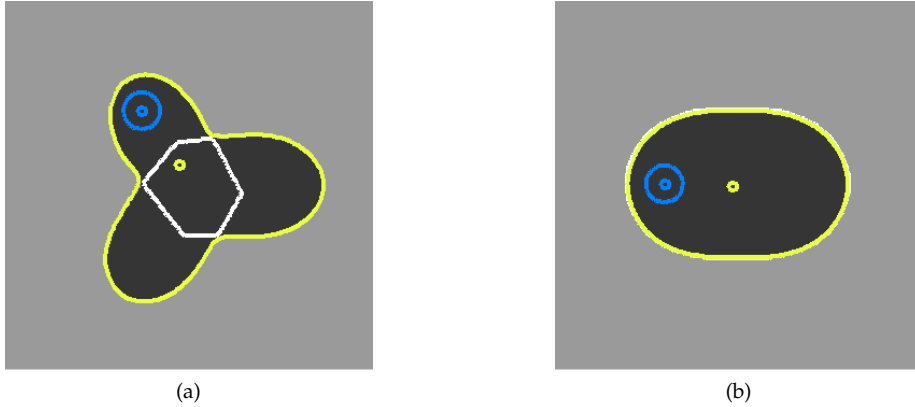


Figure 4.3: **Evolution of the Origin:** If the object is not convex (a), the origin converges to a position within the kernel (white). If the object is convex (b), the center stays in the kernel, which consists of the whole object. The initialization is drawn in blue.

- If origin translations are preferred, one should choose  $\lambda > 1$ , e.g.  $\lambda \in (1, 10]$ . If scale changes and radial deformations are preferred, one should choose  $\lambda < 1$ , e.g.  $\lambda \in [0.6, 0.9]$ .
- Meaningful values for  $\gamma$  turned out to be between 0.042 and 1, where higher values correspond to a stronger preference of scale changes. The lower bound for  $\gamma$  is  $1/24$  because it ensures that  $K_\gamma$  is positive [110].

In general, we recommend to start with  $\lambda = 1$  and  $\gamma = 0.042$  as this yields satisfying results in most cases.

### 4.3.3 Choosing the Origin

In our framework the evolution of the origin  $c^o$  is only governed by the evolution equation  $c_t^o = -\nabla_{\mathbb{L}^2} E$ . However, there are several approaches of choosing  $c^o$  explicitly or influencing its evolution. Thus, we want to quickly discuss their advantages and disadvantages:

1. **User-defined position:** In [120], for instance, a fixed origin is chosen by the user. This choice seems to be useful for interactive segmentation tasks, but if the object has, however, a more complicated boundary, it may require some time to select a good origin point.
2. **Center of mass:** It is also possible to choose the origin as the center of mass of the curve (cf. [30]). This choice works well for most applications, but from a purely theoretical point of view it is not always guaranteed that the center of mass lies within the object.
3. **Regularization:** In [4] a penalization of the  $\mathbb{L}^2$  norm of the radius function is suggested in order to force the origin to converge towards a

position near the center of mass. However, over-regularization may lead to more convex segmentations or even a shrinking-bias.

4. **Geometrically correct:** From a mathematical point of view it may seem tempting to choose a point within the set of points from which the whole boundary can be seen. This set is called the *kernel* of an object. The main drawback of this strategy is that the kernel is not very stable under small perturbations of the curve, as it is defined by the intersection of all half spaces generated by the tangent of the curve.

For certain applications it may be advantageous to use one of these strategies. However, our experience shows that such an additional step is not necessary, since  $c^o$  automatically converges to a position within the kernel, cf. Fig. 4.3.

### 4.3.4 Solving the ODE

The computation of the gradient  $\nabla_E \mathcal{H}$  requires the solution of the following ordinary differential equation, cf. also [110]:

$$g''(s) = \frac{1}{\lambda L^2}(f(s) - \bar{f}), \quad g(0) = g(L), \quad g'(0) = g'(L), \quad (4.34)$$

where we set  $g = k^r$  and  $f = h^r$  in order to keep the notation simple. Further, we denote the differentiation with respect to  $s$  by  $'$ . At first, we integrate twice and obtain:

$$g(s) = g(0) + sg'(0) + \frac{1}{\lambda L^2} \int_0^s \int_0^{\hat{s}} f(\xi) - \bar{f} \, d\xi \, d\hat{s}. \quad (4.35)$$

Second, we perform integration by parts for the rightmost term:

$$\int_0^s \int_0^{\hat{s}} f(\xi) - \bar{f} \, d\xi \, d\hat{s} = \quad (4.36)$$

$$\int_0^s \frac{d}{d\hat{s}} \left[ (\hat{s} - s) \int_0^{\hat{s}} f(\xi) - \bar{f} \, d\xi \right] - (\hat{s} - s)(f(\hat{s}) - \bar{f}) \, d\hat{s} = \quad (4.37)$$

$$(\hat{s} - s) \int_0^{\hat{s}} f(\xi) - \bar{f} \, d\xi \Big|_0^s + \int_0^s (s - \hat{s})(f(\hat{s}) - \bar{f}) \, d\hat{s} = \quad (4.38)$$

$$\int_0^s (s - \hat{s})(f(\hat{s}) - \bar{f}) \, d\hat{s}. \quad (4.39)$$

Thus, we end up with

$$g(s) = g(0) + sg'(0) + \frac{1}{\lambda L^2} \int_0^s (s - \hat{s})(f(\hat{s}) - \bar{f}) \, d\hat{s}. \quad (4.40)$$

Setting  $s = L$  and using the boundary condition  $g(0) = g(L)$  we obtain

$$g'(0) = \frac{1}{\lambda L^3} \int_0^L (L - \hat{s})(f(\hat{s}) - \bar{f}) \, d\hat{s} \quad (4.41)$$

$$= \frac{1}{\lambda L^3} \int_0^L L(f(\hat{s}) - \bar{f}) \, d\hat{s} - \frac{1}{\lambda L^3} \int_0^L \hat{s}(f(\hat{s}) - \bar{f}) \, d\hat{s} \quad (4.42)$$

$$= -\frac{1}{\lambda L^3} \int_0^L \hat{s}(f(\hat{s}) - \bar{f}) \, d\hat{s}, \quad (4.43)$$

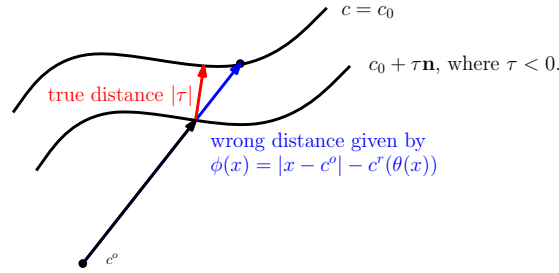


Figure 4.4: **True and Wrong Distance:** The wrong distance to the curve (or the zero level set, respectively) is given by  $\phi(x)$ . The true distance is given by  $|\tau|$ .

due to the definition of  $\bar{f}$ . Changing  $\hat{s}$  to  $s$  eventually yields

$$g'(0) = -\frac{1}{\lambda L^3} \int_0^L s(f(s) - \bar{f}) ds. \quad (4.44)$$

Plugging this formula into (4.40), integrating both sides from 0 to  $L$ , and using again that  $\bar{g} = \bar{f}$  we finally obtain

$$g(0) = \frac{1}{L} \int_0^L f(s) \left( 1 + \frac{(s/L)^2 - (s/L) + 1/6}{2\gamma} \right) ds = \int_0^L f(s) K_\gamma(s) ds, \quad (4.45)$$

where  $K_\gamma(s)$  is the kernel defined in (4.26). Since the definition of the arc length allows us to choose the starting point arbitrarily we can conclude from (4.45) that  $g$  may also be obtained by  $g = K_\gamma * f$ .

### 4.3.5 Deriving a First Order Correction for $\phi$

Now, we want to derive a first-order accurate correction  $\psi$  such that  $\hat{\phi}(x) = \psi(x)\phi(x)$ , where  $\phi$  defined in (4.32), is close to a signed distance representation of  $c$ , which we denote by  $\Phi(x)$ . At first, we note that the level lines of a signed distance representation of  $c$  are solutions to  $c_t = \mathbf{n}$ . Supposing that  $\epsilon \in \mathbb{R}$  is sufficiently small one might say that the level line  $L_\epsilon = \{x \in \Omega : \Phi(x) = \epsilon\}$  can be approximated by evolving  $c$  with a forward Euler discretization of the flow  $c_t = \mathbf{n}$ :

$$c^{0+\tau} = c^0 + \tau \mathbf{n}, \quad (4.46)$$

where  $c^0 = c$  and  $\tau = \epsilon$ . As we are only interested in the *geometry* of  $c$  we can add a tangential component to the flow  $c_t = \mathbf{n}$ :

$$c_t = \mathbf{n} + \frac{\mathbf{s} \cdot \mathbf{t}}{\mathbf{s} \cdot \mathbf{n}} \mathbf{t} = \frac{\mathbf{s} \cdot \mathbf{n}}{\mathbf{s} \cdot \mathbf{n}} \mathbf{n} + \frac{\mathbf{s} \cdot \mathbf{t}}{\mathbf{s} \cdot \mathbf{n}} \mathbf{t} = \frac{1}{\mathbf{s} \cdot \mathbf{n}} \mathbf{s}, \quad (4.47)$$

since  $\mathbf{t}$  and  $\mathbf{n}$  are an orthonormal basis. From this we may conclude that the flows  $c_t = \mathbf{n}$  and  $c_t = 1/(\mathbf{s} \cdot \mathbf{n})\mathbf{s}$  yield the same *geometric* curve. This means that the level line  $L_\epsilon$  can also be approximated by performing a forward Euler step of the flow  $c_t = 1/(\mathbf{s} \cdot \mathbf{n})\mathbf{s}$ :

$$c^{0+\tau} = c^0 + \frac{\tau}{\mathbf{s} \cdot \mathbf{n}} \mathbf{s}, \quad (4.48)$$

where again  $c^0 = c$  and  $\tau = \epsilon$ . As  $\phi(x)$  gives us the signed distance  $\epsilon / (\mathbf{s} \cdot \mathbf{n})$ , see Fig. 4.4, we thus know that the correction  $\psi$  is given by

$$\psi(x) = \mathbf{s}(\theta(x)) \cdot \mathbf{n}(\theta(x)). \quad (4.49)$$

Of course, this correction is only first-order accurate in  $\epsilon$ , because we derived it via forward Euler discretizations.

## 4.4 Experiments

In order to illustrate the advantages of the polar space  $\mathcal{H}$  we performed several experiments on synthetic as well as real data. Besides standard segmentation experiments (cf. Fig. 4.5 and Fig. 4.6) we performed also *visual tracking* experiments, where the segmentation of a whole image sequence is achieved by taking the result of the current frame as the initialization for the following frame (cf. Fig. 4.7 and Fig. 4.9).

### 4.4.1 Comparing Different Flows

In Fig. 4.5 we segment a noisy square by minimizing the Chan-Vese model [20]. We can observe that the  $\mathcal{L}$  flow is not stable and gets stuck in a local minimum due to the fact that all parts of the curve can move independently from each other, which is indicated by the spiky boundary. This is also true when we penalize the deformation component more. Increasing  $\lambda$  and employing a length regularization we can stabilize the  $\mathcal{L}$  flow. A similar result can be achieved by using the spherical harmonics (SPHARM) shape model, which we have proposed in an earlier work [4]. It is important to note that the regularized  $\mathcal{L}$  flow as well as the SPHARM model do not minimize the original energy. The first uses a length regularization and the latter employs a penalty on the norm of the radial component which causes a bias towards convex objects and may lead to a shrinking contour in the case of over-regularization. In contrast to this, the standard Sobolev active contour minimizes the original energy while showing its typical coarse to fine behavior [110, 108]. The same is, of course, true for the  $\mathcal{H}$  flow and we can see that the evolution of both flows is quite similar. The careful observer, however, might already see that the  $\mathcal{H}$  flow first translates the shape, then adapts the scale of the shape, and finally deforms it. Being typical for Sobolev-type flows [108], this behavior is extremely valuable for medical applications, where images often suffer from a relatively high amount of noise. Please note that this experiment also demonstrates that classical and polar Sobolev active contours are able to segment objects with corners, because we only ensure smoothness of the flow and not of the result itself. In fact, first order Sobolev spaces, such as the ones employed here, are the correct spaces for representing corners, because elements of them have a continuous representative, but not necessarily a continuous derivative, such as the function  $f(x) = |x|$  for instance [35].

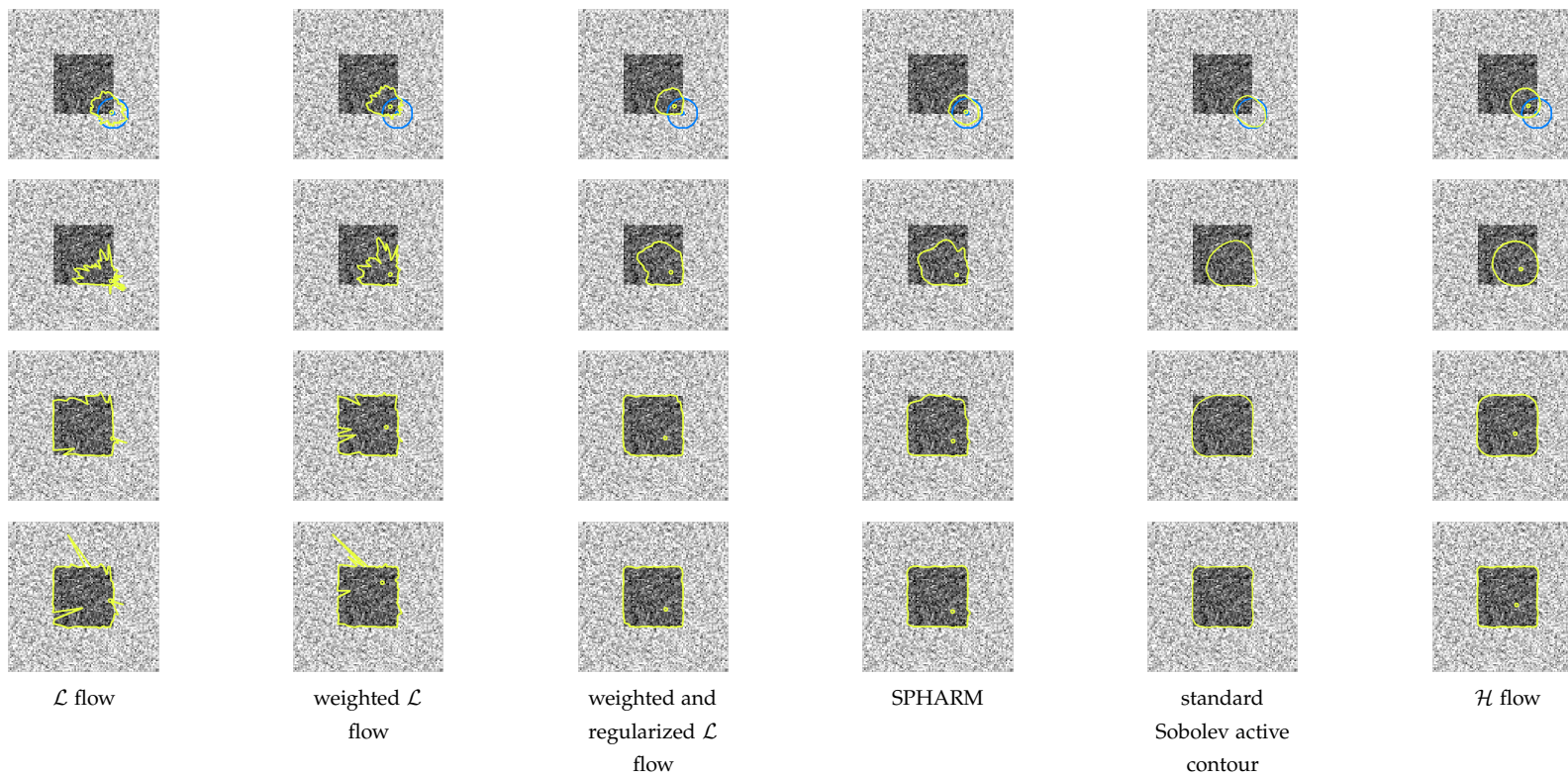


Figure 4.5: **Behavior of Different Flows:** The  $\mathcal{L}$  flow and the translation weighted  $\mathcal{L}$  flow (i.e.  $\lambda = 10$ ) get stuck in a local minimum because all parts of the curve can move independently from each other (the initialization is drawn in blue). The weighted and regularized  $\mathcal{L}$  flow and the SPHARM model [4] segment the lumen successfully, but still adapt to local features immediately. In contrast to this, the standard Sobolev active contours [110] as well as the  $\mathcal{H}$  flow capture the coarse shape first and adapt to local structures much later.

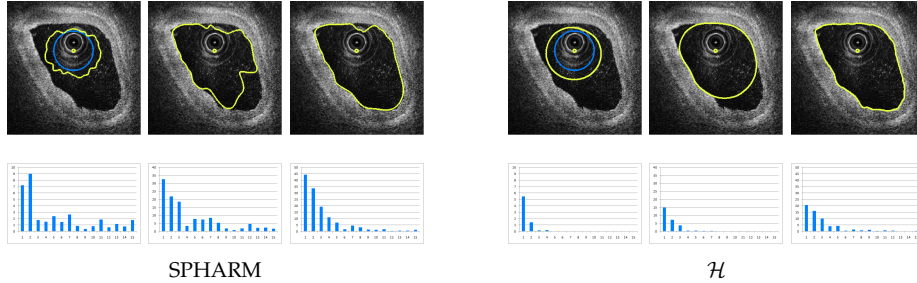


Figure 4.6: **Coarse-to-Fine Behavior:** During the evolution of the SPHARM model (left) all frequencies become active right at the beginning, which is shown by the amplitude plots of the first 15 frequencies in the second row (the initialization is drawn in blue). The resulting sensitivity to local minima causes the contour to get stuck in a local minimum. In contrast to this, the coarse-to-fine behavior of the  $\mathcal{H}$  flow makes the contour very robust to local minima. Note that the origin is fixed in this experiment in order to compare the frequencies.

#### 4.4.2 Coarse-to-Fine Behavior

In order to illustrate the *coarse-to-fine* nature of the  $\mathcal{H}$  flow a bit further we segment a coronary artery acquired by optical coherence tomography, cf. Fig. 4.6. Again we minimize the Chan-Vese model without length regularization. In order to compare the amplitudes of the first 15 frequencies of  $c^r$  we fixed the origin in this experiment. During the evolution of the SPHARM model, which is restricted to 20 frequencies, high frequencies appear to become active right at the beginning, which is not the case for the  $\mathcal{H}$  flow. The reason for this *coarse to fine* behavior of the  $\mathcal{H}$  flow is exactly the weighting of the frequency components discussed already in (1.34) in Sec. 1.2, which eventually leads to frequency dependent step sizes during the gradient descent. This makes the  $\mathcal{H}$  flow very robust to local minima, although  $\mathcal{H}$  contains an *infinite* number of frequency components.

#### 4.4.3 Comparison to Classical Sobolev Active Contours

While the coarse-to-fine behavior is typical for Sobolev-type flows in general, the  $\mathcal{H}$  flow is endowed with a metric that allows us to favor origin translations and scale changes over smooth deformations. These properties make the  $\mathcal{H}$  flow extremely suitable for visual tracking applications, where an image sequence is segmented in a frame-wise manner by using the segmentation of one frame as the initialization for the subsequent one. It is important to note that we employ no regularization which ensures that the contours of consecutive frames are close or similar.

In Fig. 4.7 we compare the  $\mathcal{H}$  flow to a standard Sobolev active contour [110], which allows only to weight translations as well as deformations *including* scale changes. In this experiment we segment an ellipse whose scale is increasing

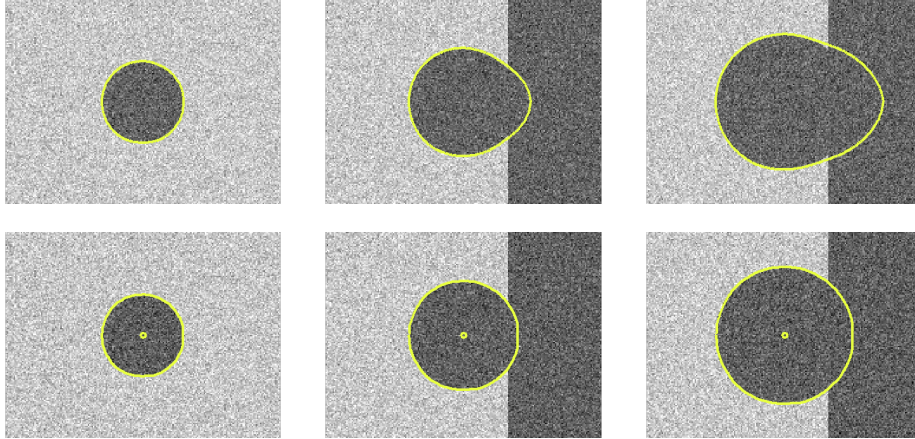


Figure 4.7: **Comparison to Sobolev Active Contours:** In this artificial tracking experiment, we can observe that the classical Sobolev Active contours (upper row) only allow to weight translations and deformations: if we allow for scale changes we also allow for deformations. In contrast to this, the  $\mathcal{H}$  flow (lower row) allows the user to penalize scale changes differently than deformations and it is thus able to maintain the shape.

such that it is occluded by the bar on the right hand side. We can see that, if we want the classical Sobolev active contour to be able to adapt to scale changes we also have to allow deformations, which causes the Sobolev active contour to leak. In contrast to this, the  $\mathcal{H}$  flow allows to weight scale changes and deformations *differently*. This leads to an increased robustness with respect to occlusions or background clutter.

#### 4.4.4 Visual Tracking Applications

In Fig. 4.9 we give several examples for visual tracking applications ranging from spatial and temporal aneurysm segmentation (first and second row) to left ventricle and cell tracking (third and fourth row).

In the first row of Fig. 4.9 we segment the inner wall (yellow) and the outer wall (blue) of an abdominal aortic aneurysm from CTA data by minimizing the coupled Chan-Vese model for aneurysm analysis proposed in [4]. The background in this scenario is highly cluttered due to the high intensities of the neighboring vertebrae, but the  $\mathcal{H}$  flow successfully tracks the aneurysm over 68 slices. The segmented aneurysm can be seen in Fig. 4.8. Please note that the inner and outer walls are smooth although we employed no regularization ensuring that segmentations in neighboring slices are somehow close or similar.

Combining the coupled Chan-Vese model of [4] with our framework can also be used for *temporal* aneurysm analysis. In the second row of Fig. 4.9 we segment an image sequence of one slice of an aortic aneurysm acquired with 4D MRI. The image quality in this example is rather poor and the neighboring vertebrae have almost the same image intensities as the thrombus, but the  $\mathcal{H}$

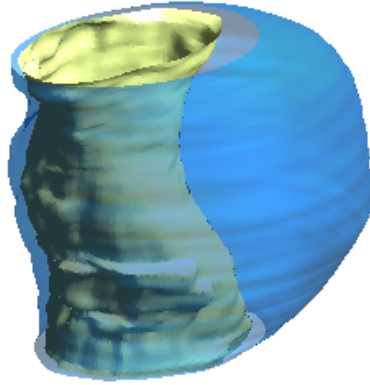


Figure 4.8: **Aneurysm Segmented by  $\mathcal{H}$  flow:** The inner wall is drawn in yellow and the outer wall is drawn in blue. Note that, although we employed no regularization ensuring that segmentations of neighboring slices are similar, both surfaces are continuous and smooth.

flow shows almost no leakage into surrounding objects.

In the third row of of Fig. 4.9 we track one slice of a left ventricular cavity acquired by 4D MRI. Although the image intensities are varying spatially and temporally the  $\mathcal{H}$  flow is able to segment the ventricular cavity by minimizing a standard piecewise constant model [20]. The image data was taken from [91].

In the forth row of Fig. 4.9 we finally track a Leukocyte chasing a bacterium in order to demonstrate the applicability of method to cell segmentation. The image sequence was taken from [99].

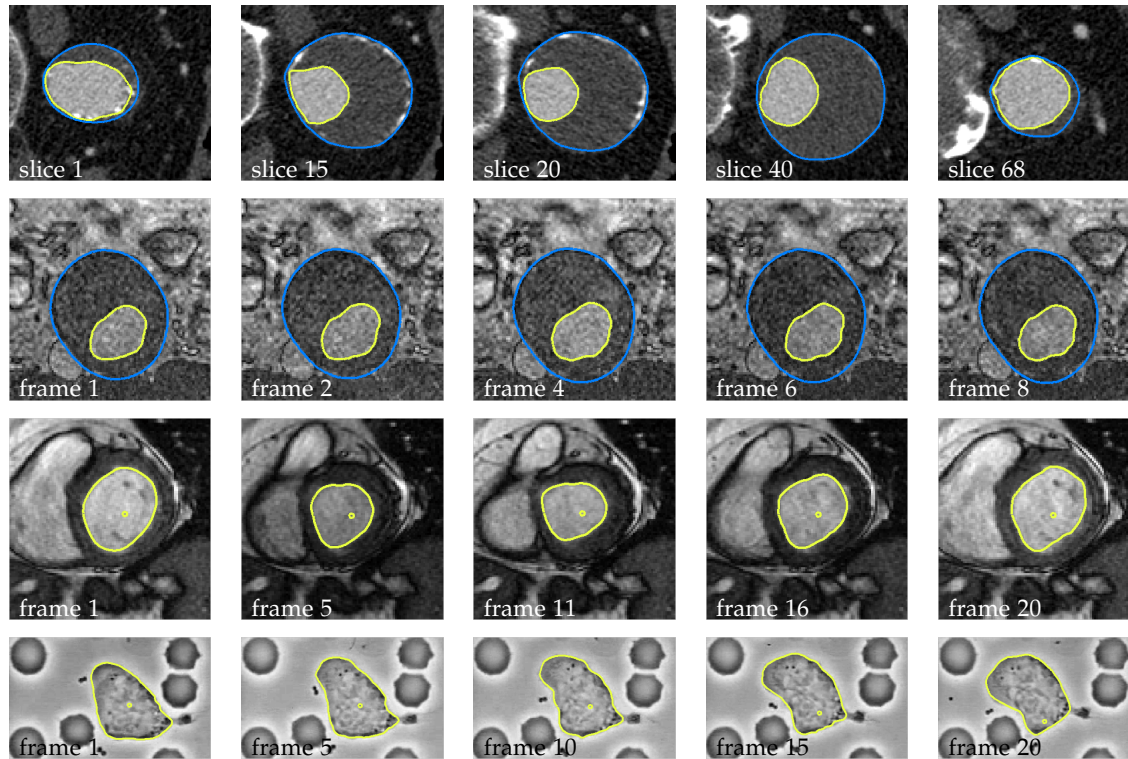


Figure 4.9: **Application Examples:** Spatial tracking of an abdominal aortic aneurysm from CTA (first row), temporal tracking of another aneurysm in one slice of 4D MRI (second row), temporal tracking of a cross-section of the left ventricular cavity in 4D MRI (third row), and tracking of a leukocyte chasing a bacterium (fourth row).

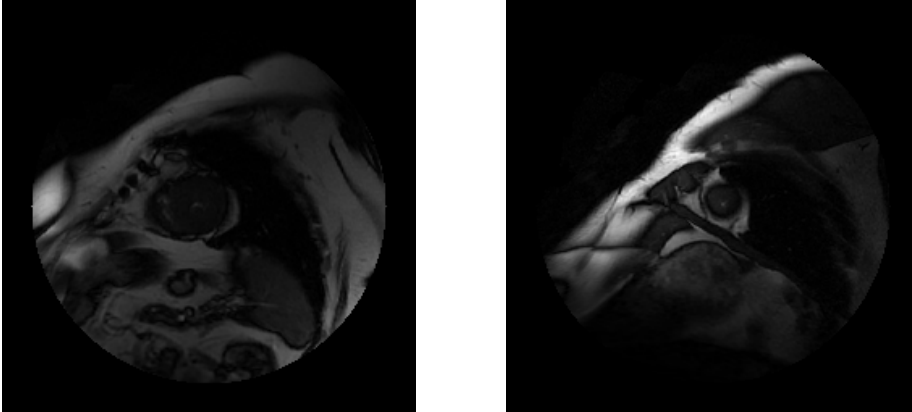


Figure 4.10: Examples of Excluded Slices.

#### 4.4.5 Quantitative Evaluation

We also performed a quantitative evaluation on the evaluation data set of the 2009 MICCAI left ventricle segmentation challenge [91]. One task of this challenge was the automatic or semi-automatic delineation of the cavity boarder on 260 slices from 15 subjects. The goal of the presented experiments based on this data set is to show that the proposed method can be applied to real world challenges without tremendous methodological modifications or extensive parameter tuning. For this reason we designed a simple MATLAB segmentation tool which only requires the selection of a filename and the definition of an initial circle by two diametral points. We used the localized Chan-Vese model of Lankton *et al.* [59] as an energy, where the diameter of the localization sphere was set to five pixels, and kept the standard parameter settings, i.e.  $\lambda = 1$  and  $\gamma = 0.024$ , for all experiments. An aspect which makes this segmentation task challenging is the fact that the intensity values of the papillary muscles, which are located inside the ventricular cavity, are quite similar to the ones of the myocardium. As the papillary muscles can only be approximated by higher frequencies of the contour we restricted the number of frequencies to five. This way, the model can be distracted far less by these fine scale structures, but it is still flexible enough to segment the cavity boarder.

After performing the experiments, we used the original evaluation framework provided by [91], which consists of a set of expert segmentations as well as an evaluation software, for generating the results presented in Tab. 4.1 and Fig 4.11. The provided framework calculates the following quality measures:

- the number and the percentage of detected contours,
- the average perpendicular distance from the automatically segmented contour to the corresponding manually drawn expert contour,
- the DICE metric, i.e. a measure of contour overlap based on the areas of

patient	# automatic	# manual	% detected	% "good"	∅ dist. (mm)	∅ DICE
SC-HF-I-01	18	18	100.00	72.22	2.62	0.8860
SC-HF-I-02	18	18	100.00	94.44	2.73	0.8745
SC-HF-I-04	20	20	100.00	95.00	2.96	0.8834
SC-HF-I-40	18	18	100.00	94.44	2.47	0.8671
SC-HF-NI-03	20	20	100.00	65.00	4.09	0.8638
SC-HF-NI-04	20	20	100.00	90.00	3.12	0.8856
SC-HF-NI-34	20	20	100.00	90.00	2.06	0.9012
SC-HF-NI-36	18	18	100.00	94.44	2.47	0.9113
SC-HYP-01	11	12	91.67	75.00	2.38	0.8661
SC-HYP-03	13	13	100.00	84.62	3.02	0.7902
SC-HYP-38	14	18	77.78	61.11	3.14	0.7872
SC-HYP-40	15	18	83.33	55.56	4.18	0.7565
SC-N-02	17	17	100.00	82.35	2.55	0.8366
SC-N-03	15	17	88.24	82.35	2.40	0.8758
SC-N-40	13	13	100.00	76.92	3.07	0.7855
<b>overall</b>	250	260	96.15	80.90	2.88	0.8514

Table 4.1: Results of the Quantitative Evaluation.

the automatically and manually segmented contours<sup>1</sup>, and finally

- the percentage of "good" contours, i.e. the percentage of contours whose average perpendicular distance is less than 5mm.

Of course, one would expect that the detection rate of a semi-automatic approach is 100%, but we had to exclude apical 10 slices where the left ventricular cavity consisted of only one to three pixels, cf. Fig. 4.10. In general, however, the obtained results are well comparable to the ones achieved by other approaches which participated in this challenge, cf. corresponding issue of the MIDAS journal. This is even more remarkable as several other methods require training data or more user interaction. While the presented method works quite well as far as the robustness with respect to the papillary muscles is concerned, it is quite susceptible in the case of very fuzzy boundaries, especially in the case of apical slices, cf. Fig. 4.11. These problems might arise from the fixed size of the localization sphere, but as mentioned above we wanted to present an approach which does not require extensive parameter tuning.

<sup>1</sup>The DICE metric takes values in  $[0, 1]$ , where higher values indicating a better match.

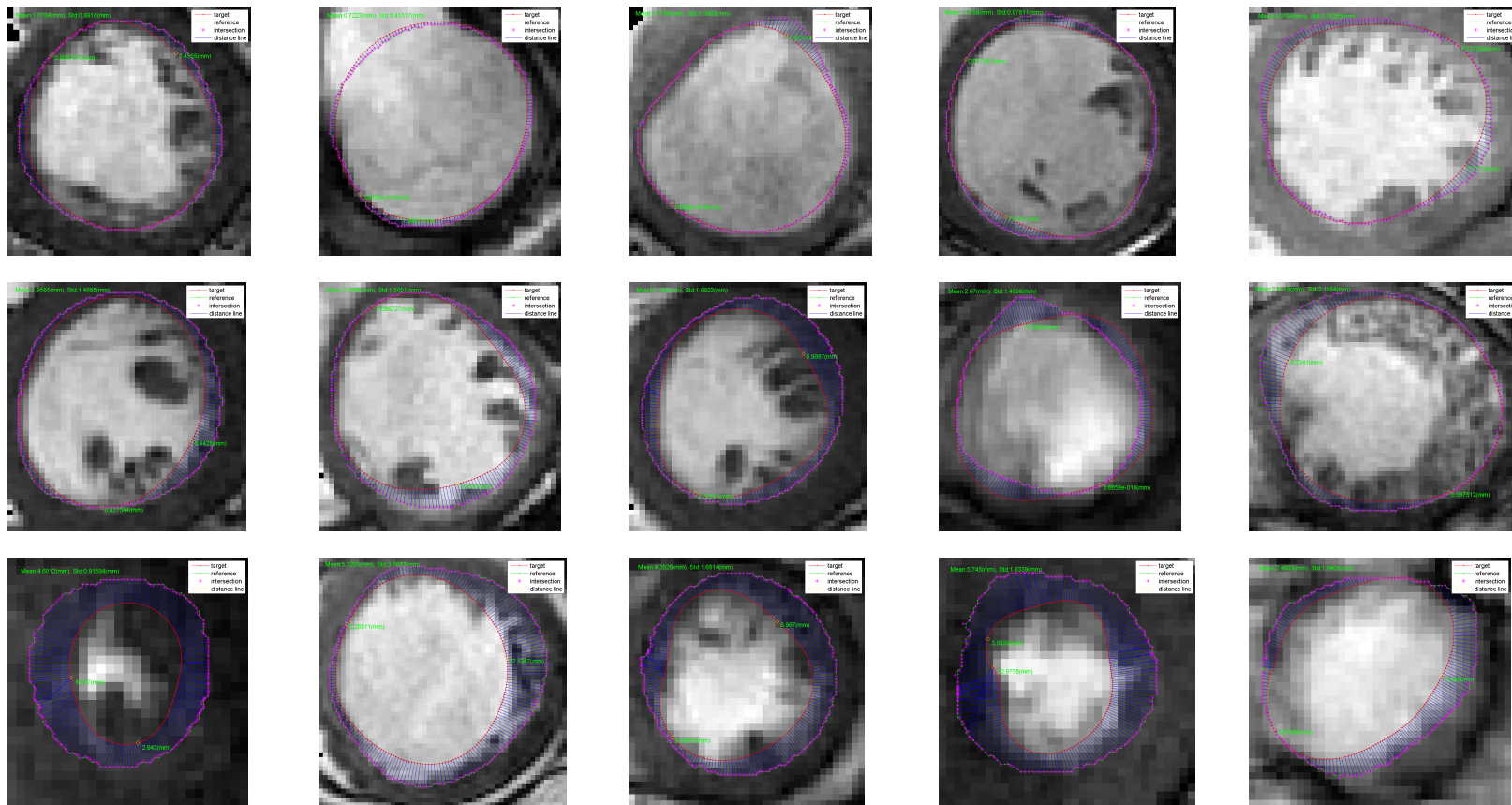


Figure 4.11: **Qualitative Results:** Good results (upper row), medium quality results (middle row), and bad results (lower row).



# 5

## Conclusion

We finally wish to sum up the contributions presented in this dissertation and discuss some interesting questions and directions for further research.

In Sec. 1.2 we have introduced the concepts of implicit and explicit regularization and showed that these concepts comprise powerful classification taxonomies, cf. chapter 2. Although many explicit and implicit regularization strategies have been proposed we believe that this topic has been fading from the spotlight too much and should be considered from a more general point of view again, as it is done in the articles of Terzopoulos [113] and Poggio *et al.* [89] for instance. In particular, we think that the following question should be answered from a more general point of view:

*Given a particular application, which regularization strategy should be chosen?*

We hope that the considerations and generalizations presented in this thesis help to reinforce future research with respect to this as well as related questions.

In Sec. 3.1.1 we have generalized several non-geometric variational level set methods. In particular, we have seen that convex active contour models exhibit a (hidden) degree of freedom - namely the choice of a (degenerate) binarization operator. A possible direction for further research could thus be the following question:

*Are there other (degenerate) convex binarization operators, which allow for a strictly convex formulation for instance?*

In Sec. 3.1.4 we have compared numerical techniques for  $H^1$ - and Tikhonov-type regularized variational level set formulations in the non-geometric case. We have seen that these regularization strategies can lead to update equations of the same computational complexity while revealing the fundamental differences of explicit and implicit regularization strategies.

In Sec. 3.2 we have presented a convenient and efficient framework for Sobolev active contours and surfaces, which is derived in a fully implicit manner. In contrast to previous approaches [21, 34], we have proposed a geometrically motivated Sobolev-type inner product. The performed experiments clearly show that the Sobolev gradients obtained with the proposed

numerical scheme lead to smooth curve and surface evolutions. If desired, one can even use operator splitting techniques, e.g. [123], in order to compute an approximate Sobolev gradient in linear complexity. Future work might include the usage of more sophisticated inner products, such as the ones described in [107], or the incorporation of the ideas presented in [22].

In chapter 4 we have proposed a framework for polar active contours, which allows the user to weight translations, scale changes and smooth deformations of the curve differently. Our framework inherits the robustness to local minima from Sobolev active contours and it allows the user to directly minimize the desired energy without the need for additional regularizers. The application examples show that the  $\mathcal{H}$  flow for polar active contours is a powerful and efficient extension of standard polar active contours. The performed quantitative evaluation hopefully convinces the reader that the design of geometrically motivated implicit regularization strategies is a powerful alternative to the *convexification* of active contour approaches, in order to make active contours more global. We believe that further improvements could be achieved by incorporating geometric priors on the isoperimetric ratio or the boundary length as demonstrated in [109].



# Sobolev Spaces

The concept of Sobolev spaces is essential in this dissertation and when dealing with them we often take several non-trivial facts, such as the possibilities of selecting a continuous representative or evaluating them on the boundary of a domain, for granted. For this reason we wish to provide a brief but mathematically correct definition along with some important tools here. The presented concepts can be found in many books on partial differential equations and functional analysis and we refer the interested reader to [35, 60, 32, 101].

At first, we need to introduce the well-known  $L^p$  spaces.

**Definition A.1 (The Function space  $L^p(\Omega)$ )** Let  $\Omega \subset \mathbb{R}^d$  (be a measurable set). For  $p \in [1, \infty)$ , the space  $L^p(\Omega)$  consists of all (measurable) functions for which

$$\int_{\Omega} |u|^p dx < \infty \quad (\text{A.1})$$

holds<sup>1</sup>.

Besides the standard  $L^p$  spaces we need the space of locally integrable functions.

**Definition A.2 (The Space of Locally Integrable Functions  $L^1_{\text{loc}}(\Omega)$ )** Let  $\Omega \subset \mathbb{R}^d$ . The function space  $L^1_{\text{loc}}(\Omega)$  consists of all functions  $u$  for which

$$u \in L^1(\Omega_0) \quad (\text{A.2})$$

holds for any open subset  $\Omega_0 \subset \subset \Omega$ .

The function spaces  $L^p(\Omega)$  are Banach spaces.

**Theorem A.1 ( $L^p$  is a Banach Space)** Endowed with the norm

$$\|u\|_{L^p} = \left( \int_{\Omega} |u|^p dx \right)^{\frac{1}{p}} \quad (\text{A.3})$$

the function space  $L^p(\Omega)$  becomes a Banach space.

---

<sup>1</sup>It should be noted that  $dx$  has to be understood in the sense of the Lebesgue-measure and not in the Riemannian sense.

The space  $L^2$ , however, has even more structure than other  $L^p$  spaces.

**Theorem A.2 (The Hilbert space  $L^2(\Omega)$ )** *Endowed with the inner product*

$$\langle u, v \rangle_{L^2} = \int_{\Omega} uv \, dx \quad (\text{A.4})$$

the function space  $L^2(\Omega)$  becomes a Hilbert space.

Now, we are in the position to formulate the fundamental lemma of variational calculus which helps us to derive the Euler-Lagrange equation(s) and to compute the Sobolev gradients.

**Theorem A.3 (Fundamental Lemma of Variational Calculus)** *Let  $\Omega \subset \mathbb{R}^d$  and  $u \in L^1_{loc}(\Omega)$ . If*

$$\int_{\Omega} uv \, dx = 0 \quad (\text{A.5})$$

for all  $v \in C_0^\infty$ , then  $u(x) = 0$  almost everywhere in  $\Omega$ .

Before, we can proceed with the introduction of the Sobolev spaces we have to introduce some notation.

**Definition A.3 (Multi-index)** *A multi-index is a vector  $\alpha = (\alpha_1, \dots, \alpha_n) \in \mathbb{N}_0^n$ . We define*

$$|\alpha| = \sum_{i=1}^n \alpha_i, \quad x^\alpha = x_1^{\alpha_1} \cdots x_n^{\alpha_n}, \quad D^\alpha u = \frac{\partial^{|\alpha|}}{\partial x_1^{\alpha_1} \cdots \partial x_n^{\alpha_n}} u. \quad (\text{A.6})$$

This allows us to define weak derivatives.

**Definition A.4 (Weak Derivative)** *Let  $u \in L^1_{loc}(\Omega)$ . If there exists a function  $u_\alpha \in L^1_{loc}(\Omega)$  such that*

$$\int_{\Omega} u D^\alpha v \, dx = (-1)^{|\alpha|} \int_{\Omega} u_\alpha v \, dx \quad (\text{A.7})$$

for all  $v \in C_0^\infty(\Omega)$ , we call  $u_\alpha$   $\alpha$ -weak derivative.

Now, we can finally define the Sobolev spaces  $H^m$ .

**Definition A.5 (The Sobolev Space  $H^m(\Omega)$ )** *Let  $m \in \mathbb{N}_0$ . The Sobolev space  $H^m(\Omega)$  consists of all functions  $u \in L^2(\Omega)$  for which  $u_\alpha$ ,  $|\alpha| \leq m$ , is an element of  $L^2(\Omega)$ .*

Fortunately,  $H^m$  is a Hilbert space.

**Theorem A.4 ( $H^m(\Omega)$  is a Hilbert Space)** *Endowed with the inner product*

$$\langle u, v \rangle_{H^m} = \sum_{|\alpha| \leq m} \int_{\Omega} D^\alpha u D^\alpha v \, dx \quad (\text{A.8})$$

$H^m(\Omega)$  becomes a Hilbert space.

---

In Hilbert spaces, we have powerful tools available to us. An important example is the Riesz representation theorem which helps us to express Sobolev gradients via standard  $L^2$  gradients.

**Theorem A.5 (Riesz Representation Theorem)** *Let  $H$  be a Hilbert space and  $F : H \rightarrow \mathbb{R}$  a linear functional which is bounded, i.e.*

$$|F(u)| \leq C \|u\|_H \quad (\text{A.9})$$

*holds for some constant  $C > 0$ . Then, there exists a uniquely determined element  $v \in H$  such that*

$$F(u) = \langle u, v \rangle_H \quad (\text{A.10})$$

*for all  $u \in H$ .*

The following theorem is very important, if we want to know, if an element of a Sobolev space is continuous in the classical sense.

**Theorem A.6 (Continuous Embedding)** *If  $\Omega \subset \mathbb{R}^d$  is a Lipschitz domain, i.e. a domain whose boundary can be locally described by a Lipschitz continuous function, and  $m - \frac{d}{2} > k$ , there exists a continuous embedding*

$$H^m(\Omega) \hookrightarrow C^k(\Omega). \quad (\text{A.11})$$

In other words, if  $m - \frac{d}{2} > 0$  for instance, we can find a continuous representative for any  $u \in H^m(\Omega)$ .

The evaluation of a function  $u \in H^m(\Omega) \subset H^1(\Omega)$  ( $m \geq 1$ ) at the boundary of a domain  $\Omega$  is tricky, because the boundary  $\partial\Omega$  has Lebesgue measure zero. Fortunately, there is a theorem which helps us.

**Theorem A.7 (Trace Theorem)** *If  $\Omega \subset \mathbb{R}^d$  is a Lipschitz domain, there exists a bounded linear operator  $T : H^1(\Omega) \rightarrow L^2(\partial\Omega)$  such that*

$$Tu = u|_{\partial\Omega}, \quad (\text{A.12})$$

*where  $u \in H^1 \cap C(\overline{\Omega})$ .*



# B

## Other Contributions

### B.1 Stent Graft Removal for Improving 2D-3D Registration

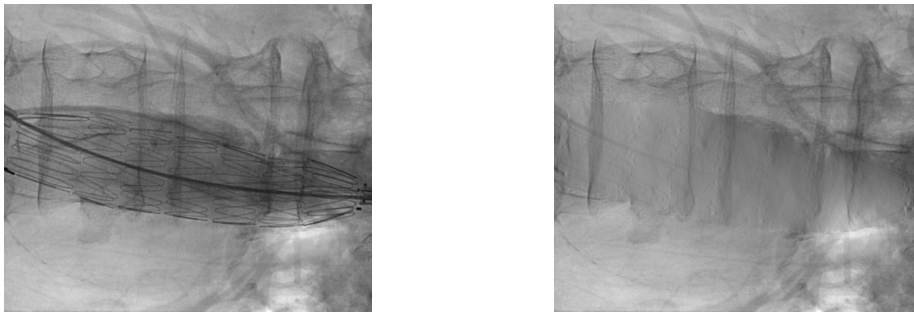


Figure B.1: An example for stent graft removal on a real interventional angiography. The original image is presented on the left and the reconstructed image is given on the right. Note that the borders of the vertebrae, which contain meaningful anatomical information, are well preserved while in contrast to this the stent graft and the catheter are hardly visible anymore.

**Maximilian Baust, Stefanie Demirci, Nassir Navab** Being performed under extensive radiation exposure, endovascular stent graft placements would greatly benefit from a reliable navigation solution. A successful implementation of such a system requires an accurate 2D-3D registration. Since the stent graft is only visible in the radiograph, registration algorithms can easily be attracted to wrong structures. In this paper, we address this problem by presenting a fast algorithm for removing the stent graft which meets real-time constraints. Based on Poisson editing, our method is easy to implement and extremely user-friendly as it requires neither parameter adjustment nor precise presegmentation. Moreover, we prove the significance of our algorithm by a realistic ground truth study.

## B.2 Monocular Deformable Model-to-Image Registration of Vascular Structures

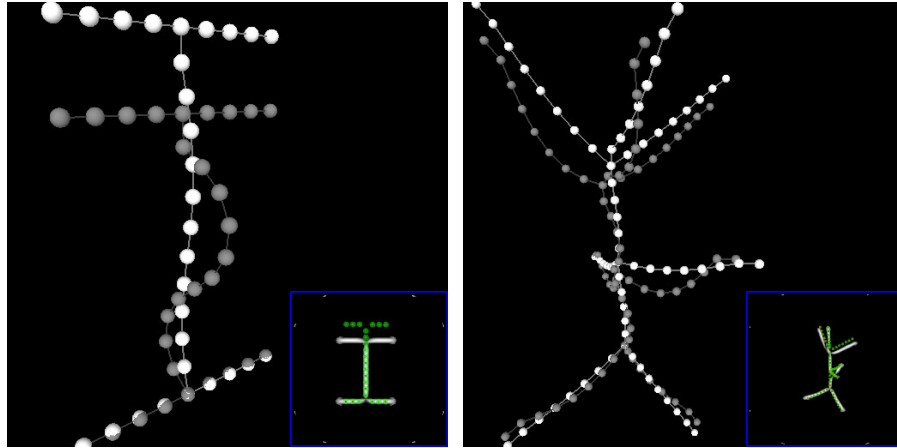


Figure B.2: Two synthetic data sets. The white spheres represent the input vascular model, the gray spheres show the deformed input model (the ground truth) from which the projection image has been generated. The lower right sub-images visualize the enhanced projection images, where green disks are drawn at all projected centerline points at the beginning of the registration.

**Martin Groher, Maximilian Baust, Darko Zikic, Nassir Navab** The registration of 3D vasculature to 2D projections is the key for providing advanced systems for image-based navigation and guidance. In areas with non-rigid patient motion, however, it is very difficult to accurately perform the registration if only one 2D view is available. We propose a method for deformable registration of a 3D vascular model extracted from an angiographic scan to a single 2D Digitally Subtracted Angiogram (DSA). Different to existing approaches, our method does not require a segmentation of 2D vasculature. In consequence, our method can be used without manual interaction during medical treatment. Formulated as an energy minimization problem, our approach combines a novel data term with the length regularization proposed in [44] which removes the ill-posedness of this monocular scenario. Besides attracting projected 3D centerline points to locations with high vessel probability the proposed data term ensures an injective projection of the centerline points. Due to our novel image-based data term, we achieve a considerable gain in performance compared to feature-based approaches.

Accuracy, robustness to outliers, as well as performance issues are analyzed through tests on synthetic and real data within a controlled environment.

### B.3 Generalization of Deformable Registration in Riemannian Sobolev Spaces

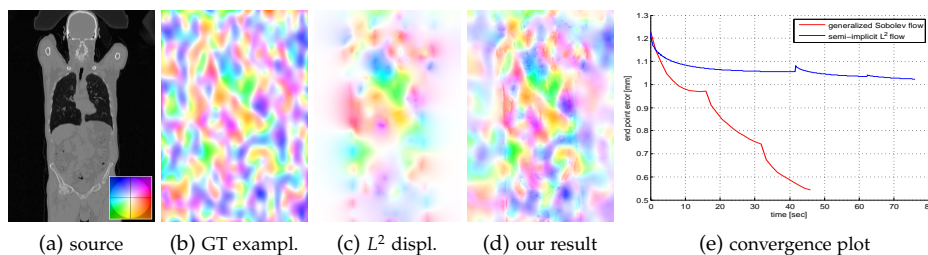


Figure B.3: Random convergence study in a mono-modal setting with SSD. Results in (e) are the mean of 100 trials, and w.r.t. actual computation time. Displacements in (b)-(d) are color-coded, c.f. (a) and <http://vision.middlebury.edu/flow/>. Bumps in (e) are due to transitions between resolution level. The proposed method clearly outperforms the semi-implicit  $L^2$  flow in terms in speed and accuracy.

**Darko Zikic, Maximilian Baust, Ali Kamen, Nassir Navab** In this work we discuss the generalized treatment of the deformable registration problem in Sobolev spaces. To this end, we extend previous approaches in two points: 1) by employing a general energy model consisting of a similarity measure *and* a regularization term, and 2) by changing the notion of distance in the Sobolev space by problem-dependent Riemannian metrics. The actual choice of the metric is such that it has a preconditioning effect on the problem. The preconditioning strategy is applicable to arbitrary similarity measures and features a simple implementation. Our experiments demonstrate an improvement in speed by several orders of magnitude in comparison to semi-implicit gradient flows in  $L^2$ , as well as increased accuracy. Furthermore, the proposed generalization establishes a theoretical link between gradient flow in Sobolev spaces and elastic registration methods.

## B.4 A General Preconditioning Scheme for Difference Measures in Deformable Registration

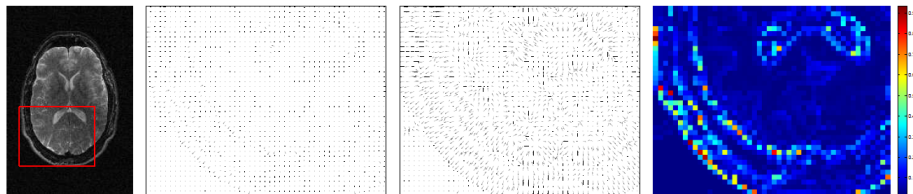


Figure B.4: From left to right: Source image, point-wise gradient vectors of the difference measure, normalized point-wise gradient vectors, and values of the preconditioner.

**Darko Zikic, Maximilian Baust, Ali Kamen, Nassir Navab** We present a preconditioning scheme for improving the efficiency of optimization of arbitrary difference measures in deformable registration problems. The proposed scheme is simple and computationally efficient: it performs an approximate normalization of the point-wise vectors of the difference gradient to unit length. The major contribution of this work is a theoretical analysis which demonstrates the improvement of the condition by our approach, which is shown to be an approximation to the optimal preconditioning for the analyzed model. The proposed approach is of particular interest for high-dimensional registration problems with statistical difference measures such as MI, and especially for the demons method, since in these cases the range of applicable standard optimization methods is limited. Because of the simplicity of the proposed scheme, its application improves the convergence speed with negligible added cost. The theoretical findings are confirmed by a series of experiments on 3D brain data.

## B.5 Midbrain Segmentation in Transcranial 3D Ultrasound for Parkinson Diagnosis

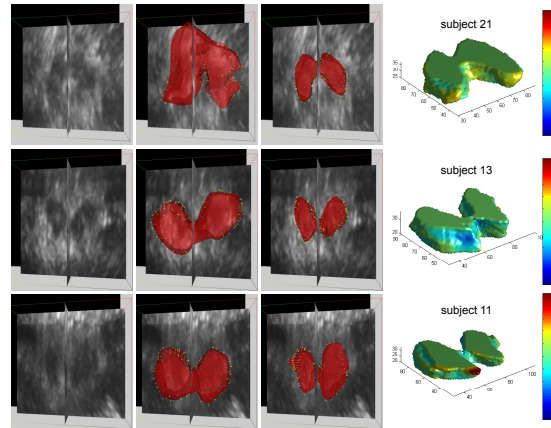


Figure B.5: Exemplary Segmentation Results: Rows: data from three subjects. Columns: sample slice through volume with midbrain visible (left), segmentation result without data term localization (middle left), segmentation result with localization (middle right), mesh surface distance map between result and ground truth (colorbar in mm).

**Seyed-Ahmad Ahmadi, Maximilian Baust, Athanasios Karamalis, Annika Plate, Kai Boetzel, Tassilo Klein, Nassir Navab** Ultrasound examination of the human brain through the temporal bone window, also called transcranial ultrasound (TC-US), is a completely non-invasive and cost-efficient technique, which has established itself for differential diagnosis of Parkinson’s Disease (PD) in the past decade. The method requires spatial analysis of ultrasound hyper-echogenicities produced by pathological changes within the Substantia Nigra (SN), which belongs to the basal ganglia within the midbrain. Related work on computer aided PD diagnosis shows the urgent need for an accurate and robust segmentation of the midbrain from 3D TC-US, which is an extremely difficult task due to poor image quality of TC-US. In contrast to 2D segmentations within earlier approaches, we develop the first method for semi-automatic midbrain segmentation from 3D TC-US and demonstrate its potential benefit on a database of 11 diagnosed Parkinson patients and 11 healthy controls.

## B.6 3D Stent Recovery from One X-ray Projection

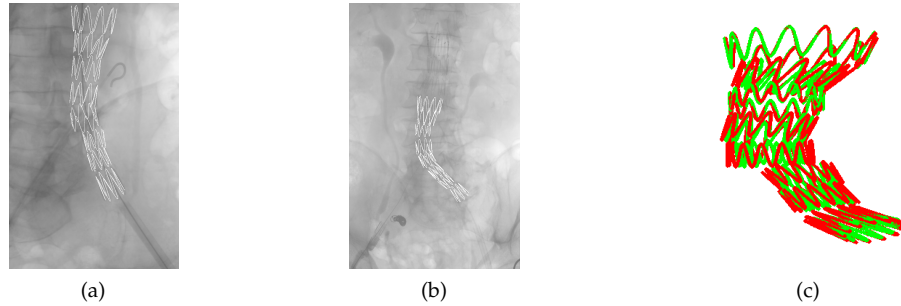


Figure B.6: Real experiment: (a)-(b) detection results (white) overlaid onto interventional images acquired from two different views, (c) 3D recovery of both stent shapes (green,red) after applying a common scale to all green segments

**Stefanie Demirci, Ali Bigdelou, Lejing Wang, Christian Wachinger, Maximilian Baust, Radhika Tibrewal, Reza Ghotbi, Hans-Henning Eckstein, Nassir Navab** In the current clinical work flow of endovascular abdominal aortic repairs (EVAR) a stent graft is inserted into the aneurysmatic aorta under 2D angiographic imaging. Due to the missing depth information in the X-ray visualization, it is highly difficult in particular for junior physicians to place the stent graft in the preoperatively defined position within the aorta. Therefore, advanced 3D visualization of stent grafts is highly required. In this paper, we present a novel algorithm to automatically match a 3D model of the stent graft to an intraoperative 2D image showing the device. By automatic preprocessing and a global-to-local registration approach, we are able to abandon user interaction and still meet the desired robustness. The complexity of our registration scheme is reduced by a semi-simultaneous optimization strategy incorporating constraints that correspond to the geometric model of the stent graft. Via experiments on synthetic, phantom, and real interventional data, we are able to show that the presented method matches the stent graft model to the 2D image data with good accuracy.

# Bibliography

- [1] Al-Shakhrah, I., Al-Obaidi, T.: Common artifacts in computerized tomography: A review. *Applied Radiology* **32**(8), 25–30 (2003)
- [2] Alpert, S., Galun, M., Basri, R., Brandt, A.: Image segmentation by probabilistic bottom-up aggregation and cue integration. In: *IEEE Conference on Computer Vision and Pattern Recognition* (2007)
- [3] Bar, L., Sapiro, G.: Generalized newton-type methods for energy formulations in image processing. *SIAM Journal on Imaging Sciences* **2**(2), 508–531 (2009)
- [4] Baust, M., Navab, N.: A spherical harmonics shape model for level set segmentation. In: *European Conference on Computer Vision* (2010)
- [5] Baust, M., Navab, N.: A fully implicit framework for sobolev active contours and surfaces. In: *Annual Symposium of the German Association for Pattern Recognition (DAGM)* (2011)
- [6] Baust, M., Yezzi, A., Unal, G., Navab, N.: A sobolev-type metric for polar active contours. In: *IEEE Conference on Computer Vision and Pattern Recognition* (2011)
- [7] Baust, M., Zikic, D., Navab, N.: Diffusion-based regularisation strategies for variational level set segmentation. In: *British Machine Vision Conference* (2010)
- [8] Bernard, O., Friboulet, D., Thevenaz, P., Unser, M.: Variational b-spline level-set: A linear filtering approach for fast deformable model evolution. *IEEE Transactions on Image Processing* **18**(6), 1179–1191 (2009)
- [9] Bertalmio, M., Cheng, L.T., Osher, S., Sapiro, G.: Variational problems and partial differential equations on implicit surfaces. *Journal of Computational Physics* **174**(2), 759 – 780 (2001)

## BIBLIOGRAPHY

---

- [10] Bishop, C.M.: *Pattern Recognition and Machine Learning*. Springer (2006)
- [11] Blake, A., Zisserman, A.: *Visual Reconstruction*. MIT Press (1987)
- [12] Bodur, O., Grady, L., Stillman, A., Setser, R., Funka-Lea, G., O'Donnell, T.: Semi-automatic aortic aneurysm analysis. In: *SPIE Medical Imaging* (2007)
- [13] Bresson, X., Esedoglu, S., Vandergheynst, P., Thiran, J.P., Osher, S.: Fast global minimization of the active contour/snake model. *Journal of Mathematical Imaging and Vision* **28**(2), 151–167 (2007)
- [14] Brooks, R., Collins, D., Morandi, X., Arbel, T.: Deformable ultrasound registration without reconstruction. In: *Medical Image Computing and Computer-Assisted Intervention* (2008)
- [15] Caselles, V., Catté, F., Coll, T., Dibos, F.: A geometric model for active contours in image processing. *Numerische Mathematik* **66**, 1–31 (1993)
- [16] Caselles, V., Kimmel, R., Sapiro, G.: Geodesic active contours. In: *International Conference on Computer Vision* (1995)
- [17] Caselles, V., Kimmel, R., Sapiro, G.: Geodesic active contours. *International Journal on Computer Vision* **22**(1), 61–79 (1997)
- [18] Chalana, V., Kim, Y.: A methodology for evaluation of boundary detection algorithms on medical images. *IEEE Transactions on Medical Imaging* **16**(5), 642–652 (1997)
- [19] Chambolle, A.: An algorithm for total variation minimization and applications. *Journal of Mathematical Imaging and Vision* **20**, 89–97 (2004)
- [20] Chan, T.F., Vese, L.A.: Active contours without edges. *IEEE Transactions on Image Processing* **10**(2), 266–277 (2001)
- [21] Charpiat, G., Maurel, P., Pons, J.P., Keriven, R., Faugeras, O.: Generalized gradients: Priors on minimization flows. *International Journal on Computer Vision* **73**(3), 325–344 (2007)
- [22] Chen, S., Charpiat, G., Radke, R.J.: Converting level set gradients to shape gradients. In: *European Conference on Computer Vision* (2010)
- [23] Cohen, L., Cohen, I.: Finite-element methods for active contour models and balloons for 2-d and 3-d images. *IEEE Transactions on Pattern Analysis and Machine Intelligence* **15**(11), 1131–1147 (1993)
- [24] Collewet, C.: Polar snakes: A fast and robust parametric active contour model. In: *IEEE International Conference on Image Processing* (2009)
- [25] Cootes, T., Edwards, G., Taylor, C.: Active appearance models. *IEEE Transactions on Pattern Analysis and Machine Intelligence* **23**(6), 681–685 (2001)

- [26] Cootes, T., Taylor, C., Cooper, D., Graham, J.: Active shape models - their training and application. *Computer Vision and Image Understanding* **61**(1), 38–59 (1995)
- [27] Cootes, T.F., Taylor, C.J.: Active shape models - 'smart snakes'. In: *British Machine Vision Conference* (1992)
- [28] Cremers, D., Rousson, M., Deriche, R.: A review of statistical approaches to level set segmentation: integrating color, texture, motion and shape. *International Journal of Computer Vision* **72**(2), 195–215 (2007)
- [29] Cremers, D., Schmidt, F.R., Barthel, F.: Shape priors in variational image segmentation: Convexity, lipschitz continuity and globally optimal solutions. In: *IEEE Conference on Computer Vision and Pattern Recognition* (2008)
- [30] Denzler, J., Niemann, H.: Active rays: polar-transformed active contours for real-time contour tracking. *Real-Time Imaging* **5**, 203–213 (1999)
- [31] Dias, J.M.B., Leitao, J.M.N.: Wall position and thickness estimation from sequences of echocardiographic images. *IEEE Transactions on Medical Imaging* **15**(1), 25–38 (1996)
- [32] Dobrowolski, M.: *Angewandte Funktionalanalysis*. Springer (2006)
- [33] Doretto, G., Chiuso, A., Wu, Y., Soatto, S.: Dynamic textures. *International Journal of Computer Vision* **51**(2), 91–109 (2003)
- [34] Eckstein, I., Pons, J.P., Tong, Y., Kuo, C.C.J., Desbrun, M.: Generalized surface flows for mesh processing. In: *Symposium on Geometry Processing* (2007)
- [35] Evans, L.C.: *Partial differential equations*. American Mathematical Society (1998)
- [36] Fernandez, M.M., Alberola-López, C.: An approach for contour detection of human kidneys from ultrasound images using markov random fields and active contours. *Medical Image Analysis* **9**(1), 1–23 (2005)
- [37] de Figueiredo, T.M., Leita, J.M.N.: Bayesian estimation of ventricular contours in angiographic images. *IEEE Transactions on Medical Imaging* **11**(3), 416–429 (1992)
- [38] Floreby, L.: A multiscale algorithm for closed contour matching in image sequence. In: *International Conference on Pattern Recognition* (1996)
- [39] Friedland, N., Adam, D.: Automatic ventricular cavity boundary detection from sequential ultrasound images using simulated annealing. *IEEE Transactions on Medical Imaging* **8**(4), 344–353 (1989)
- [40] Geman, S., Geman, D.: Stochastic relaxation, gibbs distributions, and the bayesian restoration of images. *IEEE Transactions on Pattern Analysis and Machine Intelligence* **6**(6), 721–741 (1984)

## BIBLIOGRAPHY

---

- [41] Gomes, J., Faugeras, O.D.: Reconciling distance functions and level sets. In: International Conference on Scale-Space Theories in Computer Vision (1999)
- [42] Gooya, A., Liao, H., Matsumiya, K., Masamune, K., Masutani, Y., Dohi, T.: A variational method for geometric regularization of vascular segmentation in medical images. *IEEE Transactions on Image Processing* **17**(8), 1295–1312 (2008)
- [43] Grbic, S., Ionasec, R., Vitanovski, D., Voigt, I., Wang, Y., Georgescu, B., Navab, N., Comaniciu, D.: Complete valvular heart apparatus model from 4d cardiac ct. In: Medical Image Computing and Computer-Assisted Intervention (2010)
- [44] Groher, M., Zikic, D., Navab, N.: Deformable 2d-3d registration of vascular structures in a one view scenario. *IEEE Transaction on Medical Imaging* **28**(6), 847–860 (2009)
- [45] Hadamard, J.: Sur les problèmes aux dérivés partielles et leur signification physique. *Princeton University Bulletin* **13**, 49–52 (1902)
- [46] Heimann, T., Meinzer, H.P.: Statistical shape models for 3d medical image segmentation: A review. *Medical Image Analysis* **13**(4), 543–563 (2009)
- [47] Hintermüller, M., Ring, W.: An inexact newton-cg-type active contour approach for the minimization of the mumford-shah functional. *Journal of Mathematical Imaging and Vision* **20**(1-2), 19–42 (2004)
- [48] Ho, H.P., Chen, Y., Liu, H., Shi, P.: Level set active contours on unstructured point cloud. In: IEEE Conference on Computer Vision and Pattern Recognition (2005)
- [49] Houston, B., Nielsen, M.B., Batty, C., Nilsson, O., Museth, K.: Hierarchical rle level set: A compact and versatile deformable surface representation. *ACM Transactions on Graphics* **25**(1), 151–175 (2006)
- [50] Hu, M., Ping, X., Ding, Y.: A new active contour model and its application on cell segmentation. In: Control, Automation, Robotics and Vision Conference (2004)
- [51] Huang, X., Metaxas, D., Chen, T.: Metamorphs: Deformable shape and texture models. In: IEEE Conference on Computer Vision and Pattern Recognition (2004)
- [52] Huang, X., Metaxas, D.N.: Metamorphs: Deformable shape and appearance models. *IEEE Transactions on Pattern Analysis and Machine Intelligence* **30**(8), 1444–1459 (2008)
- [53] Johnson, J.B.: Thermal agitation of electricity in conductors. *Physical Review* **32**(1), 97 (1928)

- 
- [54] Kass, M., Witkin, A., Terzopoulos, D.: Snakes: Active contour models. *International Journal of Computer Vision* **1**(4), 321–331 (1988)
- [55] Kelemen, A., Szekely, G., Gerig, G.: Elastic model-based segmentation of 3-d neuroradiological data sets. *IEEE Transactions on Medical Imaging* **18**(10), 828–839 (1999)
- [56] Kichenassamy, S., Kumar, A., Olver, P., Tannenbaum, A., Yezzi, A.: Gradient flows and geometric active contour models. In: *Computer Vision, 1995. Proceedings., Fifth International Conference on* (1995)
- [57] Kimia, B.B., Tannenbaum, A.R., Zucker, S.W.: Shapes, shocks, and deformations i: The components of two-dimensional shape and the reaction-diffusion space. *International Journal of Computer Vision* **15**, 189–224 (1995)
- [58] Krissian, K., Westin, C.F., Kikinis, R., Vosburgh, K.: Oriented speckle reducing anisotropic diffusion. *IEEE Transactions on Image Processing* **16**(5), 1412–1424 (2007)
- [59] Lankton, S., Tannenbaum, A.: Localizing region-based active contours. *IEEE Transactions on Image Processing* **17**(11), 2029–2039 (2008)
- [60] Lax, P.: *Functional Analysis*. Wiley-Interscience (2002)
- [61] Leventon, M., Grimson, W.E.L., Faugeras, O.: Statistical shape influence in geodesic active contours. In: *IEEE Conference on Computer Vision and Pattern Recognition* (2000)
- [62] Li, C., Huang, R., Ding, Z., Gatenby, C., Metaxas, D.N., Gore, J.C.: A level set method for image segmentation in the presence of intensity inhomogeneities with application to mri. *IEEE Transactions on Image Processing* **20**(7), 2007–2016 (2011)
- [63] Li, C., Xu, C., Gui, C., Fox, M.D.: Level set evolution without re-initialization: a new variational formulation. In: *IEEE Conference on Computer Vision and Pattern Recognition* (2005)
- [64] Li, C., Xu, C., Gui, C., Fox, M.D.: Distance regularized level set evolution and its application to image segmentation. *IEEE Transactions on Image Processing* **19**(12), 3243–3254 (2010)
- [65] Liang, J., Ding, G., Wu, Y.: Segmentation of the left ventricle from cardiac mr images based on radial gvf snake. In: *Biomedical Engineering and Informatics* (2008)
- [66] Malladi, R., Sethian, J., Vemuri, B.: Evolutionary fronts for topology-independent shape modeling and recovery (1994)
- [67] Malladi, R., Sethian, J.A., Vemuri, B.C.: Shape modeling with front propagation: a level set approach. *IEEE Transactions on Pattern Analysis and Machine Intelligence* **17**(2), 158–175 (1995)
-

## BIBLIOGRAPHY

---

- [68] Marr, D., Hildreth, E.: Theory of edge detection. Proceedings of the Royal Society of London. Series B. Biological Sciences **207**(1167), 187–217 (1980)
- [69] McKinstry, R.C., Jarrett, D.Y.: Magnetic susceptibility artifacts on mri: A hairy situation. *American Journal of Roentgenology* **182**(2), 532 (2004)
- [70] Mennucci, A.C.G., Yezzi, A.: Metrics in the space of curves (2004)
- [71] Michor, P., Mumford, D.: Riemannian geometries on the space of plane curves. *Journal of the European Mathematical Society* **8**, 1–48 (2006)
- [72] Morse, B.S., Liu, W., Yoo, T., Subramanian, K.: Active contours using a constraint-based implicit representation. In: IEEE Conference on Computer Vision and Pattern Recognition (2005)
- [73] Mory, B., Ardon, R., Yezzi, A., Thiran, J.P.: Non-euclidean image-adaptive radial basis functions for 3d interactive segmentation. In: IEEE International Conference on Computer Vision (2009)
- [74] Mumford, D., Shah, J.: Optimal approximations by piecewise smooth functions and associated variational problems. *Communications on Pure and Applied Mathematics* **42**(5), 577–685 (1989)
- [75] Nain, D., Haker, S., Bobick, A., Tannenbaum, A.: Multiscale 3-d shape representation and segmentation using spherical wavelets. *IEEE Transactions on Medical Imaging* **26**(4), 598–618 (2007)
- [76] Nikolova, M., Esedoglu, S., Chan, T.F.: Algorithms for finding global minimizers of image segmentation and denoising models. *SIAM Journal on Applied Mathematics* **66**(5), 1632–1648 (2006)
- [77] Nowozin, S., Lampert, C.: Structured learning and prediction in computer vision. *Foundations and Trends in Computer Graphics and Vision* (3-4), 185–365 (2011)
- [78] Nyquist, H.: Thermal agitation of electric charge in conductors. *Physical Review* **32**(1), 110–113 (1928)
- [79] Osher, S., Fedkiw, R.: *Level Set Methods and Dynamic Implicit Surfaces*. Springer (2003)
- [80] Osher, S., Paragios, N.: *Geometric Level Set Methods in Imaging, Vision, and Graphics*. Springer (2003)
- [81] Osher, S., Sethian, J.A.: Fronts propagating with curvature-dependent speed: Algorithms based on hamilton-jacobi formulations. *Journal of Computational Physics* **79**(1), 12–49 (1988)
- [82] Paragios, N., Deriche, R.: Geodesic active regions for motion estimation and tracking. In: IEEE International Conference on Computer Vision (1999)

- 
- [83] Paragios, N., Deriche, R.: Geodesic active regions and level set methods for supervised texture segmentation. *International Journal of Computer Vision* **46**, 223–247 (2002)
- [84] Paragios, N., Deriche, R.: Prior knowledge, level set representations and visual grouping. *International Journal of Computer Vision* **76**(3), 231–243 (2008)
- [85] Peng, D., Merriman, B., Osher, S., Zhao, H., Kang, M.: A pde-based fast local level set method. *Journal of Computational Physics* **155**(2), 410–438 (1999)
- [86] Pennec, X., Fillard, P.: Statistical computing on non-linear spaces for computational anatomy. In: N. Paragios, J. Duncan, N. Ayache (eds.) *Biomedical Image Analysis: Methodologies And Applications*. Springer (2011). To Appear
- [87] Pentland, A.P.: Automatic extraction of deformable part models. *International Journal of Computer Vision* **4**, 107–126 (1990)
- [88] Pham, D., C., X., JL., P.: Current methods in medical image segmentation. *Annual review of biomedical engineering* (2), 315–337 (2000)
- [89] Poggio, T., Torre, V., Koch, C.: Computational vision and regularization theory. *Nature* **317**, 314–319 (1985)
- [90] Pohl, K., Fisher, J., Bouix, S., Shenton, M.E., McCarley, R.W., Grimson, W.E.L., Kikinis, R., Wells, W.M.: Using the logarithm of odds to define a vector space on probabilistic atlases. *Medical Image Analysis* **11**(6), 465–477 (2007)
- [91] Radau, P., Lu, Y., Connelly, K., Paul, G., Dick, A., Wright, G.: Evaluation framework for algorithms segmenting short axis cardiac mri. *The MIDAS Journal* (2009)
- [92] Ravhon, R., Adam, D., Zelmanovitch, L.: Validation of ultrasonic image boundary recognition in abdominal aortic aneurysm. *IEEE Transactions on Medical Imaging* **20**(8), 751–763 (2001)
- [93] Ray, N., Acton, S.: Motion gradient vector flow: an external force for tracking rolling leukocytes with shape and size constrained active contours. *IEEE Transactions on Medical Imaging* **23**(12), 1466–1478 (2004)
- [94] Renka, R.: A simple explanation of the sobolev gradient method (2006)
- [95] Rooney, W.D., Johnson, G., Li, X., Cohen, E.R., Kim, S.G., Ugurbil, K., Springer, C.S.: Magnetic field and tissue dependencies of human brain longitudinal 1h2o relaxation in vivo. *Magnetic Resonance in Medicine* **57**(2), 308–318 (2007)
- [96] Rosman, G., Dascal L.and Tai, X.C., Kimmel, R.: On semi-implicit splitting schemes for the beltrami color image filtering. *Journal of Mathematical Imaging and Vision* **40**, 199–213 (2011)
-

## BIBLIOGRAPHY

---

- [97] Rudin, L.I., Osher, S., Fatemi, E.: Nonlinear total variation based noise removal algorithms. *Physica D* **60**(1-4), 259–268 (1992)
- [98] Saad, Y.: *Iterative Methods for Sparse Linear Systems*. Society for Industrial and Applied Mathematics (2003)
- [99] Sacan, A., Ferhatosmanoglu, H., Coskun, H.: Celltrack: an open-source software for cell tracking and motility analysis. *Bioinformatics* **24**(14), 1647–1649 (2008)
- [100] Schelten, K., Roth, S.: Connecting non-quadratic variational models and mrfs. In: *IEEE Conference on Computer Vision and Pattern Recognition* (2011)
- [101] Scherzer, O., Grasmair, M., Grossauer, H., Haltmeier, M., Lenzen, F.: *Variational Methods in Imaging*. Springer (2009)
- [102] Schnörr, S.: A study of a convex variational diffusion approach for image segmentation and feature extraction. *Journal of Mathematical Imaging and Vision* **8**(3) (1998)
- [103] Schottky, W.: Über spontane stromschwankungen in verschiedenen elektrizitätsleitern. *Annalen der Physik* **362**(23), 541–567 (1918)
- [104] Schudy, R.R.: Harmonic surfaces and parametric image operators: Their use in locating the moving endocardial surface from threedimensional cardiac ultrasound data. Tech. rep., University of Rochester (1981)
- [105] Slabaugh, G., Dinh, Q., Unal, G.: A variational approach to the evolution of radial basis functions for image segmentation. In: *IEEE Conference on Computer Vision and Pattern Recognition* (2007)
- [106] Staib, L., Duncan, J.: Model-based deformable surface finding for medical images. *IEEE Transactions on Medical Imaging* **15**(5), 720–731 (1996)
- [107] Sundaramoorthi, G., Mennucci, A., Soatto, S., Yezzi, A.: A new geometric metric in the space of curves, and applications to tracking deforming objects by prediction and filtering. *SIAM Journal on Imaging Sciences* **4**(1), 109–145 (2011)
- [108] Sundaramoorthi, G., Yezzi, A., Mennucci, A.: Coarse-to-fine segmentation and tracking using sobolev active contours. *IEEE Transactions on Pattern Analysis and Machine Intelligence* **30**(5), 851–864 (2008)
- [109] Sundaramoorthi, G., Yezzi, A., Mennucci, A., Sapiro, G.: New possibilities with sobolev active contours. *International Journal of Computer Vision* **84**(2), 113–129 (2008)
- [110] Sundaramoorthi, G., Yezzi, A.J., Mennucci, A.: Sobolev active contours. *International Journal of Computer Vision* **73**(3), 345–366 (2007)

- [111] Székely, G., Kelemen, A., Brechbühler, C., Gerig, G.: Segmentation of 2-d and 3-d objects from mri volume data using constrained elastic deformations of flexible fourier contour and surface models. *Medical Image Analysis* **1**(1), 19–34 (1996)
- [112] Szeliski, R.: Bayesian modeling of uncertainty in low-level vision. *International Journal on Computer Vision* **5**(3), 271–301 (1990)
- [113] Terzopoulos, D.: Regularization of inverse visual problems involving discontinuities. *IEEE Transactions on Pattern Analysis and Machine Intelligence* **8**(4), 413–424 (1986)
- [114] Terzopoulos, D., Metaxas, D.: Dynamic 3d models with local and global deformations: deformable superquadrics. *IEEE Transactions on Pattern Analysis and Machine Intelligence* **13**(7), 703–714 (1991)
- [115] Tikhonov, A.N., Arsenin, V.Y.: *Solutions of Ill-Posed Problems*. V. H. Winston & Sons, Washington, D.C.: John Wiley & Sons, New York, (1977)
- [116] Trouvé, A.: Diffeomorphisms groups and pattern matching in image analysis. *International Journal of Computer Vision* **28**(3), 213–221 (1998)
- [117] Tsagaan, B., Shimizu, A., Kobatake, H., Miyakawa, K.: An automated segmentation method of kidney using statistical information. In: *Medical Image Computing and Computer-Assisted Intervention* (2002)
- [118] Tsai, A., Yezzi, A., Wells, W., Tempany, C., Tucker, D., Fan, A., Grimson, W.E., Willsky, A.: A shape-based approach to the segmentation of medical imagery using level sets. *IEEE Transactions on Medical Imaging* **22**(2), 137–154 (2003)
- [119] Tsai, A., Yezzi, A., Willsky, A.S.: A curve evolution approach to smoothing and segmentation using the mumford-shah functional. In: *Computer Vision and Pattern Recognition, 2000. Proceedings. IEEE Conference on* (2000)
- [120] Veksler, O.: Star shape prior for graph-cut image segmentation. In: *European Conference on Computer Vision* (2008)
- [121] Vemuri, B., Radisavljevic, A., Leonard, C.: Multi-resolution stochastic 3d shape models for image segmentation. In: *Information Processing in Medical Imaging* (1993)
- [122] Warfield, S., Zou, K., Wells, W.: Simultaneous truth and performance level estimation (staple): an algorithm for the validation of image segmentation. *IEEE Transactions on Medical Imaging* **23**(7), 903–921 (2004)
- [123] Weickert, J., Romeny, B.M.T.H., Viergever, M.A.: Efficient and reliable schemes for nonlinear diffusion filtering. *IEEE Transactions on Image Processing* **7**(3), 398–410 (1998)

## BIBLIOGRAPHY

---

- [124] Wells, W.M., Grimson, W.E.L., Kikinis, R., Jolesz, F.A.: Adaptive segmentation of mri data. *IEEE Transactions on Medical Imaging* **15**(4), 429–442 (1996)
- [125] Widrow, B.: The 'rubber-mask' technique-i. pattern measurement and analysis. *Pattern Recognition* **5**(3), 175–176, IN1–IN2, 177–197 (1973)
- [126] Widrow, B.: The 'rubber-mask' technique-ii. pattern storage and recognition. *Pattern Recognition* **5**(3), 199 – 211 (1973)
- [127] Xu, C., Prince, J.L.: Gradient vector flow: a new external force for snakes. In: *Computer Vision and Pattern Recognition, 1997. Proceedings., 1997 IEEE Computer Society Conference on* (1997)
- [128] Yezzi, A., Kichenassamy, S., Kumar, A., Olver, P., Tannenbaum, A.: A geometric snake model for segmentation of medical imagery. *IEEE Transactions on Medical Imaging* **16**(2), 199–209 (1997)
- [129] Yezzi, A., Mennucci, A.: Conformal metrics and true "gradient flows" for curves. In: *IEEE International Conference on Computer Vision* (2005)
- [130] Zhao, H.K., Chan, T., Merriman, B., Osher, S.: A variational level set approach to multiphase motion. *Journal of Computational Physics* **127**(1), 179–195 (1996)
- [131] Zhu, S.C., Yuille, A.: Region competition: unifying snakes, region growing, and bayes/mdl for multiband image segmentation. *Pattern Analysis and Machine Intelligence, IEEE Transactions on* **18**(9), 884–900 (1996)